Crystal Chemistry, Elastic Properties and Melting Behaviors of Iron-Bearing Materials in Earth and Planetary Interiors

By

Jiachao Liu

A dissertation submitted in partial fulfillment
of the requirements for the degree of
Doctor of Philosophy
(Geology)
in the University of Michigan
2015

Doctoral Committee:

Associate Professor Jie (Jackie) Li, Chair
Professor Rebecca A. Lange
Associate Professor Vanessa Sih
Associate Professor Adam C. Simon
Professor Youxue Zhang

Dedication

This thesis is dedicated to my loving and supporting
wife, Nan Sun
grandparents, Jianxun Liu, Yufang Lu
parents, Ling Liu, Fugui Cao

Acknowledgements

My advisor Professor Jackie Li offered me the opportunity to study in University of Michigan since 2009, and has provided me all kinds of resources to finish my projects. She gives me enough freedom to explore my own interests; in the meanwhile, her critical and constructive review on my ideas, experiments and manuscripts significantly improve the quality of my work. I need to thank my defense committee Professor Youxue Zhang, Rebecca Lange, Adam Simon and especially my cognate committee Professor Vanessa Sih from physics department. I am grateful for Professor Udo Becker, Jeroen Ritsema and Peter van Keken, who served as my preliminary committee members.

I cannot thank enough Professor Bin Chen, who taught me all kinds of experimental skills step by step. He also taught me a great amount of knowledge in science and techniques and always encouraged me during the last six years. Thanks also go to Dr. Leslie Hayden for her help in electron microprobe analysis and fruitful discussions in geochemistry. I need to thank my group members Zeyu Li, Liang Li and Ryan Meredith for their help in my experiments.

I would like to thank Drs. Jesse Smith, Ross Hrubiak, Daijo Ikuta, Ligang Bai, Dimitry Popov, Stanislav Sinogeikin, Curtis kenney-Benson, Guoyin Shen and Yue Meng in high pressure collaborative access team (HPCAT) at the advanced photon source for letting me conduct my experiments using their world-leading high pressure high temperature techniques and awarding me beam times continuously for the last two years.

I need to thank two coauthors Drs. Bjorn Mysen and Yingwei Fei from Carnegie institution of Washington in my first paper and also Drs. Yingwei Fei and Katherine Crispin for letting me use

some instruments there.

Thanks also go to Dr. Fuxiang Zhang for teaching me analyze XRD spectra and sharing synchrotron beamtimes; Dr. Gordon Moore for his assistance in using electron microprobe; Professor David Walker, Jungfu Lin and Drs. Lili Gao, Zhixue Du, Jin Liu and Dongzhou Zhang for fruitful discussion in both experiments and theories.

Last but not least, I need to thank my family for supporting me to study aboard and pursue academic career. Especially to my lovely wife Nan Sun, who always supports me and shows me how a talented experimentalist does experiments and housework. She proofread my manuscripts, made ceramic octahedra for my multi-anvil experiments and polished samples.

Table of Contents

Dedication .... **ii**
Acknowledgements .... **iii**
List of Tables .... **vii**
List of Figures .... **viii**
Abstract .... **xi**

Chapter I. Introduction **1**

References **9**

Chapter II. Recoil-free Fractions of Iron in Aluminous Bridgmanite from Temperature Dependent Mössbauer Spectra **14**
2.1 Abstract **14**
2.2 Introduction **15**
2.3 Experimental Method **16**
2.3.1 Sample Synthesis and Characterization 16
2.3.2 Conventional Mössbauer Spectroscopy 17
2.4 Results and Discussions **18**
2.4.1 The Recoil-free Fractions of Fe^{2+} and Fe^{3+} in Al-Bm 19
2.4.2 Crystal Chemistry 20
2.4.3 Debye Temperature 23
2.4.4 The Fe^{2+} Site with Large QS 24
2.5 Implications **26**
2.6 References **35**

Chapter III. "Invar"-like Behavior in Compressed Fe_7C_3 with Implication for the Inner Core **41**
3.1 Abstract **41**
3.2 Introduction **42**
3.3 Experimental Methods **44**
3.4 Results **45**
3.5 Discussion **47**
3.5.1 Equations of State and Magnetic Transitions 47
3.5.2 Invar Behavior of Fe_7C_3 and Its Effect on Fe_7C_3 Formation 51
3.6 Implications **52**
3.7 References **66**

Chapter IV. Eutectic Melting of Fe-C System at the Core-mantle Boundary **72**

4.1 Abstract 72
4.2 Introduction 73
4.3 Experimental Methods 74
4.4 Results and Discussions 76
4.4 Reference 86

Chapter V. Chemical Convection in Lunar Core from Melting Experiments on Fe-Ni-S System 90
5.1 Abstract 90
5.2 Introduction 90
5.3 Experimental Methods 93
5.4 Results 94
5.5 Discussions 96
5.5.1 The Effects of Ni on the Properties of the Lunar Core 96
5.5.2 Thermodynamic Model 97
5.5.3 Core Evolution 99
5.5.4 Ancient Lunar Dynamo 101
5.6 Conclusions 103
5.7 References 118

Chapter VI. Conclusions 125

List of Tables

Table 2.1. Hyperfine parameters of $Mg_{0.87}Fe_{0.087}Si_{0.94}Al_{0.101}O_{2.994}$ bridgmanite at 1 bar. 28

Table 2.2. Debye parameters and recoil-free fractions of bridgmanites at 1 bar. 29

Table 3.1. Volume and unit-cell parameters of Fe_7C_3 at 300 K. ………………………….....……54

Table 3.2. Volume and unit-cell parameters of Fe at 300 K. 55

Table 3.3. Equation of state parameters of Fe_7C_3. 56

Table 4.1. Upper bound of eutectic melting tempeartures of Fe-C system at high pressures. 79

Table 5.1. Conditions and results of melting experiments in the systems of Fe-S and Fe-Ni-S at 5.1 GPa..104

Table 5.2. The partition coefficient of Ni between liquid and solid iron-alloys at different temperatures and 5.1 GPa. 106

Table 5.3. Margules interaction parameters at different pressures. 107

List of Figures

Figure 1.1. The layered structure of the Moon compared with that of the Earth based on seismic models. 8

Figure 2.1. The ^{57}Fe Mössbauer spectra of the starting orthopyroxene sample $(Mg_{0.9}Fe_{0.1})(Si_{0.9}Al_{0.10})O_3$ at room temperature. 30

Figure 2.2. Mössbauer spectra of $Mg_{0.868}Fe_{0.087}Si_{0.944}Al_{0.101}O_{2.994}$ bridgmanite between 65 K and 300 K at 1 bar. 31

Figure 2.3. Area fractions (a, b) and hyperfine parameters (c, d) of iron sites in bridgmanite $Mg_{0.868}Fe_{0.087}Si_{0.944}Al_{0.101}O_{2.994}$ as a function of temperature at 1 bar. 32

Figure 2.4. Calculated recoil-free fractions as a function of temperature, according to the Debye model. 33

Figure 2.5. Ternary diagram illustrating the cation substitution mechanisms in bridgmanite in full compositional range (a) and a close-up (b). 34

Figure 3.1. The configuration of the diamond anvil cell experiment. 57

Figure 3.2. Representative X-ray diffraction image of Fe_7C_3 at 33.2 GPa. 58

Figure 3.3. Representative X-ray diffraction patterns of Fe_7C_3 at 2.2 GPa and 67.9 GPa, respectively. 59

Figure 3.4. a) Unit-cell volume of Fe_7C_3 up to 68 GPa at 300 K. (b) The relation between finite Eulerian strain *F* and normalized stress *f*. 60

Figure 3.5. Pressures derived from Au at different locations within the DAC sample chamber and those from Ne and ruby 61

Figure 3.6. Lattice parameters *a* and *c* of Fe_7C_3 up to 68 GPa at 300 K. The inset is the axial ratio *a/c* vs. Pressure. 62

Figure 3.7. Unit-cell volume of Fe_7C_3 up to 21 GPa at 300 K is shown as open black circles....... 63

Figure 3.8. The comparison of the compression curve of *h*-Fe_7C_3 from different studies............. 64

Figure 3.9. The magnetic phase diagram of Fe_7C_3 up to the core's *P-T* conditions. 65

Figure 4.1. The change of X-ray diffraction images with increasing temperatures at 29.9 GPa.... 80

Figure 4.2. X-ray diffraction images and integrated spectra near the eutectic temperature at 29.9 GPa. 81

Figure 4.3. Eutectic melting points of Fe-C system and curve fit using the Simon-Glatzel equation, along with melting data from literature. 82

Figure 4.4. The eutectic melting curve of Fe-C system plotted together with geotherm and solidus curves of possible mantle materials. ………………………………………..………..76

Figure 4.5. Cartoon illustrating a possible sequence of subducted oceanic lithosphere going down the core-mantle boundary. 84

Figure 4.6. The dihedral angles in enstatite - FeNiS melt as a function of pressure from Shi et al., (2013) 85

Figure 5.1. Multi-anvil calibration curve for Umich 17/12 assembily. 108

Figure 5.2. (a) Reflected light image of the experiment at 5.1 GPa, 1478 K. (b) Back-scattered-electron (BSE) image showing part of the Fe-S sample in the experiment at 5.1 GPa, 1286 K. (c) and (d) are BSE images of Fe-S and Fe-Ni-S samples respectively, in the experiment at 5.1 GPa and 1580 K..109

Figure 5.3. The relation between thermocouple readings in the center of assembly and sample chamber. 110

Figure 5.4. The liquidi of Fe-S and Fe-Ni-S systems at 5.1 GPa..111

Figure 5.5. Solid metal/liquid metal partitioning of Ni in Fe-Ni-S system at 5.1 GPa.................112

Figure 5.6. (a) Fe-S liquidi between 1 bar and 10 GPa. Solid curves are fittings to experimental data using the asymmetric Margules solution formulation. (b) Fitted Margules parameters W_{Fe} and W_{FeS} as a function of pressure. 113

Figure 5.7. (a) Pressure dependence of liquidus temperature for Fe-S mixtures containing 1 wt.% to 10 wt.% sulfur. (b) The comparison between liquidus gradients and adiabatic gradients at lunar ICB pressure (5.1 GPa) for sulfur content up to 12 wt.%. 114

Figure 5.8. Pressure (solid) and and gravitational acceleration (dashed) in lunar interior. 115

Figure 5.9. The relation between the bulk sulfur content of the lunar core and sulfur content of the outer core. 116

Figure 5.10. Calculated compositional heat flux Q_c and the minimum heat flux Q_{min} across the lunar core-mantle boundary requested for core dynamo. 117

Abstract

Iron (Fe), with the maximal nuclear stability, is the most abundant element in the Earth. With a partially filled 3*d* shell, iron adds a variety of influences onto the physical properties and chemical behavior of the Earth and planetary interiors. This dissertation addresses a number of issues concerning the nature and dynamics of the Earth's lower mantle, the terrestrial cores by studying the crystal chemistry of aluminum- and iron-bearing magnesium silicate bridgmanite, elastic properties of iron carbide Fe_7C_3 and melting behaviors of Fe-C and Fe-Ni-S systems.

Aluminous bridgmanite (Al-Bm) is the dominant phase in the Earth's lower mantle. In this study, the Mössbauer spectra of an Al-Bm sample $Mg_{0.868}Fe_{0.087}Si_{0.944}Al_{0.101}O_{2.994}$ were recorded from 65 K to 300 K at 1 bar. The temperature dependence of the center shift was fitted by the Debye model and yielded the Debye temperatures of 305±3 K for Fe^{2+} and 361±22 K for Fe^{3+}. These values are lower than those of Al-free bridgmanite by 17% and 24%, respectively, indicating that the presence of Fe and Al increases the average Fe-O bond length and weakens the bond strength. At 300 K, the calculated recoil-free fractions of Fe^{2+} (0.637±0.006) and Fe^{3+} (0.72±0.02) are similar and therefore the molar fractions of Fe^{2+} and Fe^{3+} are nearly the same as the area fractions of the corresponding Mössbauer doublets. At 900 K, the calculated recoil-free fractions of Fe^{3+} is 46% higher than that of Fe^{2+}, implying that the molar fraction of Fe^{3+} is only 41% for a measured spectral area fraction of 50%, and that the area fractions of iron sites may change with temperature without any changes in the valence state or spin state of iron. We infer that Fe^{3+} accounts for 46±2 % of the iron in the Al-Bm and it enters the A site along with Al^{3+} in

the B site through the coupled-substitution mechanism. An Fe^{2+} component with large quadrupole splitting (~ 4.0 mm/s) was observed at cryogenic conditions and interpreted as a high-spin distorted iron site

Iron carbide Fe_7C_3 has recently emerged as a leading candidate component of the inner core because it is likely the first phase to solidify from a liquid containing iron and a small amount of carbon, and previous studies suggest that it provides a good match for the density and sound velocity of the inner core under relevant conditions. Pressure-induced magnetic transitions have been observed in Fe_7C_3 but the pressure of the ferromagnetic to paramagnetic transition remains controversial and its effect on equation of state (EoS) is unclear, thus introducing uncertainties in estimating the density of Fe_7C_3 under inner core pressures. Here we report the lattice parameters and unit cell volume of hexagonal Fe_7C_3 at 300 K and up to about 70 GPa, obtained through synchrotron x-ray diffraction measurements using a diamond anvil cell. The new data revealed significant softening near 8 GPa, followed by stiffening near 22 GPa. For comparison, the compression curve of iron in the same loading turned out to be smooth as expected, thus confirming that the abnormal behavior in Fe_7C_3 compression curve reflects its true nature and is not an artifact. The softening at the lower pressure and stiffening at the higher pressure can be attributed to a magnetic ordering transition and a spin crossover, respectively. By extrapolating the established equations-of-state (EoS) to the inner core pressure and accounting for the effect thermal expansion, we found that the non-magnetic phase provides a good match for the observed density, whereas the paramagnetic phase would be denser by 12~13 %.

Ultra-low-velocity-zones (ULVZs) are anomalous regions above the core-mantle boundary (CMB) with reduced shear wave velocity (*Vs*) and compressional wave velocity (*Vp*) and they are important for understanding the thermochemical evolution of the deep mantle. Existing hypotheses for the origin of the ULVZ often require very a very hot core, which may not be consistent with independent constraints for sustaining the geodynamo. Recent studies predicted that when the subducted slab entered the lower mantle, a mixture of about 1 wt.% iron and a small amount of carbon existed in the grain boundaries. To evaluate the fate of such mixture, I conducted melting experiments of the Fe-C system up to the lowermost mantle pressures, using the laser-heated diamond anvil cells and synchrotron x-ray diffraction techniques. Our results show that the melting curve of the Fe-C system intersects with mantle geotherm at 3068 kelvin and 128 GPa, implying that the onset of melting of iron-carbon mixture occurs within the D'' layer and that about 1 wt.% Fe-C melt associated with subducted slabs would be present at depths of 20 ~ 120 km above CMB. If such mixture melts at the lowermost mantle, it would completely wet grain boundaries and lower *Vs* more than *Vp*. Therefore, such metallic melt from subducted slabs provides a plausible explanation for the non-ubiquitous occurrence of ULVZ.

Paleomagnetic studies on lunar rocks revealed that ancient lunar dynamo probably existed 4.2 billion years ago and lasted for more than 500 million years. Recent dynamic simulations suggested that the lunar dynamo might have stopped when the solidification regime of the lunar core changed from freezing at the bottom of the molten core to crystallizing at the top of the liquid layer. To test this hypothesis, I conducted experiments at relevant pressure conditions using the multi-anvil apparatus to determine the melting behavior of Fe-S binary and Fe-Ni-S ternary systems as simplified model compositions for the lunar core. Our results show that for the Fe-S binary system the solidification regime of the core depends strongly on its sulfur content, and it is expected to switch from the Earth-like "frozen heart" scenario to "snowing" if the initial sulfur content falls between 5 and 11 wt.%. Applying a thermal evolution model, we find that a core with the initial sulfur content of about 7 wt.% can explain the timing and duration of the ancient lunar dynamo.

Chapter I. Introduction

Iron (Fe), with the maximal nuclear stability, is the most abundant element in the Earth (McDonough and Sun, 1995) and possibly other terrestrial planets and satellites, such as Mercury, Mars (Breuer et al., 2010). With a partially filled 3d shell, iron adds a variety of influences onto the physical properties and chemical behavior of the Earth and planetary interiors, such as temperature gradient, density, sound velocity (e.g. Li and Fei, 2014; Li, 2007).

Seismic discontinuities define the Earth's interior into crust, upper mantle, transition zone, lower mantle, D", outer core and inner core (Fig. 1.1 based on Dziewonski and Anderson, 1981). Across the transition zone, the major minerals transform from olivine polymorphs, pyroxenes and garnets in the upper mantle and transition zone into bridgemanite (Bm), ferropericlase (Fp) and calcium silicate perovskite (CaPv) in the lower mantle (Irifune et al., 2010). The lower mantle, as the most voluminous and massive layer inside the Earth, accounts for ~55% by volume and ~50% by mass of the Earth (Dziewonski and Anderson, 1981). Two most abundant minerals Bm and Fp can incorporate substantial amount of iron, whereas CaPv is essentially iron-free.

As the most abundant transition-metal element in the mantle, the oxidation state, spin state, and site occupancy of iron in lower mantle minerals are of particular importance because these factors may influence the density and velocity structure and convective pattern of the lower mantle (Badro, 2014; Li, 2007; Lin et al., 2013 and references within). Over the last decade, considerable experimental and computational studies have shown that iron in the lower mantle minerals undergoes spin transitions from the high-spin (HS) to the low-spin (LS) state due to increase of the crystal-field splitting energy (CFSE) with pressure (Badro, 2014; Li, 2007; Lin et al., 2013 and references within). The nature of spin transitions in Bm is still controversial (Badro, 2014; Li, 2007; Lin et al., 2013; McCammon et al., 2013 and references within). One well held view is that Fe^{3+} in the B site undergoes the HS-LS transition between 30~70 GPa while Fe^{2+} remains HS state in the A site (Catalli et al., 2010; Fujino et al., 2012; Lundin et al., 2008) at the lower mantle pressures. On the other hand, several studies claimed that at about 30 GPa, Fe^{2+} goes through a HS to intermediate spin (IS) transition, where electrons are only partially spin-paired, and changes to LS state at about 120 GPa (Kupenko et al., 2014; McCammon et al., 2010; McCammon et al., 2008; 2010; Narygina et al., 2010). Considering both Fe^{2+} and Fe^{3+} can enter either site or both sites in Bm and adopt either the HS or LS state, there are eight possible configurations, therefore the site occupancies for different iron species are essential for understanding the nature of spin states in Bm.

The D" layer (Fig. 1.1), extending about 250~350 km above the core-mantle boundary (CMB), is characterized by complex patterns of shear wave velocities (Garnero and McNamara, 2008 and references within). The D" discontinuity is associated with a solid-state phase transition from Bm with perovskite (Pv) structure to post-perovskite (pPv) (Murakami et al., 2004). Within the D" layer, there are some regions with greater than 10% drop in seismic velocities and have been named as Ultra-Low Velocity Zones (ULVZs): The heights of ULVZs are about 5~30 km and the lateral extent is ~ 100 km (McNamara et al., 2010 and references within), except a recent discovered one near Hawaii with ~ 900 km in diameter (Cottaar and Romanowicz, 2012). The origin and physical state of ULVZs are important for our understanding of the dynamic Earth and may provide new insight into the thermochemical evolution at CMB. Different hypotheses have been proposed for ULVZs in the basal mantle, including silicate partial melting (Andrault et al., 2014; Fiquet et al., 2010; Lay et al., 2004; Williams and Garnero, 1996); iron-rich materials due to core-mantle interaction (Mao et al., 2006; Wicks et al., 2010); ultra-dense remnants of descending slabs (Dobson and Brodholt, 2005).

Beneath CMB, the Earth's core has a radius of about 3480 km and occupies roughly one-sixth of the Earth by volume and one-third by mass (Fig. 1.1 based on Dziewonski and Anderson, 1981). One key question is the composition of the core: Seismic and geochemical/cosmochemical observations integrated with mineral physics measurements on relevant materials suggest more than 80 wt.% of the core is composed of iron and nickel accounts for ~ 5 wt.% (Li and Fei, 2014 and references within). Lighter elements are needed to explain the density deficit in the core with respect to pure iron under relevant pressure-temperature conditions (e.g. Birch, 1952). Hydrogen, carbon, oxygen, silicon and sulfur have been considered as major light elements present in the core based on their cosmochemical abundance and affinity with iron (Li and Fei, 2014 and references within). The nature and amount of light elements in the core are fundamental for understanding the formation and evolution of the Earth's core. In order to investigate light elements in the core, direct density comparison between the core and iron alloys at relevant pressure-temperature conditions are vital.

Carbon has been proposed as a primary light element in the Earth’s core because it is the fourth cosmochemically abundant element in the solar system, and it has strong affinity with both solid and liquid iron (Wood, 1993). In addition, carbonaceous chondrites, the most primitive meteorites, have 2.5~5.8 wt.% carbon in CI and CM chondrites (e.g. Kerridge, 1985; Mason, 1979). Fe_7C_3, as a major iron carbide, has received broad attention due to its unique physical and chemical properties: The density measurement of Fe_7C_3 up to the core's pressures showed the presence of Fe_7C_3could explain the density deficit of the inner core compared with pure iron at relevant pressure-temperature conditions (Chen et al., 2012; Nakajima et al., 2011). Besides, sound velocity measurement of compressed Fe_7C_3 found that the nonmagnetic phase exhibited low increase rate of sound velocity with pressure, which may explain the anomalously low shear wave velocity observed in the inner core (Chen et al., 2014). A ferromagnetic to paramagnetic transition in Fe_7C_3 under pressure has been reported, however the transition pressure differs by ~ 10 GPa in different studies (Chen et al., 2012; Nakajima et al., 2011). Therefore, more work is needed to understand the nature of magnetic transitions and their effects on the elastic properties of Fe_7C_3.

The core of the Earth's moon has similar structure as the Earth's core, where a solid inner core is surrounded by a liquid outer core based on seismic observation (Fig. 1.1 based on Weber et al., 2011); high quality lunar gravity data from Gravity Recovery and Interior Laboratory (GRAIL) mission (Williams et al., 2014) and laser ranging determination of pole orientation (Williams et al., 2001). The lunar solid inner core occupies 38% of the core in volume, which is much larger than that of the Earth’s core (4%) (Fig. 1.1). The thermal and chemical evolutions of the lunar core are important for understanding the origin and cessation of the ancient lunar dynamo (Laneuville et al., 2014; Ruckriemen et al., 2014; Williams, 2009). The lunar core should be mainly composed of Fe and Ni as the Earth’s core due to geochemical similarities between Earth and Moon (Dauphas et al., 2014 and references within). Considering the cosmochemical abundance of sulfur and its affinity with iron, sulfur is a likely light element present in the lunar core. In order to understand the thermochemical evolution of the lunar core, melting curves of lunar core materials at lunar core pressures are crucial.

This thesis reports experimental results of hyperfine parameters from Mössbauer spectra and fitted recoil-free fractions for bridgmanite (Chapter II); melting curves of Fe-S and Fe-Ni-S systems at the pressure of the lunar inner-core boundary (Chapter III); the equation of state (EoS) of Fe_7C_3 up to 70 GPa (Chapter IV) and the eutectic melting of Fe-C system up to 120 GPa (Chapter V).

In Chapter II, the crystal chemistry of Bridgmanite (Bm), the most abundant mineral in Earth, has been studied by temperature dependent Mössbauer spectra. Mössbauer spectroscopy probes the hyperfine interactions between the nuclei/nucleus and the surrounding electric and magnetic fields. It has been applied to investigating the valence state, spin state and crystal chemistry of iron in lower-mantle Bm (e.g., Fei et al. 1994; McCammon 1997, 1998; Jackson et al. 2005; Li et al. 2006; Lin et al. 2012; Bengtson et al. 2009; Narygina et al. 2010; Grocholski et al. 2009; Catalli et al. 2010; Hummer and Fei 2012). Of particular importance are Mössbauer measurements at variable temperatures, which provide information on recoil-free fractions (*f*) of different iron sites and thus allow for reliable determination of the relative proportions of divalent and trivalent iron. In this chapter, I analyzed Mössbauer spectra of an Al-Bm sample from 65 to 300 K at 1 bar and applied the results to examine the crystal chemistry of Fe^{2+} and Fe^{3+} in lower mantle Bm.

In chapter III, I investigated the magnetic phase diagram of Fe_7C_3 up to 68 Gpa at 300 K. A previous experimental study on compression curve of Fe_7C_3 found a ferromagnetic to paramagnetic transition at about 18 GPa and 300 K (Nakajima et al., 2011). In comparison, another experimental study at 300 K showed two-step magnetic transitions: a ferromagnetic to paramagnetic transition happened between 5.5 and 7.5 GPa, followed by a paramagnetic to nonmagnetic transition at 53 GPa (Chen et al., 2012). To understand the nature of magnetic transitions and their effects on Fe_7C_3, I measured the lattice parameters and unit cell volume of Fe_7C_3 at 300 K and up to 68 GPa, obtained through synchrotron X-ray diffraction (XRD) measurements using a diamond anvil cell (DAC).

In chapter IV, a new hypothesis has been proposed to explain ULVZs based on high pressure eutectic melting experiments on Fe-C system. Across the 660 km discontinuity, Fe^{2+} in ringwoodite disproportionates to Fe and Fe^{3+} (Frost et al., 2004). Fe^{3+} from this reaction enters Bm (Chapter II) while about 1 wt.% Fe distributes in the grain boundaries. Because some subducted slabs penetrated the transition zone and stagnated above CMB (Ritsema et al., 2004), metallic iron is expected to be transported down to the CMB. On the other hand, about 20-300 ppm carbon in subducted oceanic lithosphere is likely to be reduced to diamond in the lower mantle (Rohrbach and Schmidt, 2011). In this case, iron and diamond coexist in the subduction region beneath 660 km discontinuity. In order to investigate the fate of coexisting iron and diamond in the lower mantle, high pressure-temperature experiments were performed in Fe-C system using laser-heated diamond anvil cells. The eutectic melting curve of Fe-C system was determined up to 120 GPa and compared with geotherm. A new mechanism associated with Fe-C melt in the basal layer of the lower mantle is proposed to explain the significant velocity drops in ULVZs.

In Chapter V, the melting curves of both iron-sulfur system and iron-nickel-sulfur system at the pressure of the lunar inner-core boundary were measured using the multi-anvil apparatus at the University of Michigan. The pressure dependence of liquidi of lunar core compositions is essential for understanding the evolution of the lunar core (Williams, 2009). Interestingly, the pressures of the lunar core are about 5.1 GPa (Fig. 1.1 based on Weber et al., 2011), which is the pressure of the δ (bcc)- γ (fcc)–liquid triple point of pure iron (Anderson and Isaak, 2000). In addition, another major liquidus phase FeS also has a phase transition from FeS II to FeS III around 6 GPa (Fei et al., 1995). The phase transitions in iron and iron sulfide may significantly influence the behaviors of Fe-S and Fe-Ni-S liquidi. In this study, we measured the liquidi of Fe-S and Fe-Ni-S systems at the pressure of the lunar inner core boundary (ICB) in order to understand the evolution of the lunar core and the ancient lunar dynamo.

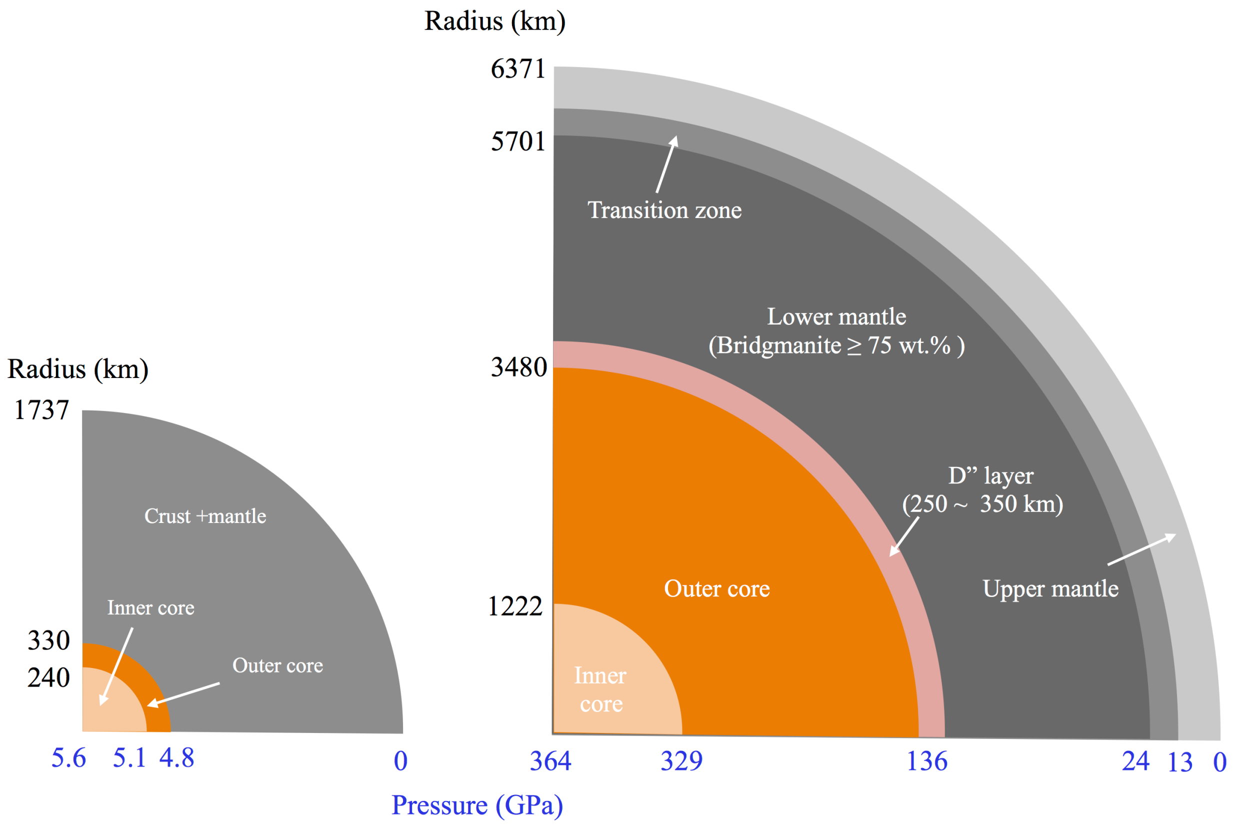

Figure 1.1. The layered structure of the Moon (left) compared with that of the Earth (right) based on seismic models (Dziewonski and Anderson, 1981; Weber et al., 2011). The volume fractions and radii of the outer and inner core, the pressures at the core-mantle boundary and inner-core boundary are shown.

References

Auzende, A.L., Badro, J., Ryerson, F.J., Weber, P.K., Fallon, S.J., Addad, A., Siebert, J., Fiquet, G., 2008. Element partitioning between magnesium silicate perovskite and ferropericlase: New insights into bulk lower-mantle geochemistry. Earth Planet Sc Lett 269, 164-174.

Breuer, D., Labrosse, S., Spohn, T., 2010. Thermal Evolution and Magnetic Field Generation in Terrestrial Planets and Satellites. Space Sci Rev 152, 449-500.

Catalli, K., Shim, S.H., Prakapenka, V.B., Zhao, J.Y., Sturhahn, W., Chow, P., Xiao, Y.M., Liu, H.Z., Cynn, H., Evans, W.J., 2010. Spin state of ferric iron in MgSiO3 perovskite and its effect on elastic properties. Earth Planet Sc Lett 289, 68-75.

Chen, B., Gao, L.L., Lavina, B., Dera, P., Alp, E.E., Zhao, J.Y., Li, J., 2012. Magneto-elastic coupling in compressed Fe7C3 supports carbon in Earth's inner core. Geophys Res Lett 39.

Cottaar, S., Romanowicz, B., 2012. An unsually large ULVZ at the base of the mantle near Hawaii. Earth Planet Sc Lett 355, 213-222.

Dobson, D.P., Brodholt, J.P., 2005. Subducted banded iron formations as a source of ultralow-velocity zones at the core-mantle boundary. Nature 434, 371-374.

Dziewonski, A.M., Anderson, D.L., 1981. Preliminary Reference Earth Model. Phys Earth Planet In 25, 297-356.

Fei, Y.W., Zhang, L., Corgne, A., Watson, H., Ricolleau, A., Meng, Y., Prakapenka, V., 2007. Spin transition and equations of state of (Mg, Fe)O solid solutions. Geophys Res Lett 34.

Fujino, K., Nishio-Hamane, D., Seto, Y., Sata, N., Nagai, T., Shinmei, T., Irifune, T., Ishii, H., Hiraoka, N., Cai, Y.Q., Tsuei, K.D., 2012. Spin transition of ferric iron in Al-bearing Mg-perovskite up to 200 GPa and its implication for the lower mantle. Earth Planet Sc Lett 317, 407-412.

Garnero, E.J., McNamara, A.K., 2008. Structure and dynamics of Earth's lower mantle. Science 320, 626-628.

Goncharov, A.F., Haugen, B.D., Struzhkin, V.V., Beck, P., Jacobsen, S.D., 2008. Radiative conductivity in the Earth's lower mantle. Nature 456, 231-234.

Goncharov, A.F., Struzhkin, V.V., Jacobsen, S.D., 2006. Reduced radiative conductivity of low-spin (Mg,Fe)O in the lower mantle. Science 312, 1205-1208.

Goncharov, A.F., Struzhkin, V.V., Montoya, J.A., Kharlamova, S., Kundargi, R., Siebert, J., Badro, J., Antonangeli, D., Ryerson, F.J., Mao, W., 2010. Effect of composition, structure, and spin state on the thermal conductivity of the Earth's lower mantle. Phys Earth Planet In 180, 148-153.

Irifune, T., Shinmei, T., McCammon, C.A., Miyajima, N., Rubie, D.C., Frost, D.J., 2010. Iron Partitioning and Density Changes of Pyrolite in Earth's Lower Mantle. Science 327, 193-195.

Keppler, H., Dubrovinsky, L.S., Narygina, O., Kantor, I., 2008. Optical Absorption and Radiative Thermal Conductivity of Silicate Perovskite to 125 Gigapascals. Science 322, 1529-1532.

Keppler, H., Kantor, I., Dubrovinsky, L.S., 2007. Optical absorption spectra of ferropericlase to 84 GPa. Am Mineral 92, 433-436.

Kupenko, I., McCammon, C., Sinmyo, R., Prescher, C., Chumakov, A.I., Kantor, A., Ruffer, R., Dubrovinsky, L., 2014. Electronic spin state of Fe,Al-containing MgSiO3 perovskite at lower mantle conditions. Lithos 189, 167-172.

Lay, T., Garnero, E.J., Williams, Q., 2004. Partial melting in a thermo-chemical boundary layer at the base of the mantle. Phys Earth Planet In 146, 441-467.

Li, J., 2007. Electronic Transitions and Spin States in the Lower Mantle. Geophys Monogr Ser 174, 47-68.

Lin, J.F., Speziale, S., Mao, Z., Marquardt, H., 2013. Effects of the Electronic Spin Transitions of Iron in Lower Mantle Minerals: Implications for Deep Mantle Geophysics and Geochemistry. Rev Geophys 51, 244-275.

Lin, J.F., Struzhkin, V.V., Jacobsen, S.D., Hu, M.Y., Chow, P., Kung, J., Liu, H.Z., Mao, H.K., Hemley, R.J., 2005. Spin transition of iron in magnesiowustite in the Earth's lower mantle. Nature 436, 377-380.

Lin, J.F., Weir, S.T., Jackson, D.D., Evans, W.J., Vohra, Y.K., Qiu, W., Yoo, C.S., 2007. Electrical conductivity of the lower-mantle ferropericlase across the electronic spin transition. Geophys Res Lett 34.

Lundin, S., Catalli, K., Santillan, J., Shim, S.H., Prakapenka, V.B., Kunz, M., Meng, Y., 2008. Effect of Fe on the equation of state of mantle silicate perovskite over 1 Mbar. Phys Earth Planet In 168, 97-102.

Mao, W.L., Mao, H.K., Sturhahn, W., Zhao, J.Y., Prakapenka, V.B., Meng, Y., Shu, J.F., Fei, Y.W., Hemley, R.J., 2006. Iron-rich post-perovskite and the origin of ultralow-velocity zones. Science 312, 564-565.

McCammon, C., Dubrovinsky, L., Narygina, O., Kantor, I., Wu, X., Glazyrin, K., Sergueev, I., Chumakov, A.I., 2010. Low-spin Fe2+ in silicate perovskite and a possible layer at the base of the lower mantle. Phys Earth Planet In 180, 215-221.

McCammon, C., Glazyrin, K., Kantor, A., Kantor, I., Kupenko, I., Narygina, O., Potapkin, V., Prescher, C., Sinmyo, R., Chumakov, A., Ruffer, R., Sergueev, I., Smirnov, G., Dubrovinsky, L., 2013. Iron spin state in silicate perovskite at conditions of the Earth's deep interior. High Pressure Res 33, 663-672.

McCammon, C., Kantor, I., Narygina, O., Rouquette, J., Ponkratz, U., Sergueev, I., Mezouar, M., Prakapenka, V., Dubrovinsky, L., 2008. Stable intermediate-spin ferrous iron in lower-mantle perovskite. Nat Geosci 1, 684-687.

McDonough, W.F., Sun, S.S., 1995. The Composition of the Earth. Chem Geol 120, 223-253.

Murakami, M., Hirose, K., Kawamura, K., Sata, N., Ohishi, Y., 2004. Post-perovskite phase transition in MgSiO3. Science 304, 855-858.

Nakajima, Y., Takahashi, E., Sata, N., Nishihara, Y., Hirose, K., Funakoshi, K., Ohishi, Y., 2011. Thermoelastic property and high-pressure stability of Fe7C3: Implication for iron-carbide in the Earth's core. Am Mineral 96, 1158-1165.

Narygina, O.V., Kantor, I.Y., McCammon, C.A., Dubrovinsky, L.S., 2010. Electronic state of Fe2+ in (Mg,Fe)(Si,Al)O-3 perovskite and (Mg,Fe)SiO3 majorite at pressures up to 81 GPa and temperatures up to 800 K. Phys Chem Miner 37, 407-415.

Ohta, K., Hirose, K., Onoda, S., Shimizu, K., 2007. The effect of iron spin transition on electrical conductivity of (Mg,Fe)O magnesiowustite. P Jpn Acad B-Phys 83, 97-100.

Ritsema, J., van Heijst, H.J., Woodhouse, J.H., 2004. Global transition zone tomography. J Geophys Res-Sol Ea 109.

Rohrbach, A., Schmidt, M.W., 2011. Redox freezing and melting in the Earth's deep mantle resulting from carbon-iron redox coupling. Nature 472, 209-212.

Weber, R.C., Lin, P.Y., Garnero, E.J., Williams, Q., Lognonne, P., 2011. Seismic Detection of the Lunar Core. Science 331, 309-312.

Wicks, J.K., Jackson, J.M., Sturhahn, W., 2010. Very low sound velocities in iron-rich (Mg,Fe)O: Implications for the core-mantle boundary region. Geophys Res Lett 37.

Williams, Q., Garnero, E.J., 1996. Seismic evidence for partial melt at the base of Earth's mantle. Science 273, 1528-1530.

Chapter II. Recoil-free Fractions of Iron in Aluminous Bridgmanite from Temperature Dependent Mössbauer Spectra

2.1 Abstract

Aluminous bridgmanite (Al-Bm) is the dominant phase in the Earth's lower mantle. In this study, the Mössbauer spectra of an Al-Bm sample $Mg_{0.868}Fe_{0.087}Si_{0.944}Al_{0.101}O_{2.994}$ were recorded from 65 K to 300 K at 1 bar. The temperature dependence of the center shift was fitted by the Debye model and yielded the Debye temperatures of 305±3 K for Fe^{2+} and 361±22 K for Fe^{3+}. These values are lower than those of Al-free bridgmanite by 17% and 24%, respectively, indicating that the presence of Fe and Al increases the average Fe-O bond length and weakens the bond strength. At 300 K, the calculated recoil-free fractions of Fe^{2+} (0.637±0.006) and Fe^{3+} (0.72±0.02) are similar and therefore the molar fractions of Fe^{2+} and Fe^{3+} are nearly the same as the area fractions of the corresponding Mössbauer doublets. At 900 K, the calculated recoil-free fractions of Fe^{3+} is 46% higher than that of Fe^{2+}, implying that the molar fraction of Fe^{3+} is only 41% for a measured spectral area fraction of 50%, and that the area fractions of iron sites may change with temperature without any changes in the valence state or spin state of iron. We infer that Fe^{3+} accounts for 46±2 % of the iron in the Al-Bm and it enters the A site along with Al^{3+} in the B site through the coupled-substitution mechanism. An Fe^{2+} component with large quadrupole splitting (~4.0 mm/s) was observed at cryogenic conditions and interpreted as a high-spin distorted iron site.

2.2 Introduction

Aluminum- and iron-bearing magnesium silicate bridgmanite (Mg,Fe,Al)(Si,Fe,Al)O_3 (abbreviated as “Al-Bm”, following the same convention as Rw for ringwoodite) is the predominant phase in the Earth’s lower mantle, and its physical properties and crystal chemistry play an important role in mantle dynamics. It adopts orthorhombic structure (space group: Pbnm) and has two cation sites: the pseudo-dodecahedral site and the octahedral site. Iron, with a partially filled 3d shell, adds a variety of influences to the physical properties and chemical behavior of Bm. The oxidation state, spin state, and site occupancy of iron in Bm are of particular importance because these factors may influence the density and velocity structure and convective pattern of the lower mantle (e.g., Badro 2014; Li 2007; Lin et al. 2013).

Mössbauer spectroscopy probes the hyperfine interactions between the nuclei/nucleus and the surrounding electric and magnetic fields. These interactions are expressed as center shift (CS), quadrupole splitting (QS), and the magnetic Zeeman splitting. Mössbauer spectroscopy also has been widely used to measure the valence state of iron in geological materials (Dyar et al., 2006). In the past two decades, Mössbauer spectroscopy has been applied to investigating the valence state, spin state and crystal chemistry of iron in lower-mantle Bm (e.g., Fei et al. 1994; McCammon 1997, 1998; Jackson et al. 2005; Li et al. 2006; Lin et al. 2012; Bengtson et al. 2009; Narygina et al. 2010; Grocholski et al. 2009; Catalli et al. 2010; Hummer and Fei 2012). Of particular importance are Mössbauer measurements at variable temperatures, which provide information on recoil-free fractions (*f*) of different iron sites and thus allow for reliable determination of the relative proportions of divalent and trivalent iron. Moreover, effects of temperature on the hyperfine parameters have been used to test the validity of the fitting procedure of Mössbauer data, and to gain additional insights on electron delocalization in Al-free Bm at elevated temperatuers (Fei et al. 1994; McCammon 1998).

Bridgmanite in the lower mantle contains 4.0~5.3 weight % Al (Wood and Rubie 1996). The presence of Al alters the crystal chemistry of iron and appears to stabilize trivalent iron in the structure (McCammon 1997; Frost et al. 2004). Such structural changes may also affect the recoil-free fractions of both Fe^{2+} and Fe^{3+}, which need to be determined in order to derive the Fe^{3+}/Fe ratios from Mössbauer spectra. Mössbauer data of Al-Bm under cryogenic conditions appear not to have been reported. In this study, we measured Mössbauer spectra of an Al-Bm sample from 65 to 300 K at 1 bar and applied the results to examine the crystal chemistry of Fe^{2+} and Fe^{3+} in lower mantle Bm.

2.3 Experimental Method

2.3.1 Sample Synthesis and Characterization

An Al-Bm sample was synthesized and characterized at the Geophysical Laboratory, Carnegie Institution of Washington. The synthesis procedure started with reducing a 94% ^{57}Fe enriched Fe_2O_3 to FeO at 1273 K and $\log f_{O2}$ = -14 (between the iron-wüstite and wüstite-magnetite buffers) for 24 hours in a $CO-CO_2$ gas-mixing furnace to reduce all Fe^{3+} to Fe^{2+}. An $(Mg_{0.9}Fe_{0.1})(Si_{0.9}Al_{0.1})O_3$ orthopyroxene was then synthesized by equilibrating the stoichiometric mixture of MgO, SiO_2, FeO and Al_2O_3 in a graphite capsule at 2 GPa and 1673 K for 3 days in a piston cylinder apparatus. A Mössbauer spectrum of this sample shows all iron in orthopyroxene to be Fe^{2+} (Fig. 2.1). Several milligrams of the orthopyroxene were packed into a rhenium capsule and equilibrated at 26.5 GPa and 2023 K for 30 minutes with a multi-anvil apparatus by using methods described by Bertka and Fei (1997). The recovered run product was crushed between two tungsten carbide (WC) anvils at 77 K to minimize back transformation or amorphization. The average composition of the synthesized Al-Bm, determined with the JEOL 8900 electron microprobe at the Geophysical Laboratory, is $Mg_{0.868(11)}Fe^{2+}_{0.087(5)}Si_{0.944(10)}Al_{0.101(3)}O_{2.994}$ as formulated on the two-cation basis and assuming all iron to be ferrous. The structure and purity of the run product were further confirmed by an energy-dispersive powder X-ray diffraction (XRD) pattern collected at the GSECARS of the Advanced Photon Source, Argonne National Laboratory, and by a Raman spectrum collected at the Geophysical Laboratory, which matched the existing references (Bertka and Fei 1997). Ferropericlase was not detected in the electron microprobe, or XRD measurements. The absence of ferropericlase is consistent with the excess SiO_2 in the starting composition and the presence of a smaller amount of stishovite in the run product.

2.3.2 Conventional Mössbauer Spectroscopy

Mössbauer spectra of Al-Bm were acquired at temperatures between 65 and 300 K at the Geophysical Laboratory, following the method described in Fei et al. (1994). A closed-cycle refrigerator was used to generate cryogenic temperatures. For Mössbauer measurements, a 0.5" or ~12 mm-diameter pellet was prepared by mixing the crushed sample with transoptic binder, which was sandwiched between two sheets of high-purity alumina foil. This sample was placed between the faces of two Cu discs with a 0.75-in or ~ 19 mm aperture, each lined with indium foil and attached to the cold finger of the cryostat. Temperature was monitored with a chromel-alumel thermocouple next to the sample. An Austin Science Drive operating in the constant acceleration mode produced velocities in the range of ±4 mm/s. The Mössbauer absorption intensity was collected over 512 channel in a mirror-imaged mode. The velocity-channel relation was calibrated using the inner four lines of the stainless steel sextet. The gamma-ray source was a 30 mCi Co in Pd matrix. Spectra were first collected at the lowest temperature of 65 K, and then at progressively higher temperature until reaching the room temperature.

2.4 Results and Discussions

The Mössbauer spectra (Fig. 2.2) do not show evidence of metallic Fe, which would produce a sextet associated with magnetic Zeeman splitting. The absence of metallic Fe was also indicated from examination of electron back-scattered images. Accordingly, we fitted the spectra by multiple doubles with Lorentzian line shape using the fitting program “MossA” (Prescher et al. 2012).

To account for the main feature of each spectrum (Fig. 2.2), we first introduced two doublets with distinct quadruple splitting (QS) values, corresponding to one Fe^{2+} site and one Fe^{3+} site, respectively. The broad and asymmetric absorption peaks near -1 mm/s and 2 mm/s suggest the presence of a second Fe^{2+} doublet. A small peak near 3 mm/s requires a third Fe^{2+} doublet with unusually large quadrupole splitting value, exceeding 4 mm/s. The central shift (CS) of the Fe^{2+}III doublet is well constrained and its value falls into the range of CS for Fe^{2+} in minerals (Dyar et al. 2006). The Fe^{2+}II doublet has an anomalously large width. Treatment of this doublet with a Voigt-based function involving correlated QS and CS distributions (Lagarec and Rancourt 1997) did not improve the fits based on the F test. We chose, therefore, to keep Fe^{2+}II as a Lorentzian doublet. The line shape of Fe^{2+}II did not affect its own hyperfine parameters but influenced those of Fe^{3+} because the low-velocity peak of the Fe^{3+} doublet overlaps with other peaks. The Fe^{2+}II doublet are broader than those reported in the literature (e.g., Fei et al. 1994). With the maximum full width at half maximum (FWHM) of the Fe^{2+}II constrained to a typical value of 0.6 mm/s, the derived Fe^{3+}/Fe ratio decreases by 10% between 65 K and 300 K. This approach is discarded because the valence state of iron is unlikely to change under the cryogenic conditions. We interpret the broad line widths as a manifestation of complexity in the local electronic environment of iron site (Bengtson et al. 2009). With increasing temperature, the relative area of the Fe^{2+}II doublet increased at the expense of the Fe^{2+}I doublet and the large QS site (Fe^{2+}III doublet), with the combined area of all three Fe^{2+} sites remaining nearly constant (Fig. 2.3). Previous studies used an additional doublet to fit systematic aberrations near 1.2~1.3 mm/s (Fei et al. 1994; McCammon 1998) and attributed this component to Fe^{2+}-Fe^{3+} electron delocalization. We did not find it necessary to introduce this component. Furthermore, the fitted CS of each site from our fits decreases with increasing temperature (Fig. 2.3 (d)), as expected for the second-order Doppler shift (Fei et al. 1994). The areas of Fe^{3+} and total Fe^{2+} are constant within uncertainties over the temperature range investigated (Table 2.1). All the above evidence supports the conclusion that Fe^{2+}-Fe^{3+} electron delocalization does not happen in the Al-Bm sample examined here.

2.4.1 The Recoil-free Fractions of Fe^{2+} and Fe^{3+} in Al-Bm

As Fe^{2+} and Fe^{3+} have different valence states and may occupy different crystallographic sites, the recoil-free fractions of Fe^{2+} and Fe^{3+}, denoted as f_2 and f_3, respectively, are generally unequal. Knowledge of the recoil-free fractions is necessary to convert the Mössbauer spectral areas of iron sites to their molar fractions. According to the harmonic theory of lattice dynamics, the recoil-free fraction, f (also known as Lamb-Mössbauer factor), decreases with the mean square displacement of the Mössbauer isotope from its equilibrium position $<x^2>$ and depends on the wavelength of the gamma photons, λ, through the equation $f = \exp(-4p^2 <x^2>/\lambda^2)$ (Frauenfelder 1962). By using the Debye approximation for lattice vibration, the recoil free fraction at a given temperature $f(T)$ is commonly calculated from the characteristic Debye temperature Θ_D according to:

$$f(T) = \exp\left\{-\frac{3}{2}\frac{E_R}{k_B\Theta_D}\left[1 + 4\left(\frac{T}{\Theta_D}\right)^2 \int_0^{\Theta_D/T} \frac{x\,dx}{e^x - 1}\right]\right\}$$

where the recoil energy E_R is 3.13425×10^{-22} J for the 14.4 keV gamma ray from the decay of ^{57}Co to stable ^{57}Fe, and k_B is the Boltzmann constant (Pound and Rebka 1960). Given Mössbauer data at variable temperatures, the Θ_D can be determined by fitting the temperature-dependent center shift $\delta(T)$ to the following relation:

$$\delta(T) = \delta_I - \frac{9}{2}\frac{k_B T}{Mc}\left(\frac{T}{\Theta_D}\right)^3 \int_0^{\Theta_D/T} \frac{x^3\,dx}{e^x - 1}$$

Where δ_I is the intrinsic isomer shift, M is the mass of the Mössbauer nucleus, and c is the velocity of light in vacuum. For the Al-Bm sample, we fitted the CS of Fe^{3+}, Fe^{2+}III, and the weighted average of Fe^{2+}I and Fe^{2+}II to the above equation and derived the δ_I and Θ_D values and the corresponding f at 300 K for each site (Fig. 2.3 (d), Table 2.2).

For a given site i, the relation between its molar fraction, x_i, and Mössbauer spectral area fraction, A_i, is $x_i = (A_i/f_i)/\sum(A_i/f_i)$. The recoil free fraction of Fe^{2+} f_2 and that of Fe^{3+} f_3 derived from our data are similar between 65 and 300 K (Table 2.2 and Fig. 2.4). Therefore, the molar fraction of trivalent iron with respect to total iron (Fe^{3+}/Fe = 46±2%) is indistinguishable from its spectral area fraction of 49±2% (Table 2.1). According to the Debye model, both f_2 and f_3 of the Al-Bm become considerably smaller and diverge from each other at higher temperatures (Fig. 2.4). At 900 K, the calculated f_3 is 46% higher than f_2, implying that the molar fraction of Fe^{3+} is only 41% for a measured spectral area fraction of 50%, and that the area fractions of iron sites may change with temperature without any changes in the valence state or spin state of iron.

2.4.2 Crystal Chemistry

Knowledge of the site occupancy of iron in Bm is essential to understand the chemistry and physics of the lower mantle, including the nature of spin crossover and the mechanism of thermal and electrical conduction (e.g. Badro 2014; Li 2007; Lin et al. 2013). According to experimental observations and atomistic calculations, Fe^{2+} occupies the pseudo-dodecahedral or A site through simple substitution: $Fe^{2+}{}_A = Mg^{2+}{}_A$ (e.g., Wright and Price, 1989). A number of mechanisms have been proposed for the site occupancy of Fe^{3+} (Frost and Langenhorst 2002; Frost et al. 2004; Lauterbach et al. 2000; Hummer and Fei 2012). Given the knowledge of chemical composition and the Fe^{3+} fraction we may use the $(Fe,Mg)_2O_2$-$(Fe^{3+},Al)_2O_3$-Si_2O_4 ternary diagram to infer the site occupancies of Fe^{3+} in Bm (Fig. 2.5). In compositions that plot along the $(Fe^{3+},Al)_2O_3$ and $(Mg,Fe^{2+})SiO_3$ join, Fe^{3+} may enter either the A site or the octahedral B site through substitution of two trivalent ions for Mg^{2+} in the A site and Si^{4+} in the B site: $Mg^{2+}{}_A + Si^{4+}{}_B = Fe^{3+}{}_A + (Fe^{3+},Al^{3+})_B$, known as the coupled substitution mechanism. In compositions showing oxygen deficiency, Fe^{3+} may have substituted for Si^{4+} in the B site and is charge-balanced by introducing a vacancy in the oxygen site (V_O): $2Si^{4+} + O^{2-} = 2Fe^{3+} + V_O$, known as the oxygen vacancy substitution mechanism. For compositions with excess oxygen, Fe^{3+} may have substituted for Mg^{2+} in the A site and is charge-balanced by removing an extra Mg^{2+} which produces an apparent excess in oxygen: $2Fe^{3+} = 3Mg^{2+}$, known as the cation vacancy substitution mechanism. As an alternative to removing an extra Mg^{2+}, charge balance may be maintained by introducing an interstitial oxygen, which is considered energetically unfavorable (Smyth 1993).

Bm compositions that were synthesized at different pressure and temperature conditions spread over a broad range in the $(Fe,Mg)_2O_2$-$(Fe^{3+},Al)_2O_3$-Si_2O_4 ternary diagram, indicating variable site occupancy of iron in the structure (Fig. 2.5). This is consistent with the previous findings that the synthesis condition influences the volume and compressibility of Bm, as well as its spin-pairing transition behavior (Catalli et al. 2010; Fujino et al. 2012; Hummer and Fei 2012; Lundin et al. 2008).

Using the ternary diagram, we infer that most Al-free Bm compositions in the literature involve a combination of coupled substitution and cation vacancy substitution. Those synthesized in very oxidizing environment are exceptions and scattered significantly in this plot (Hummer and Fei 2012). Relatively large uncertainty in Fe^{3+} content also results in wide scatter (Frost and Langenhorst 2002).

The situation is more complex in Al-Bm (Frost et al. 2004; Richmond and Brodholt 1998). Whereas the majority of Al-Bm involve the oxygen vacancy substitution and coupled substitution mechanisms (Fig. 2.5), the Al-Bm sample from our study and that of Narygina et al. (2009) plot between the joins (2) and (3), indicating that some trivalent cations entered the structure through the cation vacancy mechanism. Richmond and Brodholt (1998) showed that the most favorable mechanism to incorporate trivalent cations in the Bm structure is through the coupled substitution ${Mg^{2+}}_A + {Si^{4+}}_B = {Fe^{3+}}_A + {Al^{3+}}_B$, where Fe^{3+} and Al^{3+} substitute into adjacent sites. Given that the Al^{3+}/Fe^{3+} ratio of the Al-Bm is larger than one, we infer that all the Fe^{3+} occupies the A site, coupled with an equal fraction of Al^{3+} in the B site. Because the Mg/Si ratio of the sample is smaller than one, some of the remaining Al^{3+} may adopt the A site through the cation vacancy mechanism in order to approach an equal distribution of cations in the two sites. The inferred occupancy of Fe^{3+} in the A site alone is consistent with the narrow width of the corresponding doublet (Fig. 2.2 and Table 2.1), and with the absence of Fe^{n+} in our sample. Previous studies interpreted Fe^{n+} as a result of electron hopping between Fe^{2+} and Fe^{3+}, which likely occurs between the adjacent A and B sites the cation-cation distance falling within the range for electron hopping in oxides and silicates (Fei et al. 1994, McCammon 1998). In contrast, the cation-cation distance between adjacent A sites is marginally within the range of electron hopping and hence less likely to occur. Note that the presence of Fe^{3+} in the Al-Bm cannot be inferred from the composition alone because its influence on the cation to oxygen ratio depends on how trivalent ions are incorporated in the structure: The ratio would exceed the stoichiometric value of 2 to 3 if trivalent ions preferentially enters the A site, fall below the value if they preferentially enters the B site, or does not change if all trivalent ions enters both sites in equal proportion through the coupled substitution mechanism.

2.4.3 Debye Temperature

Even though the physical meaning of Debye temperature Θ_D, derived from Mössbauer measurements, is not fully understood, it is generally accepted that it can be used to compare the strength of chemical bonding among structurally related compounds (De Grave et al. 1985). McCammon (1998) reported the Debye temperatures of an Al-free Bm (Table 2.2). We were able to exactly reproduce the results, thus confirming the validity of the fitting procedure. Compared with the Al-free Bm, the Debye temperatures of Fe^{2+} and Fe^{3+} in the Al-Bm are lower by 17% and 24%, respectively, resulting in f_2 and f_3 values at 300 K that differs by 13 % (Table 2.2). The lower Debye temperatures in Al-Bm are consistent with the finding that substituting larger Al^{3+} ion for smaller Si^{4+} ion in the B site expands its volume and increases the average bond length (Lundin et al. 2008; Vanpeteghem et al. 2006). Moreover, this substitution causes tilting of the octahedra, therefore, inflates the A site. The elongated and weakened Fe-O bond then give rise to the lower Debye temperatures and smaller recoil free fractions, f_2 and f_3, in Al-Bm.

One intriguing phenomenon is that the fitted Debye temperature of the Fe^{2+}III site exceeds 1000 K (Table 2.2) and is more than twice the highest value reported in the literature (De Grave and Van Alboom 1991). Unlike the very large values of Debye temperatures for Fe^{2+} in Al-free Bm samples (Fei et al. 1994), which have been attributed to fitting artifacts (McCammon 1998), the unusually high Debye temperature is a robust feature because the CS values of the Fe^{2+}III doublets are well constrained by the Mössbauer data. Theoretical calculations have shown that at 0.1 MPa two high-spin (HS) Fe^{2+} sites with distinct QS values exist in the A site of Bm, and the one with a large QS value (~ 3.2 mm/s) has a shorter average bond length (Bengtson et al. 2009; Hsu et al. 2010). This is consistent with the observation that Fe^{2+}III with large QS has extraordinarily high Debye temperatures, reflecting its short bond length and high bond strength.

2.4.4 The Fe^{2+} Site with Large QS

Recent Mössbauer studies detected Fe^{2+} sites with extremely large QS values (~4.0 mm/s) at pressures above 30 GPa (Kupenko et al. 2014; Lin et al. 2008; McCammon et al. 2008; Narygina et al. 2010; Potapkin et al. 2013). These values were interpreted to be the results of intermediate-spin (IS) Fe^{2+} according to the spin numbers derived from X-ray emission spectroscopy data (Lin et al. 2008), or attributed to high-spin (HS) Fe^{2+} (Grocholski et al. 2009; Jackson et al. 2005; Li et al. 2004, 2006; Lin et al. 2012). Theoretical calculations suggested that IS Fe^{2+} is unstable relative to HS or low-spin (LS) Fe^{2+} and that the QS of the intermediate-spin Fe^{2+} in the A site falls into the range of 0.7 to 1.4 mm/s, which is well below 4.0 mm/s (Bengtson et al. 2009; Hsu et al. 2010). Additionally, these studies showed that HS Fe^{2+} in the A site could have high QS (3.2-3.6 mm/s) due to difference in d-orbital occupation and local distortion.

In the Al-Bm, the Fe^{2+}III site has similar QS-values (3.47-4.03 mm/s) and CS-values (~1.1 mm/s) to those proposed for IS Fe^{2+} (Kupenko et al. 2014; Lin et al. 2008; McCammon et al. 2008; Narygina et al. 2010; Potapkin et al. 2013), and its area fraction in the Mössbauer absorption spectra decreased with temperature from 6% at 65 K to near 0% at 300 K (Table 2.1). It is generally understood that the high-spin state is favored at low pressures and/or high temperatures. A potential explanation for the large QS and temperature dependence of the Fe^{2+}

III site is, therefore, that it represents an IS or LS-site at low temperatures, which transforms to a HS state as temperature rises. To test this hypothesis, we estimated the temperature of spin-pairing transition at 0.1 MPa, on the basis of simplified crystal field theory and existing data on pressure-induced spin-pairing transition in Bm at 300 K. The spin transition at 65 K is expected to take place below 30 GPa as a result of the entropy difference between IS (or LS) and HS iron (dS) and thermal contraction. By assuming the crystal field splitting energy (CFSE), D, relates to the Fe-O bond length, R, through $D \sim R^{-5}$ (Burns 1993) and ignoring the volume difference between the adjacent spin states (Catalli et al. 2010; Lundin et al. 2008), for a temperature drop of dT, the spin transition pressure would decrease by $dT \bullet dS/(5\mathrm{n}D/3K_\mathrm{T})$ because of the entropy difference, and by $(\mathrm{a}K_\mathrm{T}dT)_\mathrm{V}$ because of thermal contraction, where n is the number of electrons that flip spin through the transition, K_T is the isothermal bulk modulus, and a is the isobaric thermal expansion coefficient. By using the parameters in Li (2007), we found that the pressure of HS to LS transition of Fe^{2+} at 65 K is 1.7 GPa lower than that at 300 K, where 0.4 GPa is from the entropy and 1.3 GPa from thermal contraction. From HS to IS, the transition pressure at 65 K is 3.1 GPa lower, where 1.8 GPa comes from the entropy effect and 1.3 GPa from the thermal contraction effect. Given the pressures of spin transitions in Bm at 300 K range from 30 to 120 GPa (e.g., Badro et al. 2004; Fujino et al. 2012; Catalli et al. 2010; McCammon et al. 2010; Jackson et al. 2005; Li et al. 2006), and that these pressures would only be lowered by a few GPa, we conclude that the Fe^{2+}III site represents a HS state and that the large QS likely result from temperature-induced change in the degree of lattice distortion (Bengtson et al. 2009; Hsu et al. 2010).

2.5 Implications

For an Al- and Fe-bearing Bm sample with a composition that is applicable to the Earth's lower mantle, we found that the recoil-free fractions of Fe^{2+} and Fe^{3+} at 300 K are 0.637 and 0.72, respectively. These values are sufficiently similar so that the molar fractions of the two ions can be roughly equated to the area fractions of their respective Mössbauer doublet. By using the fitted Debye temperatures to calculate the recoil-free fractions at different temperatures we expect the recoil-free fraction of Fe^{3+} at 900 K to be 46% higher than that of Fe^{2+} because of different temperature dependence, thus requiring a downward correction to calculate the molar fraction of Fe^{3+} from its area fraction in the Mössbauer spectra.

Contrary to some of the recent studies that interpreted exceptionally large QS value as a diagnostic feature of intermediate spin state of iron in Bm, we observed a Fe^{2+} component with a large QS near 4.0mm/s at 1 bar and below 250 K, which supports the theoretical prediction of large QS resulting from distortion rather than spin-crossover.

Our analyses of a large number of Bm samples reported in the literature suggest that site occupancy of Fe^{3+} depends on Al content and synthesis conditions: Whereas the majority of the Al-free samples can be explained by a combination of coupled substitution and cation vacancy substitution, a combination of coupled substitution and oxygen vacancy mechanism is inferred for most of the Al-bearing samples.

The geophysical estimate of the lower-mantle electric conductivity has been adequately explained by the Bm component (e.g., Katsura et al. 1998). It was shown that at temperatures up to 1500 K conduction mechanism was dominated by Fe^{2+}-Fe^{3+} electron hopping with relatively small activation energy, whereas at higher temperatures the dominant mechanism is ionic conduction through A site vacancies and oxygen vacancies, which involves larger activation energy (Katsura et al. 1998; Xu and McCammon 2002). In the Al-Bm at 300 K examined here, Fe^{3+} was found to exclusively enter the pseudo-dodecahedral A site through the coupled substitution mechanism, which is consistent with the Mössbauer results that indicate no electron hopping. Accordingly the Al-Bm is expected to have low electric conductivity at ambient conditions. A recent study on spin crossover suggested that at pressures above 50-60 GPa and high temperatures, Fe^{3+} in the A site exchanged with Al^{3+} in the B sites and transitioned to the low-spin state (Fujino et al. 2012). Such migration would enable electron hopping between Fe^{2+} in the A site and low-spin Fe^{3+} in the B site and therefore lower the activation energy and increase the electric conductivity of the Al-Bm.

Table 2.1. Hyperfine parameters of $Mg_{0.868}Fe_{0.087}Si_{0.944}Al_{0.101}O_{2.994}$ bridgmanite at 1 bar.

	Fe^{2+}I				Fe^{2+}II			
T	QS	CS	FWHM	A^a	QS	CS	FWHM	A^a
(K)	(mm/s)	(mm/s)	(mm/s)	(%)	(mm/s)	(mm/s)	(mm/s)	(%)
65	2.80(2)	1.051(6)	0.44(4)	31(4)	1.8(5)	1.17(5)	1.2(3)	14(7)
100	2.76(1)	1.039(4)	0.37(3)	27(2)	1.8(1)	1.13(2)	0.9(1)	20(3)
150	2.72(2)	1.004(4)	0.38(3)	23(3)	1.80(8)	1.09(1)	0.76(6)	25(3)
200	2.67(2)	0.962(5)	0.36(4)	17(3)	1.78(6)	1.048(8)	0.73(4)	33(3)
250	2.61(3)	0.924(9)	0.36(6)	11(3)	1.78(6)	1.000(8)	0.75(4)	39(3)
300	2.55(4)	0.89(1)	0.32(9)	5(3)	1.72(4)	0.956(7)	0.75(3)	44(2)

	Fe^{2+}III				Fe^{3+}				
T	QS	CS	FWHM	A^a	QS	CS	FWHM	A^a	$Fraction^b$
(K)	(mm/s)	(mm/s)	(mm/s)	(%)	(mm/s)	(mm/s)	(mm/s)	(%)	(%)
65	4.03(3)	1.11(2)	0.34(7)	6(1)	0.89(1)	0.407(7)	0.52(1)	49(5)	46(5)
100	3.97(3)	1.12(1)	0.32(5)	6(1)	0.897(8)	0.397(5)	0.449(9)	48(3)	45(3)
150	3.86(4)	1.11(2)	0.30(6)	4(1)	0.898(9)	0.372(5)	0.439(9)	48(2)	48(2)
200	3.74(5)	1.11(2)	0.28(8)	3(1)	0.902(9)	0.339(5)	0.437(9)	47(2)	44(2)
250	3.55(5)	1.09(2)	0.20(8)	1(1)	0.91(1)	0.306(6)	0.47 (1)	48(3)	45(3)
300	3.47(9)	1.06(4)	0.2(1)	1(1)	0.91(1)	0.306(6)	0.47 (1)	48(3)	46(2)

CS: Center shift. QS: Quadruple splitting. FWHM: Full width at half maximum.

[a] Area Fractions. [b] Molar fractions. Numbers in parentheses represent fitting errors.

Table 2.2. Debye parameters and recoil-free fractions of bridgmanites at 1 bar.

Site	Composition	Θ_D (K)	δ_I (mm/s)	$f_{300\ \mathrm{K}}$
Fe^{2+}	**Fe_9Al_{10} (this study)**	**305(3)**	**1.096(5)**	**0.637(6)**
	Fe_{10} (Fei)	233	1.304	0.47
	Fe_5 (Fei)	405	1.264	0.77
	Fe_5 (McC)	366	1.259	0.73
Fe^{2+} large QS	**Fe_9Al_{10} (Liu)**	**1102(114)**	**1.115(4)**	**0.956(4)**
Fe^{3+}	**Fe_9Al_{10} (this study)**	**361(22)**	**0.412(4)**	**0.72(2)**
	Fe_{10} (Fei)	1553	0.426	0.97
	Fe_5 (Fei)	1366	0.430	0.97
	Fe_5 (McC)	476	0.426	0.82

Θ_D: Debye temperature. δ_I: Intrinsic isomer shift. $f_{300\ \mathrm{K}}$: recoil-free fraction at 300 K.

Numbers in parentheses represent fitting errors.

Data sources: Fe_9Al_{10}(this study): $Mg_{0.868}Fe_{0.087}Si_{0.944}Al_{0.101}O_{2.994}$ from this study;

Fe_5 (Fei) and Fe_{10} (Fei): $Mg_{0.95}Fe_{0.05}SiO_3$ and $Mg_{0.90}Fe_{0.10}SiO_3$, respectively (Fei et al. 1994);

Fe_5 (McC): $Mg_{0.95}Fe_{0.05}SiO_3$ (McCammon 1998).

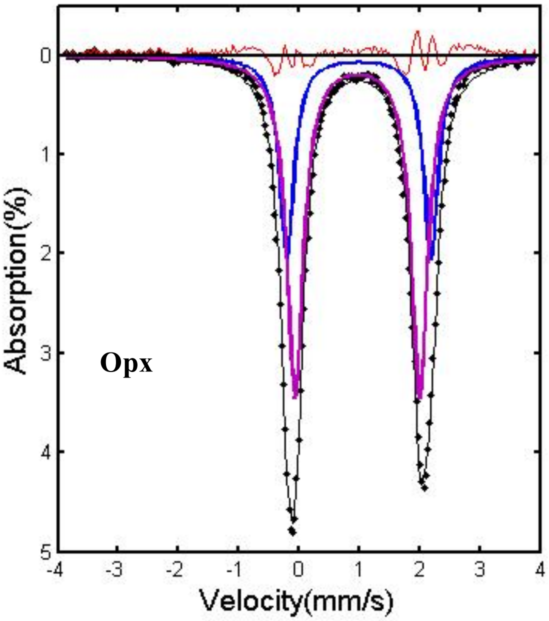

Figure 2.1. The ^{57}Fe Mössbauer spectrum of the starting orthopyroxene sample $(Mg_{0.9}Fe_{0.1})(Si_{0.9}Al_{0.10})O_3$ at room temperature. Quadrupole doublets are colored as follows: Fe^{2+} in M_1 site, blue; Fe^{2+} in M_2 site, pink. Solid circles: experimental data; thin black line: model spectra; red line: residual.

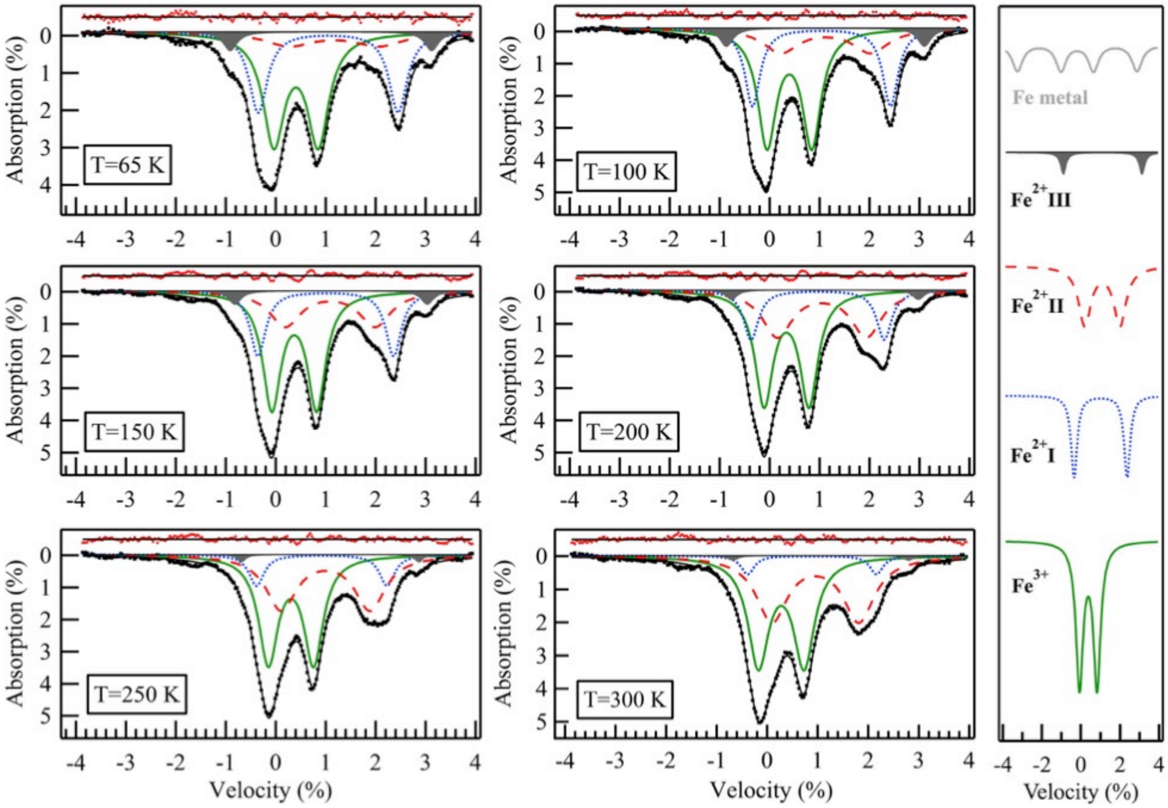

Figure 2.2. Mössbauer spectra of $Mg_{0.868}Fe_{0.087}Si_{0.944}Al_{0.101}O_{2.994}$ bridgmanite between 65 K and 300 K at 1 bar. Each spectrum (black dots) was fitted by four doublets (black envelop): Fe^{3+} (green solid), Fe^{2+}I (blue dotted), Fe^{2+}II (red dashed) and Fe^{2+}III (gray filled). Red dots represent the fitting residual. Within the velocity range of our measurements, a sextet from metallic Fe would consist of peaks near -3.0, -1.0, 1.0, and 3.0 mm/s.

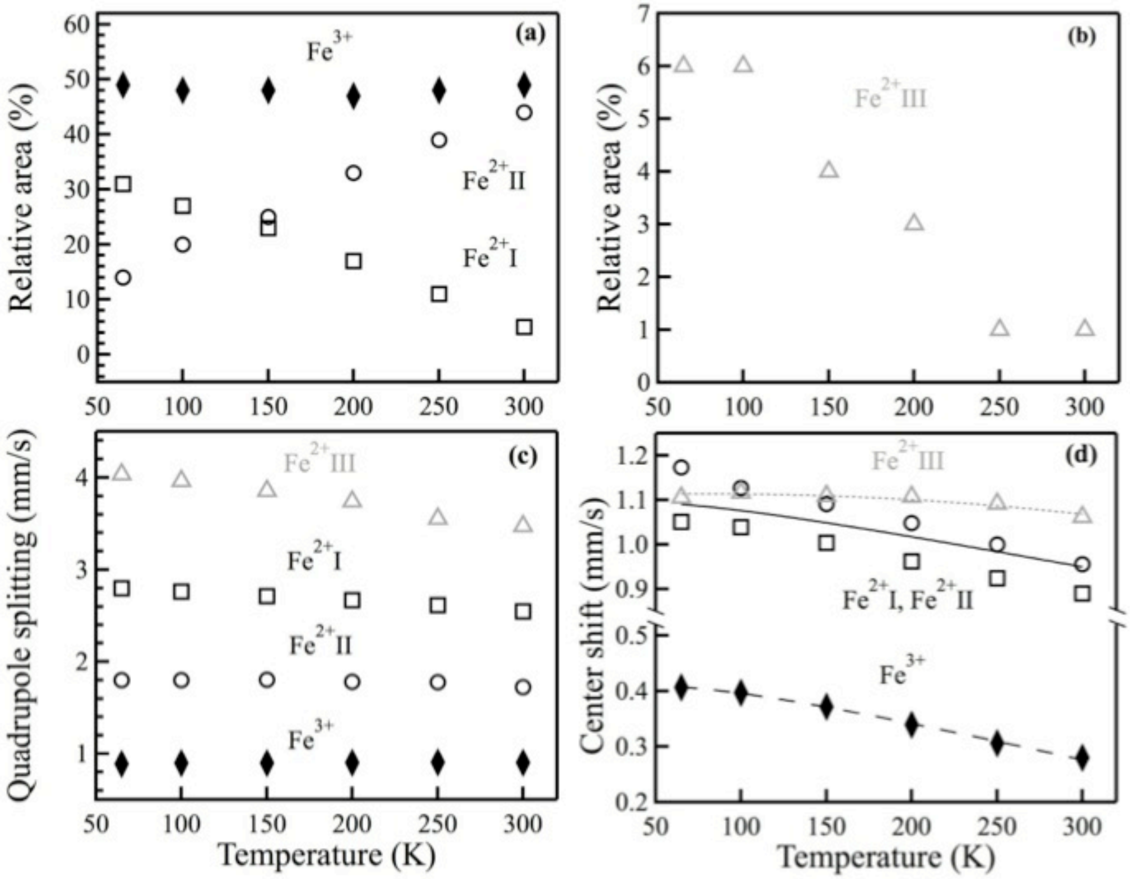

Figure 2.3. Area fractions (a, b) and hyperfine parameters (c, d) of iron sites in bridgmanite $Mg_{0.868}Fe_{0.087}Si_{0.944}Al_{0.101}O_{2.994}$ as a function of temperature at 1 bar. The iron sites include Fe^{2+}I (open squares), Fe^{2+}II (open circles), Fe^{2+}III (gray triangles), and Fe^{3+}(solid diamonds). In (d), the curves represent the Debye model fittings for the weighted average of Fe^{2+}I and Fe^{2+}II (solid), Fe^{2+}III (dashed), and Fe^{3+}(gray dotted).

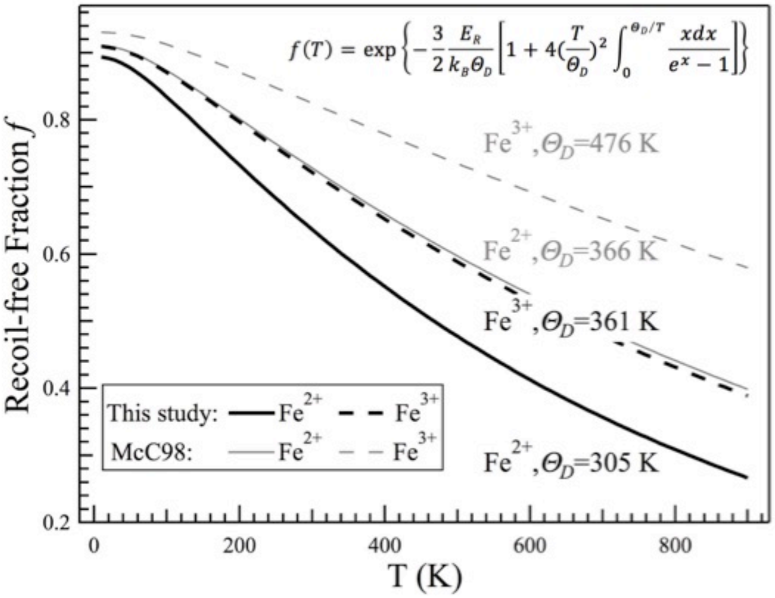

Figure 2.4. Calculated recoil-free fractions as a function of temperature, according to the Debye model. Black solid and dashed curves represent Fe^{2+} and Fe^{3+}, respectively, in Al-Bm from this study; Gray solid and dashed curves represent Fe^{2+} and Fe^{3+}, respectively, in Al-free Bm from McCammon (1998).

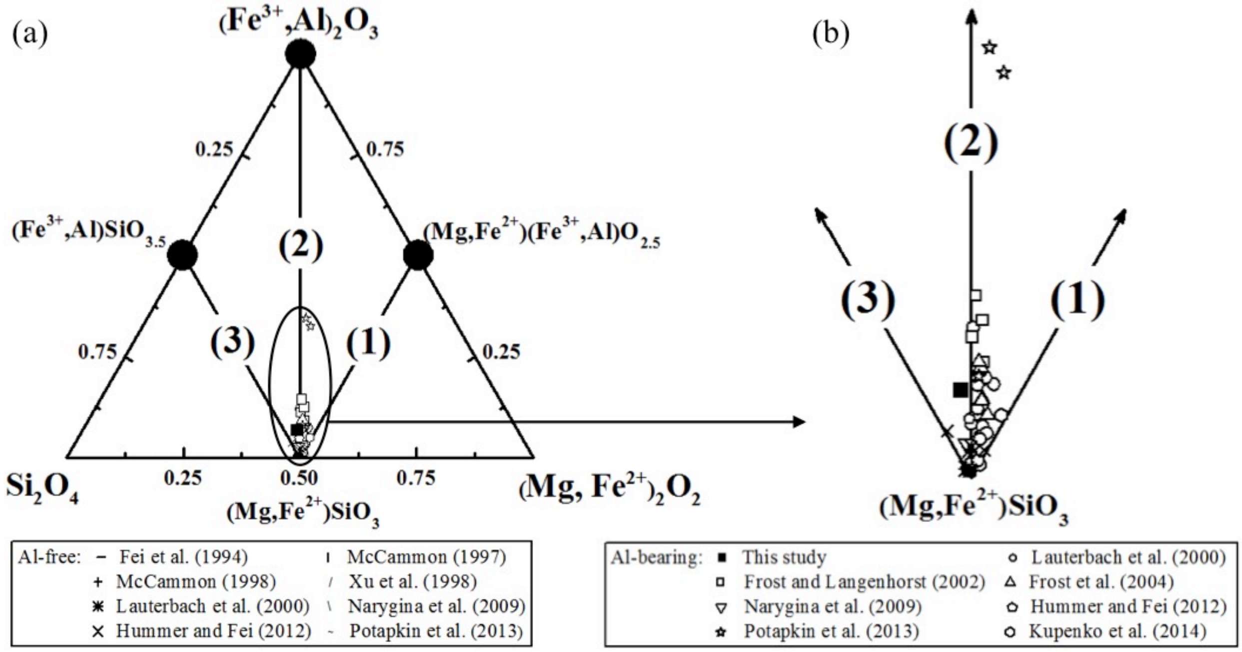

Figure 2.5. Ternary diagram illustrating the cation substitution mechanisms in bridgmanite in full compositional range (a) and a close-up (b). The end-member compositions Si_2O_4, $(Mg,Fe^{2+})_2O_2$, and $(Fe^{3+},Al)_2O_3$ are written on the two-cation basis. Lines connecting the trivalent-cation-free composition $(Mg, Fe^{2+})SiO_3$ to each of the three trivalent-bearing compositions represent (1) $(Mg,Fe^{2+})(Fe^{3+},Al)O_{2.5}$, oxygen vacancy substitution mechanism, (2) $(Fe^{3+},Al)_2O_3$, coupled substitution mechanism, and (3) $(Fe^{3+},Al)SiO_{3.5}$, cation vacancy substitution mechanism. Open and closed symbols represent Al-free and Al-bearing compositions, respectively. Error bars in this study are smaller than the symbol size. More complex compositions including cations other than Mg, Si, Al, and Fe are not included.

2.6 References

Badro, J. (2014) Spin transitions in mantle minerals. Annual Review of Earth and Planetary Sciences, 42, 231-248.

Badro, J., Rueff, J.P., Vanko, G., Monaco, G., Fiquet, G., and Guyot, F. (2004) Electronic transitions in perovskite: possible nonconvecting layers in the lower mantle. Science, 305, 383-386.

Bengtson, A., Li, J., and Morgan, D. (2009) Mössbauer modeling to interpret the spin state of iron in (Mg,Fe)SiO_3 perovskite. Geophysical Research Letters, 36, L15301.

Bertka, C. M., and Y. Fei (1997) Mineralogy of the Martian interior up to core-mantle boundary pressures, J. Geophys. Res., 103, 5251-5264.

Burns, R.G. (1993) Mineralogical Applications of Crystal Field Theory, Seond ed., Cambridge University Press, Cambridge, p. 551.

Catalli, K., Shim, S.H., Prakapenka, V.B., Zhao, J.Y., Sturhahn, W., Chow, P., Xiao, Y.M., Liu, H.Z., Cynn, H., and Evans, W.J. (2010) Spin state of ferric iron in $MgSiO_3$ perovskite and its effect on elastic properties. Earth and Planetary Science Letters, 289, 68-75.

De Grave, E., and Van Alboom, A. (1991) Evaluation of ferrous and ferric Mössbauer fractions. Physics and Chemistry of Minerals, 18, 337-342.

De Grave, E., Verbeeck, A.E., and Chambaere, D.G. (1985) Influence of small aluminum substitutions on the hematite lattice. Physics Letters A, 107, 181-184.

Dyar, M.D., Agresti, D.G., Schaefer, M.W., Grant, C.A., and Sklute, E.C. (2006) Mössbauer spectroscopy of earth and planetary materials. Annual Review of Earth and Planetary Sciences, 34, 83-125.

Fei, Y., Virgo, D., Mysen, B.O., Wang, Y., and Mao, H.K. (1994) Temperature-dependent electron delocalization in (Mg,Fe)SiO_3 perovskite. American Mineralogist, 79, 826-837.

Frauenfelder H. 1962. The Mössbauer effect. New York: WA Benjamin, p. 333.

Frost, D.J., and Langenhorst, F. (2002) The effect of Al_2O_3 on Fe-Mg partitioning between magnesiowustite and magnesium silicate perovskite. Earth and Planetary Science Letters, 199, 227-241.

Frost, D.J., Liebske, C., Langenhorst, F., McCammon, C.A., Tronnes, R.G., and Rubie, D.C. (2004) Experimental evidence for the existence of iron-rich metal in the Earth's lower mantle. Nature, 428, 409-412.

Fujino, K., Nishio-Hamane, D., Seto, Y., Sata, N., Nagai, T., Shinmei, T., Irifune, T., Ishii, H., Hiraoka, N., Cai, Y.Q., and Tsuei, K.D. (2012) Spin transition of ferric iron in Al-bearing Mg-perovskite up to 200 GPa and its implication for the lower mantle. Earth and Planetary Science Letters, 317, 407-412.

Grocholski, B., Shim, S.H., Sturhahn, W., Zhao, J., Xiao, Y., and Chow, P.C. (2009) Spin and valence states of iron in $(Mg_{0.8}Fe_{0.2})SiO_3$ perovskite. Geophysical Research Letters, 36, L24303.

Hsu, H., Umemoto, K., Blaha, P., and Wentzcovitch, R.M. (2010) Spin states and hyperfine interactions of iron in (Mg,Fe)SiO_3 perovskite under pressure. Earth and Planetary Science Letters, 294, 19-26.

Hummer, D.R., and Fei, Y.W. (2012) Synthesis and crystal chemistry of Fe^{3+}-bearing $(Mg,Fe^{3+})(Si,Fe^{3+})O_3$ perovskite. American Mineralogist, 97, 1915-1921.

Jackson, J.M., Sturhahn, W., Shen, G.Y., Zhao, J.Y., Hu, M.Y., Errandonea, D., Bass, J.D., and Fei, Y.W. (2005) A synchrotron Mössbauer spectroscopy study of (Mg,Fe)SiO_3 perovskite up to 120 GPa. American Mineralogist, 90, 199-205.

Katsura, T., Sato, K., Ito, E., 1998. Electrical conductivity of silicate perovskite at lower-mantle conditions. Nature 395, 493-495.

Kupenko, I., McCammon, C., Sinmyo, R., Prescher, C., Chumakov, A.I., Kantor, A., Ruffer, R., and Dubrovinsky, L. (2014) Electronic spin state of Fe,Al-containing $MgSiO_3$ perovskite at lower mantle conditions. Lithos, 189, 167-172.

Lagarec, K., and Rancourt, D.G. (1997) Extended Voigt-based analytic lineshape method for determining N-dimensional correlated hyperfine parameter distributions in Mössbauer spectroscopy. Nuclear Instruments & Methods in Physics Research Section B-Beam Interactions with Materials and Atoms, 129, 266-280.

Lauterbach, S., McCammon, C.A., van Aken, P., Langenhorst, F., and Seifert, F. (2000) Mössbauer and ELNES spectroscopy of (Mg,Fe)(Si,Al)O_3 perovskite: a highly oxidised component of the lower mantle. Contributions to Mineralogy and Petrology, 138, 17-26.

Li, J., Struzhkin, V.V., Mao, H.K., Shu, J.F., Hemley, R.J., Fei, Y.W., Mysen, B., Dera, P., Prakapenka, V., and Shen, G.Y. (2004) Electronic spin state of iron in lower mantle perovskite. Proceedings of the National Academy of Sciences of the United States of America, 101, 14027-14030.

Li, J., Sturhahn, W., Jackson, J.M., Struzhkin, V.V., Lin, J.F., Zhao, J., Mao, H.K., and Shen, G. (2006) Pressure effect on the electronic structure of iron in (Mg,Fe)(Si,Al)O_3 perovskite: a combined synchrotron Mössbauer and X-ray emission spectroscopy study up to 100 GPa. Physics and Chemistry of Minerals, 33, 575-585.

Li, J. (2007) Electronic transitions and spin states in the lower mantle. Post-perovskite: the last mantle phase transition, 174, 47-68.

Lin, J.F., Alp, E.E., Mao, Z., Inoue, T., McCammon, C., Xia, Y.M., Chow, P., and Zhao, J.Y. (2012) Electronic spin states of ferric and ferrous iron in the lower-mantle silicate perovskite. American Mineralogist, 97, 592-597.

Lin, J.F., Watson, H., Vanko, G., Alp, E.E., Prakapenka, V.B., Dera, P., Struzhkin, V.V., Kubo, A., Zhao, J.Y., McCammon, C., and Evans, W.J. (2008) Intermediate-spin ferrous iron in lowermost mantle post-perovskite and perovskite. Nature Geoscience, 1, 688-691.

Lin, J.F., Speziale, S., Mao, Z., and Marquardt, H. (2013) Effects of the electronic spin transitions of iron in lower mantle minerals: implications for deep mantle geophysics and geochemistry. Reviews of Geophysics, 51, 244-275.

Lundin, S., Catalli, K., Santillan, J., Shim, S.H., Prakapenka, V.B., Kunz, M., and Meng, Y. (2008) Effect of Fe on the equation of state of mantle silicate perovskite over 1 Mbar. Physics of the Earth and Planetary Interiors, 168, 97-102.

McCammon, C. (1997) Perovskite as a possible sink for ferric iron in the lower mantle. Nature, 387, 694-696.

McCammon, C. (1998) The crystal chemistry of ferric iron in $Fe_{0.05}Mg_{0.95}SiO_3$ perovskite as determined by Mössbauer spectroscopy in the temperature range 80-293 K. Physics and Chemistry of Minerals, 25, 292-300.

McCammon, C., Kantor, I., Narygina, O., Rouquette, J., Ponkratz, U., Sergueev, I., Mezouar, M., Prakapenka, V., and Dubrovinsky, L. (2008) Stable intermediate-spin ferrous iron in lower-mantle perovskite. Nature Geoscience, 1, 684-687.

McCammon, C., Dubrovinsky, L., Narygina, O., Kantor, I., Wu, X., Glazyrin, K., Sergueev, I., and Chumakov, A.I. (2010) Low-spin Fe^{2+} in silicate perovskite and a possible layer at the base of the lower mantle. Physics of the Earth and Planetary Interiors, 180, 215-221.

Narygina, O.V., Kantor, I.Y., McCammon, C.A., and Dubrovinsky, L.S. (2010) Electronic state of Fe^{2+} in $(Mg,Fe)(Si,Al)O_3$ perovskite and $(Mg,Fe)SiO_3$ majorite at pressures up to 81 GPa and temperatures up to 800 K. Physics and Chemistry of Minerals, 37, 407-415.

Narygina, O.V., Mattesini, M., Kantor, I., Pascarelli, S., Wu, X., Aquilanti, G., McCammon, C., and Dubrovinsky, L. (2009) High-pressure experimental and computational XANES studies of $(Mg,Fe)(Si,Al)O_3$ perovskite and (Mg,Fe)O ferropericlase as in the Earth's lower mantle. Physical Review B, 79, 174115.

Potapkin, V., McCammon, C., Glazyrin, K., Kantor, A., Kupenko, I., Prescher, C., Sinmyo, R., Smirnov, G.V., Chumakov, A.I., Ruffer, R., and Dubrovinsky, L. (2013) Effect of iron oxidation state on the electrical conductivity of the Earth's lower mantle. Nature Communications, 4, 1427.

Pound, R.V., and Rebka, G.A. (1960) Variation with temperature of the energy of recoil-free gamma-rays from solids. Physical Review Letters, 4, 274-275.

Prescher, C., McCammon, C., and Dubrovinsky, L. (2012) MossA: a program for analyzing energy-domain Mössbauer spectra from conventional and synchrotron sources. Journal of Applied Crystallography, 45, 329-331.

Richmond, N.C., and Brodholt, J.P. (1998) Calculated role of aluminum in the incorporation of ferric iron into magnesium silicate perovskite. American Mineralogist, 83, 947-951.

Smyth, D.M. (1993) Oxidative nonstoichiometry in Perovskite oxides. In: Tejuco, L.G., Fierro, J.L.G., Eds., Properties and Applications of Perovskite-Type Oxides, p. 47-72. Marcel Dekker, New York.

Vanpeteghem, C.B., Angel, R.J., Ross, N.L., Jacobsen, S.D., Dobson, D.P., Litasov, K.D., and Ohtani, E. (2006) Al, Fe substitution in the $MgSiO_3$ perovskite structure: a single-crystal X-ray diffraction study. Physics of the Earth and Planetary Interiors, 155, 96-103.

Wood, B.J., and Rubie, D.C. (1996) The effect of alumina on phase transformations at the 660-kilometer discontinuity from Fe-Mg partitioning experiments. Science, 273, 1522-1524.

Wright, K., and Price, G.D. (1989) Computer-Simulations of Iron in Magnesium-Silicate Perovskite. Geophysical Research Letters, 16, 1399-1402.

Xu, Y.S., McCammon, C., and Poe, B.T. (1998) The effect of alumina on the electrical conductivity of silicate perovskite. Science, 282, 922-924.

Xu, Y.S., McCammon, C., 2002. Evidence for ionic conductivity in lower mantle $(Mg,Fe)(Si,Al)O_3$ perovskite. Journal of Geophysical Research, 107, 2251.

Chapter III. "Invar"-like Behavior in Compressed Fe_7C_3 with Implication for the Inner Core

3.1 Abstract

Iron carbide Fe_7C_3 has recently emerged as a leading candidate component of the inner core because it is likely the first phase to solidify from a liquid containing iron and a small amount of carbon, and previous studies suggest that it provides a good match for the density and sound velocity of the inner core under relevant conditions. Pressure-induced magnetic transitions have been observed in Fe_7C_3 but the pressure of the ferromagnetic to paramagnetic transition remains controversial and its effect on equation of state (EoS) is unclear, thus introducing uncertainties in estimating the density of Fe_7C_3 under inner core pressures. Here we report the lattice parameters and unit cell volume of hexagonal Fe_7C_3 at 300 K and up to about 70 GPa, obtained through synchrotron x-ray diffraction measurements using a diamond anvil cell. The new data revealed significant softening near 8 GPa, followed by stiffening near 22 GPa. For comparison, the compression curve of iron in the same loading turned out to be smooth as expected, thus confirming that the abnormal behavior in Fe_7C_3 compression curve reflects its true nature and is not an artifact. The softening at the lower pressure and stiffening at the higher pressure can be attributed to a magnetic ordering transition and a spin crossover, respectively. By extrapolating the established equations-of-state (EoS) to the inner core pressure and accounting for the effect thermal expansion, we found that the non-magnetic phase provides a good match for the observed density, whereas the paramagnetic phase would be denser by 12~13 %.

3.2 Introduction

Carbon has been proposed as a primary light element in the Earth core because it is the fourth cosmochemically abundant element in the solar system, and it has strong affinity with both solid and liquid iron (Wood, 1993). In addition, carbonaceous chondrites, the most primitive planetary material, have 2.5~5.8 wt.% carbon in CI and CM chondrites (e.g. Kerridge, 1985; Mason, 1979). Fe_7C_3, as a major iron carbide, has received broad attention due to its unique physical and chemical properties: experimental studies on Fe-C binary system have shown that Fe_7C_3 stabilizes above 6 GPa (Tsuzuki et al., 1984) and melts incongruently to graphite/diamond and liquid (Fei and Brosh, 2014; Nakajima et al., 2009;Lord et al., 2009). Such phase relation may persist up to Earth inner core pressures, making Fe_7C_3 as the major component in the inner core if several weight percent carbon presented during core formation period (Fei and Brosh, 2014). The density measurement of Fe_7C_3 up to the core's pressures showed that the presence of Fe_7C_3 could explain the density deficit of the inner core compared with pure iron at relevant pressure-temperature conditions (Chen et al., 2012; Nakajima et al., 2011). Besides, sound velocity measurement of compressed Fe_7C_3 found it exhibited low increase rate of sound velocity with pressure, which may explain the anomalously low shear wave velocity observed in the inner core (Chen et al., 2014).

The crystal structures, electronic and magnetic properties of Fe_7C_3 have been investigated experimentally and theoretically. X-ray diffraction studies discovered two crystal structures for Fe_7C_3: one is hexagonal structure with the space group $P6_3mc$ (h-Fe_7C_3), known as Eckstrom-Adcock carbide (Eckstrom and Adcock, 1950). This structure is observed from ambient pressure-temperature condition to relevant conditions of the core (Chen et al., 2012; Herbstein and Snyman, 1964; Nakajima et al., 2011). The other structure is orthorhombic (o-Fe_7C_3), and the space groups can be *Pnma* or *Pmcn* (Fang et al., 2009; Fruchart and Rouault, 1969). These two crystal structures are different polytypes of Fe_7C_3: they have the same structural element, named triads, which is composed of three Fe prisms shared corners and each Fe prism has a C atom in the center, and different arrangements of such triads in the unit cells result in different polytypes of M_7C_3 (M=Fe, Mn and Cr) carbides (Fang et al., 2009; Kowalski, 1985; Senczyk, 1993; Tsuzuki et al., 1984). The relative stability of these two crystal structures is still under debates: atomistic calculations suggested *h*-Fe_7C_3 is more stable (Xie et al., 2005), however, first-principles calculations gave an opposite conclusion (Fang et al., 2009). Both experimental and theoretical studies showed Fe_7C_3 in these two structures is ferromagnetic alloy at 1 bar (Fang et al., 2009; Mookherjee et al., 2011; Tsuzuki et al., 1984) and the curie temperature (Tc) of *h*-Fe_7C_3 is 523 K (Tsuzuki et al., 1984). Under pressures, the magnetic moment of *h*-Fe_7C_3 gradually decreases and magnetic transitions happen: theoretical calculations indicated a ferromagnetic to nonmagnetic transition happens at about 67 GPa and 0 K (Mookherjee et al., 2011); while an experimental study on compression curve of *h*-Fe_7C_3 found a ferromagnetic to paramagnetic transition at about 18 GPa and 300 K (Nakajima et al., 2011). In comparison, another experimental study at 300 K showed two-step magnetic transitions: a ferromagnetic to paramagnetic transition happened between 5.5 and 7.5 GPa, followed by a paramagnetic to nonmagnetic transition at 53 GPa (Chen et al., 2012). In addition, Chen et al. (2012) observed *h*-Fe_7C_3 softening associated with the second magnetic transition, and referred this to Invar behavior. Invar behavior refers to anomalously low thermal expansions found in several Fe alloys, such as alloys of Fe-Ni (Guillaume, 1987), Fe-Pd (Kussmann and Jessen, 1962), further include anomalies in molar volume, bulk modulus, heat capacity, magnetization and others. Under pressures, Fe-Ni Invar alloys exhibited softening within specific pressure ranges, where the bulk modulus dropped (Dubrovinsky et al., 2001; van Schilfgaarde et al., 1999). Such pressure-induced softening in Fe-Ni Invar alloys was observed below 15 GPa (Dubrovinsky et al., 2001; van Schilfgaarde et al., 1999), significantly lower than 53 GPa reported in Chen et al. (2012) for *h*-Fe_7C_3.

To understand the nature of magnetic transitions and their effects on Fe_7C_3, we measured the lattice parameters and unit cell volume of *h*-Fe_7C_3 at 300 K and up to 68 GPa, obtained through synchrotron X-ray diffraction (XRD) measurements using a diamond anvil cell (DAC).

3.3 Experimental Methods

Polycrystalline Fe_7C_3 sample was synthesized at 7 GPa and 1473 K for 7 hours using a multi-anvil apparatus at University of Michigan. The starting material was a mixture of fine iron and graphite powders, with 10 wt.% graphite. The purpose of adding extra graphite relative to stoichiometric composition was to avoid synthesizing a mixture of Fe_3C and Fe_7C_3. 8 mm truncation edge length (TEL) high-pressure assembly was used, which consisted of a cast MgO octahedron (Aremco 584OS) with 14 mm long finned gaskets, MgO capsule and spacers and a cylindrical Re heater. Temperature was monitored by a W5%Re-W26%Re thermocouple, which was inserted into the octahedron through the center of a fin and the junction of the thermocouple directly contacted with the middle of the Re heater. The run product was characterized by electron microprobe and XRD measurement.

High pressures were generated using a symmetry-type DAC with 300 μm culet diamonds. A rhenium gasket, initially 250 μm thick, was preindented to about 27 GPa and the thickness thinned to about 43 μm. A hole of 150 μm was drilled in the center by an electric discharge machine (EDM) at University of Michigan. An Aggregation of polycrystalline Fe_7C_3 of approximately 30×20×7 μm^3 was loaded into the center of the sample chamber (Fig. 3.1). A flake of α-Fe with similar size was also placed apart from the sample. Two ruby balls with about 8 μm diameter and a flake of Au of 15×15×5 μm^3 were also put in the sample chamber as pressure standards (Fei et al., 2007; Mao et al., 1986). In addition, few Au powders with submicron sizes were put on Fe_7C_3 and α-Fe samples so the derived pressures were the same as the samples experienced. Neon was loaded into the sample chamber as hydrostatic pressure medium by the COMPRES/GSECARS gas-loading system at the Advanced Photon Source (APS), Argonne National Laboratory (Rivers et al., 2008).

High pressure angle-dispersive XRD measurements were performed at beamline 16-BM-D of APS. The wavelength of incident monochromatic X-ray was 0.4246 Å, and the full width at half maximum (FWHM) of the incident beam was about 5 μm × 15 μm. Diffracted X-rays were recorded by a MAR345 image plate. The sample-to-detector distance, the tilt angle and rotation angle of the image plate relative to the incident X-ray beam were calibrated by 1 bar diffraction of cerium dioxide (CeO_2). The X-ray diffraction images of Fe_7C_3, Fe and Au flakes were collected at each pressure point with exposure time of 30~60 seconds. Pressure interval was about 0.5 GPa for pressures below 10 GPa and became ~2-4 GPa above 10 GPa (Table 3.1 and 3.2). Ruby signal was also collected using the on-line ruby system in beamline 16-BM-D.

The 2-D XRD images were integrated to 1-D spectra using software Fit2D (Hammersley et al., 1996) and peak fitting was performed using software FullProf. The P-V curve was fitted to a third-order Birch-Murnaghan equation of state (EOS) by software EosFit7c (Angel et al., 2014).

3.4 Results

Our Fe_7C_3 sample adopted a hexagonal structure ($P6_3mc$) with the unit-cell parameters a = 6.902±(0.002) Å and c = 4.511±(0.003) Å at 1 bar, and this structure was stable over the pressure range investigated here. Table 3.1 listed the lattice parameters of h-Fe_7C_3 and corresponding pressures derived from pressure standard Au at the same place. The representative XRD image and integrated spectra were shown in Fig. 3.2 and Fig. 3.3, respectively. The lattice parameters were determined by diffraction peaks of (1 2 0), (0 1 2), (1 2 1), (3 0 0), (1 1 2), (3 0 1), (2 0 2) and (2 2 0).

The diffraction patterns of our *h*-Fe_7C_3 sample were consistent with those shown in Herbstein and Snyman. (1976) and Nakajima et al. (2011). No diffraction peaks from other iron carbides, such as Fe_5C_2 were observed (Herbstein and Snyman., 1976). Two unidentified peaks were observed with d-spacings of 2.280 Å and 2.217 Å at 1 bar, respectively. The peak at 2.217 Å gradually disappeared with pressures (Fig. 3.3) and probably was (2 0 0) peak from FeO (Fig. 3.3), which may form during the synthesis process of *h*-Fe_7C_3 in multi-anvil apparatus. The peak at 2.280 Å persisted to the highest pressures of this study (Fig. 3.3) and was also observed in Herbstein and Snyman. (1976) and Nakajima et al. (2011). The shifts of this peak with pressures had similar magnitude as peaks from Fe_7C_3 (Fig. 3.3), implying that it was unlikely from some impurity. One possible explanation is that it originates from (2 0 1) planes in *o*-Fe_7C_3 with *Pnma* space group. All the other peaks shown in Fig. 3.3 can also been fitted by *Pnma* space group. However, more than 10 diffraction peaks from *o*-Fe_7C_3 are not observed over the range of 2Θ shown in Fig. 3.3. As a result, it is more appropriate to fit the spectra by a hexagonal structure instead of an orthorhombic structure. Moreover, the derived hexagonal lattice parameters are not affected by the presence of these two peaks because they have relative low intensities and do not overlap with other peaks.

The XRD spectra of iron were also collected at each pressure step and the lattice parameters were listed in Table 3.2. The α-Fe to ε-Fe phase transition happens at 14~16.5 GPa at 300 K (Inset in. 3.4 (a)), which is consistent with previous DAC study (Dewaele et al., 2006); shock wave study (Bancroft et al., 1956) and other spectroscopic studies (e.g. Mathon et al., 2004; Wang and Ingalls, 1998).

The pressures of Au and Ne scales were determined by their equations of state (Fei et al., 2007). The ruby luminescent pressure was calculated from Mao et al. (1986). The pressures derived from Au scale at different locations within the sample chamber were different: at the center, the pressure of Au was higher than those near the edges by less than 1 GPa below 10 GPa; above 10 GPa, the central pressure was smaller and the difference became larger at higher pressures: at 68 GPa, the difference is 6 GPa (Fig. 3.5). The diffraction signal from solid Ne first appeared at 6.7 GPa and the pressure of Ne scale was first smaller then larger than that of the central Au and the difference was within 2.4 GPa. The ruby pressure was similar as those of Au scale at the edges and the difference was no more than 1.6 GPa below 45 GPa, above where ruby signal was too weak to be useful.

3.5 Discussion

3.5.1 Equations of State and Magnetic Transitions

The compression curve of h-Fe_7C_3 at 300 K is shown in Fig. 3.4. In the normalized pressure ($F=P/3f_E(1+2f_E)^{5/2}$) - Eulerian strain ($f_E=[(V/V_0)^{-2/3}-1]/2$) plot, three distinguishable regions with different slopes are present (Fig. 3.5(b)): at 0 ~ 8.9 GPa, the slope was about zero, partially due to large uncertainties of F_E at low f_E (Angel, 2001); between 8.9 ~ 21.2 GPa, the slope became negative; between 23.5 ~ 67.9 GPa, the slope became positive. For a linear relation in the F_E - f_E plot, its slope equals to $3/2K_0(K_0'-4)$ (Angel, 2001), where K_0 is isothermal bulk modulus at 1 bar and 300 K, K_0' is its pressure derivative. As a result, a 2nd-order equation of state is needed for the first segment; 3rd-order equations of state should be used for the other two segments.

This three-segments pattern also appears in the *a*/*c* - pressure plot (Inset in Fig. 3.6): below 5.6 GPa, the a/c ratios are the same within error bars; between 6.2-18.5 GPa, the slope becomes positive; above 21.2 GPa, shallower slope is present. In comparison, the a/c ratios of α-Fe only change within error bars (Table 3.3) up to 14.1 GPa, above where α-Fe to ε-Fe phase transition happens. The abnormal behaviors between 5.6 ~ 8.9 GPa in Fe_7C_3 is discovered for the first time, due to scarce data coverage below 10 GPa in previous studies (Chen et al., 2012; Nakajima et al., 2011). The second kink around 18.5 ~ 21.2 GPa was also observed in Nakajima et al. (2011).

Based on the distinguishable behaviors of these three pressure segments, the compression curve of h-Fe_7C_3 is fitted by three distinct Birch-Murnaghan equations of state (BM-EoS):

$$P = \frac{3}{2}K_{0T}\left[\left(\frac{V_0}{V}\right)^{7/3} - \left(\frac{V_0}{V}\right)^{5/3}\right] \times \left\{1 + \frac{3}{4}(K_0{}' - 4)\left[\left(\frac{V_0}{V}\right)^{2/3} - 1\right]\right\}$$

The derived elastic parameters are shown in Table 3.3. An elastic softening happens across the first discontinuity (5.6 ~ 8.9 GPa) with K_0 decreases from 236 ± 2 GPa to 180 ± 27 GPa and K_0' drops from 4 (fixed) to 3.5 ± 1.9 (Fig. 3.7 and Table 3.3). At the same pressure range, Chen et al. (2012) found *h*-Fe_7C_3 lost fast oscillations in synchrotron Mössbauer spectra, which has been interpreted as a loss of magnetic ordering. In comparison of *h*-Fe_7C_3, the compression curve of α-Fe is smooth up to 14 GPa (Fig. 3.4), which rules out the possibility that the abnormal behaviors of *h*-Fe_7C_3 are due to some experimental artificiality. Instead, the softening of *h*-Fe_7C_3 associated with magnetic collapse is likely because the ferromagnetic (fm) ground state is destabilized with pressures, and transfer to paramagnetic (pm) state above 8.9 GPa. Such pressure-induced softening, indicating by decrease in bulk modulus, has been reported in Fe-Ni Invar alloys by both experimental and theoretical studies (Dubrovinsky et al., 2001; van

Schilfgaarde et al., 1999). The Invar-like behaviors in *h*-Fe_7C_3 indicates its Curie temperature drops to 300 K at 5.6 ~ 8.9 GPa. Considering the curie temperature (*Tc*) of *h*-Fe_7C_3 is 523 K at 1 bar, Tc drops with pressure by 40 ~ 25 K/GPa. These values are once to twice higher than 12.6 K/GPa reported in Nakajima et al. (2011), implying smaller stability field of fm phase in the pressure-temperature plot.

The second discontinuity around 18.5 ~ 21.2 GPa in the compression curve of *h*-Fe_7C_3 is manifested by the changes of slopes in both F_E - f_E plot and *a*/*c* - pressure plot (Fig. 3.4 and Fig. 3.6). This discontinuity stiffens *h*-Fe_7C_3 with K_0 increases from 180 ± 27 GPa to 202 ± 12 GPa and K_0' increases from 3.5 ± 1.9 to 4.7 ± 0.3 (Table 3.3). This is also observed in Nakajima et al. (2011): Despite they interpreted this softening as a fm-pm transition, the elastic parameters of pm phase in Nakajima et al. (2011) is consistent with those of fm phase reported here within errors (Table 3.3). Since the fm-pm transition is observed at 5.6 ~ 8.9 GPa (Fig. 3.6), the second discontinuity at 18.5 ~ 21.2 GPa is most likely to be a pm to nonmagnetic (nm) phase transition, where *h*-Fe_7C_3 undergoes a high-spin to low-spin transition. Because Nakajima et al. (2011) only had two data points below 8.9 GPa, the fm-pm transition at 5.6 ~ 8.9 GPa was missed. K_0 and K_0' of the magnetic phase above 18~23.5 GPa are different between our study and Nakajima et al. (2011), which can be explained by the pressure heterogeneity in the sample chamber of DAC and different pressure standards used: Using the separate Au flake as our pressure scale, the discrepancy of compression curves from our study and Nakajima et al. (2011) is significantly reduced (Fig. 3.8). Moreover, Nakajima et al. (2011) used MgO as pressure scale for their DAC and multi-anvil experiments, which would generate 0 ~ 3 GPa difference with Au scale at the same conditions (Dorfman et al., 2012).

For the pm to nm phase transition, Chen et al. (2012) reported it happened at 53 GPa, which is more than twice of the values reported here (Table 3.3). Instead of stiffening, Chen et al. (2012) found this magnetic transition softened *h*-Fe_7C_3 (Table 3.3). On the contrary, theoretical calculations found a magnetic transition from magnetically ordered state to non-magnetical state at ~67 GPa, accompanied with augment of K_0 and K_0' (Mookherjee et al., 2011).

Such significant discrepancies in magnetic transition pressures and their effects on elastic properties were also found in another iron carbide Fe_3C: A synchrotron Mössbauer spectroscopy study reported a fm to pm transition happened at 4.3~6.5 GPa (Gao et al., 2008), which is consistent with 8~10 GPa reported by a x-ray magnetic circular dicroism study (Duman et al., 2005) and conventional Mössbaue spectroscopic study coupled with single-crystal XRD measurements (Prescher et al., 2012). The pm to nm transition in Fe_3C is more controversial: Prescher et al. (2012) reported this transition happened at ~ 22 GPa without significantly affect its elastic parameters. Their results are consistent with 25 GPa reported in a x-ray emission spectroscopy study (Lin et al., 2004). Contrarily, XRD measurements coupled with thoeretical calculations claimed nm phase was only stable above 55 GPa (Ono and Mibe, 2010). In addition, theoretical calculations indicate magnetically ordered state to non-magnetical state transition happened at ~60 GPa, with increase of K_0 and decrease of K_0' (Vocadlo et al., 2002).

There are several possible explanations for above-mentioned discrepancies: (1) Non-hydrostatic stress in DAC sample chambers can significantly influence the pressures of magnetic transitions. An experimental study on $Fe_{64}Ni_{36}$ Invar alloy showed the pressure of magnetic transition in mechanical stressed sample is about twice of that from the normal sample (Gorria et al., 2009), which was explained as stress-induced strain increased the Fe-Fe interatomic distances, further reinforced ferromagnetic interactions. Non-hydrostatic stress in DAC sample chambers could affect the pressures of magnetic transitions by a similar way. The magnitude of non-hydrostatic stress on DAC samples is influenced by many factors, such as compressibility and distribution of pressure mediums; materials of gaskets; deformation of sample chambers; sizes of samples and grain sizes (Dorfman et al., 2012). As a result, at least part of the discrepancies among different studies is due to different experimental setups and sample preparations. (2) Another possible reason is that nonstoichiometry in Fe_7C_3 and Fe_3C generate dislocations and defects (Walker et al., 2013), which could affect their compressibilities and pressures of magnetic transitions (Gorria et al., 2009). (3) The theoretical studies on Fe_7C_3 and Fe_3C focused on the fm and nm states without considering the pm state (Mookherjee et al., 2011; Ono and Mibe, 2010; Vocadlo et al., 2002). The omission of pm state in calculations of enthalpy and elastic parameters could render the inferred pressures of magnetic transitions vulnerable.

3.5.2 Invar Behavior of Fe_7C_3 and Its Effect on Fe_7C_3 Formation

The magnetio-elastic interaction has been proposed as the origin for Invar behavior (Dubrovinsky et al., 2001; van Schilfgaarde et al., 1999). For *h*-Fe_7C_3, the Invar-like behaviors have been observed between 5.6 ~ 8.9 GPa, where the bulk modulus drops (Table 3.3) and a loss of magnetic moment was observed by synchrotron Mössbauer spectroscopy (Chen et al., 2012). As a result, our experimental results are consistent with the theoretical model by Schilfgaarde (1999) for the origin of the Invar behaviors.

Fe-C phase diagrams have shown Fe_7C_3 is not stable below 5 GPa, where Fe_3C is the only stable iron carbide phase (Chabot et al., 2008; Fei and Brosh, 2014; Nakajima et al., 2009; Tsuzuki et al., 1984). Fe_7C_3 forms from a subsolidus reaction: Fe_3C+diamond/graphite = Fe_7C_3 above 5 GPa (Tsuzuki et al., 1984) and is observed above 7 GPa by several other studies (Fei and Brosh, 2014; Chen et al., 2012; Lord et al., 2009; Nakajima et al., 2009; Nakajima et al., 2011).

Based on our compression curve of Fe_7C_3 (Fig. 3.4), the net volume change of the above reaction decreases across 5.6 ~ 8.9 GPa, where the magneto-elastic interaction softens Fe_7C_3. As a result, the Gibbs energy of the reaction decreases at this pressure range and facilitate the appearance of Fe_7C_3 in the Fe-C phase diagrams.

3.6 Implications

Previous density measurements of *h*-Fe_7C_3 have found it can be a dominant phase in the Earth's inner core because the density of a mixture of *h*-Fe_7C_3 and hexagonal close-packed (HCP) iron at the relevant *P-T* conditions can match those of the inner core (Chen et al., 2012; Nakajima et al., 2011). Moreover, recent sound velocity measurements on *h*-Fe_7C_3 showed its sound velocity could match the anomalously low shear velocity observed in the inner core (Chen et al., 2014), which further supports an Fe_7C_3-dominant inner core model.

In order to investigate which magnetic phase of Fe_7C_3 is stable under the core's *P-T* conditions, we explore its phase relation at conditions where experimental data are not available yet. The melting temperatures of Fe_7C_3 were measured up to 52 GPa (Lord et al., 2009). Fitting their data by a Simon equation (Simon and Glatzel, 1929), we extrapolate the melting temperatures of Fe_7C_3 to the core's pressures (Fig. 3.9).

The paramagnetic (high-spin state) to nonmagnetic (low-spin state) transition happens between 21.2 ~ 23.5 GPa at 300 K (Fig. 3.5). The slope of this high-spin to low-spin transition is $dT/dP=\Delta\beta/\Delta\alpha$, where $\Delta\beta$ and $\Delta\alpha$ are compressibility and thermal expansion differences between low-spin and high-spin phases. Because this spin transition stiffens Fe_7C_3, $\Delta\beta$ is negative at 300 K. Nakajima et al. (2011) measured thermal EoS of *h*-Fe_7C_3 up to 1973 K and 30 GPa, however, due to limited pressure coverage, the boundary between high-spin and low-spin states cannot be resolved. In contrast, the *P*-*T* boundaries of spin transitions in silicates and oxides are better constrained: Synchrotron XRD measurements using laser-heated DAC have shown at high temperatures, the transition pressures are higher than those at 300 K and the values of dT/dP are 20 ~ 43 K/GPa (Liu et al., 2014; Mao et al., 2012). Using this range of dT/dP and the extrapolated melting temperatures, the phase diagram of Fe_7C_3 is constructed to illustrate the possible stable magnetic phases under the core's *P*-*T* conditions: as shown in Fig. 3.9, the stability *P*-*T* ranges of pm Fe_7C_3 expand as the value of dT/dP decreases: for dT/dP=43 K/GPa, low-spin state is the only stable phase of Fe_7C_3; if dT/dP is only 20 K/GPa, the spin transition of Fe_7C_3 would happen at the core's *P*-*T* conditions, and both spin states may be stable to be a component of the inner core. These two spin states have different elastic parameters (Table 3.3); sound velocities (Chen et al., 2014). In addition, they may differ in melting temperatures, rheological, thermal and electrical transport properties. Consequently, if the spin transition of Fe_7C_3 happens in the core's *P*-*T* conditions, the above mentioned properties would affect the evolution of the core and help us to understand the current state of the core, such as the origin of the innermost inner core (Ishii and Dziewonski, 2002); the anomalously low shear wave velocities of the inner core (Dziewonski and Anderson, 1981); the anisotropy of the inner core (Masters and Gilbert, 1981; Poupinet et al., 1983).

Table 3.1. Volume and unit-cell parameters of Fe_7C_3 at 300 K.

*P*au (GPa)	*V* (Å^3)	*a* (Å)	*c* (Å)
0.0	186.1(1)	6.902(2)	4.511(3)
2.2(1)	184.6(1)	6.884(2)	4.498(2)
2.4(1)	184.3(1)	6.882(2)	4.494(3)
3.0(1)	183.7(1)	6.874(2)	4.489(2)
3.5(1)	183.4(1)	6.871(2)	4.486(3)
4.1(1)	183.0(1)	6.866(2)	4.482(3)
4.5(1)	182.8(1)	6.863(2)	4.480(3)
5.0(1)	182.5(1)	6.860(2)	4.479(3)
5.5(1)	182.1(1)	6.855(2)	4.475(2)
5.6(1)	182.0(1)	6.854(2)	4.474(3)
6.2(1)	181.5(1)	6.848(2)	4.468(3)
6.3(1)	181.1(1)	6.844(2)	4.465(3)
6.9(1)	180.7(1)	6.839(2)	4.461(3)
7.6(1)	180.4(1)	6.836(2)	4.459(2)
8.2(1)	179.9(1)	6.830(2)	4.454(3)
8.5(1)	179.4(1)	6.823(2)	4.448(3)
8.9(1)	179.0(1)	6.819(2)	4.445(2)
9.6(1)	178.5(1)	6.813(2)	4.441(3)
9.9(1)	178.0(1)	6.808(2)	4.435(3)
10.7(1)	177.3(1)	6.801(2)	4.427(3)
11.6(1)	176.6(1)	6.791(2)	4.421(2)
12.8(1)	175.6(1)	6.780(2)	4.411(2)
14.9(1)	174.4(1)	6.765(2)	4.400(2)
16.6(1)	173.0(1)	6.749(2)	4.387(2)
18.5(1)	171.5(1)	6.729(2)	4.372(2)
21.2(1)	169.6(1)	6.706(2)	4.355(3)
23.5(1)	168.3(1)	6.689(2)	4.344(2)
26.6(1)	166.6(1)	6.668(2)	4.328(2)
29.9(2)	165.4(1)	6.652(2)	4.315(2)
33.2(2)	163.5(1)	6.627(2)	4.298(3)
36.5(2)	161.9(1)	6.605(2)	4.286(2)
38.7(2)	161.0(1)	6.595(2)	4.274(2)
41.2(2)	160.0(1)	6.582(2)	4.265(3)
44.5(2)	158.6(1)	6.564(2)	4.251(3)
47.0(2)	157.5(1)	6.550(2)	4.240(2)
48.9(2)	156.9(1)	6.541(2)	4.234(2)
51.3(2)	155.9(1)	6.529(2)	4.224(3)
53.1(2)	155.2(1)	6.519(2)	4.217(3)
55.6(2)	154.4(1)	6.509(2)	4.209(3)
57.8(2)	153.7(1)	6.499(2)	4.201(3)
60.2(2)	152.9(1)	6.487(2)	4.195(2)
61.9(2)	152.2(1)	6.480(2)	4.187(3)
63.8(2)	151.7(1)	6.472(2)	4.181(3)
65.8(2)	151.1(1)	6.464(2)	4.174(3)
67.9(3)	150.4(1)	6.454(2)	4.167(3)

Table 3.2. Volume and unit-cell parameters of Fe at 300 K.

bcc Fe			hcp Fe			
Pau (GPa)	V (Å^3)	a (Å)	Pau (GPa)	V (Å^3)	a (Å)	c (Å)
0	23.567(3)	2.8670(2)	17.0(1)	20.71(2)	2.457(1)	3.962(5)
1.5(1)	23.329(4)	2.8574(3)	19.3(1)	20.52(1)	2.4504(7)	3.945(3)
1.9(1)	23.291(4)	2.8558(3)	22.1(1)	20.23(2)	2.443(1)	3.913(4)
2.2(1)	23.198(4)	2.8520(3)	24.7(1)	20.06(2)	2.436(1)	3.904(4)
2.9(1)	23.147(4)	2.8499(3)	27.6(1)	19.87(2)	2.428(1)	3.892(4)
3.5(1)	23.084(4)	2.8473(3)	30.6(2)	19.68(2)	2.420(1)	3.880(3)
3.7(1)	23.048(4)	2.8458(3)	34.7(2)	19.44(2)	2.410(1)	3.863(3)
4.0(1)	22.997(4)	2.8437(3)	37.5(2)	19.26(1)	2.4028(7)	3.851(2)
4.4(1)	22.946(4)	2.8416(3)	40.4(2)	19.12(2)	2.397(1)	3.842(3)
4.6(1)	22.923(4)	2.8407(3)	42.9(2)	19.00(1)	2.3919(7)	3.834(2)
5.1(1)	22.855(4)	2.8379(3)	46.8(2)	18.82(2)	2.3847(9)	3.821(3)
5.4(1)	22.800(4)	2.8356(3)	50.0(2)	18.68(2)	2.3789(9)	3.811(3)
6.2(1)	22.733(6)	2.8328(4)	51.7(2)	18.59(1)	2.3754(9)	3.805(3)
6.4(1)	22.691(6)	2.8311(4)	54.8(2)	18.48(1)	2.3706(9)	3.797(3)
7.2(1)	22.621(5)	2.8282(4)	55.8(2)	18.37(1)	2.3660(8)	3.790(3)
7.8(1)	22.549(5)	2.8252(4)	58.1(2)	18.27(1)	2.3615(6)	3.783(2)
8.2(1)	22.492(5)	2.8228(4)	60.4(2)	18.17(1)	2.3573(8)	3.776(3)
8.9(1)	22.426(5)	2.8200(4)	63.6(2)	18.07(1)	2.3522(6)	3.771(2)
9.3(1)	22.364(5)	2.8174(4)	65.2(2)	17.99(1)	2.3488(9)	3.765(3)
10.3(1)	22.267(5)	2.8133(4)	67.5(2)	17.91(1)	2.3455(8)	3.759(3)
11.1(1)	22.167(5)	2.8091(4)	69.0(2)	17.84(1)	2.3426(8)	3.754(3)
12.4(1)	22.035(5)	2.8035(4)	73.6(3)	17.76(1)	2.3392(8)	3.748(2)
14.1(2)	21.870(5)	2.7965(4)				

Table 3.3. Equation of state parameters of Fe_7C_3. fm: ferromagnetic phase; pm: paramagnetic phase; nm: nonmagnetic phase. Nakajima11: Nakajima et al., 2011; Chen12: Chen et al., 2012.

This study	P (GPa)	V_0 ($\AA^3$)	K_0 (GPa)	K_0'
fm	0~5.6	186.1 (1)	236 (2)	4 (fixed)
pm	8.9~21.2	187.3 (9)	180 (27)	3.5 (1.9)
nm	23.5~67.9	184.9 (7)	202 (12)	4.7 (3)
Nakajima11	P (GPa)	V_0 ($\AA^3$)	K_0 (GPa)	K_0'
fm	0~18	186.4 (1)	201 (2)	4 (fixed)
pm	18~71.5	184.2 (3)	253 (7)	3.6 (2)
Chen12	P (GPa)	V_0 ($\AA^3$)	K_0 (GPa)	K_0'
pm	7~53	184.7 (2)	201 (12)	8.0 (14)
nm	53~167	182.9 (4)	307 (6)	3.2 (1)

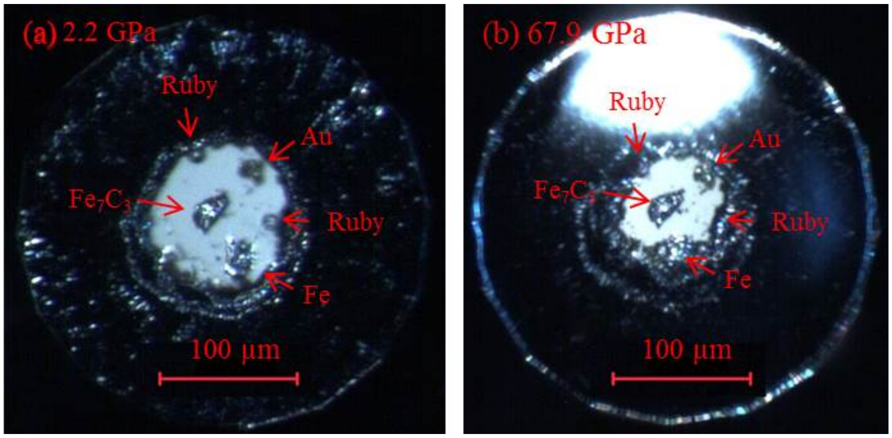

Figure 3.1. The configuration of the diamond anvil cell experiment: (a) is at 2.2 GPa, (b) is at 67.9 GPa. The center flake is Fe_7C_3, the upper right flake is Au, the bottom flake is Fe. Two ruby balls are at the top and right corners.

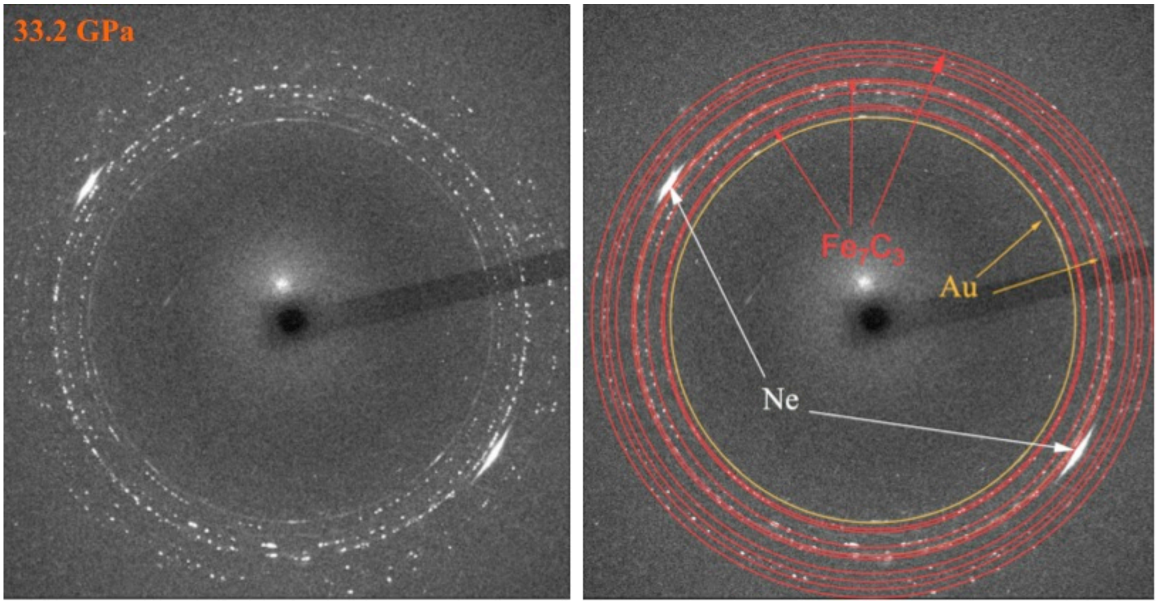

Figure 3.2. Representative X-ray diffraction image of Fe_7C_3 at 33.2 GPa. The diffraction spots from Fe_7C_3, Au are marked by red and brown rings, respectively. Ne has two separate diffraction spots.

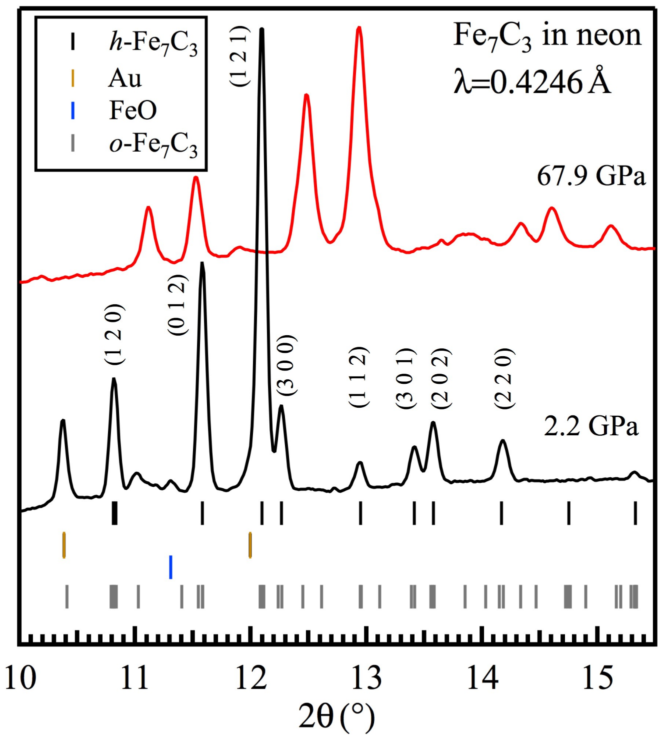

Figure 3.3. Representative X-ray diffraction patterns of Fe_7C_3 at 2.2 GPa and 67.9 GPa, respectively. Black Miller indices are from Fe_7C_3, and yellow Miller indices are from gold, which is used as the internal pressure calibrant. One unknown peak was marked by blue stars. The peak marked by green cross may be from (Mg,Fe)O. Neon peaks were masked because they overlap with peaks from Fe_7C_3.

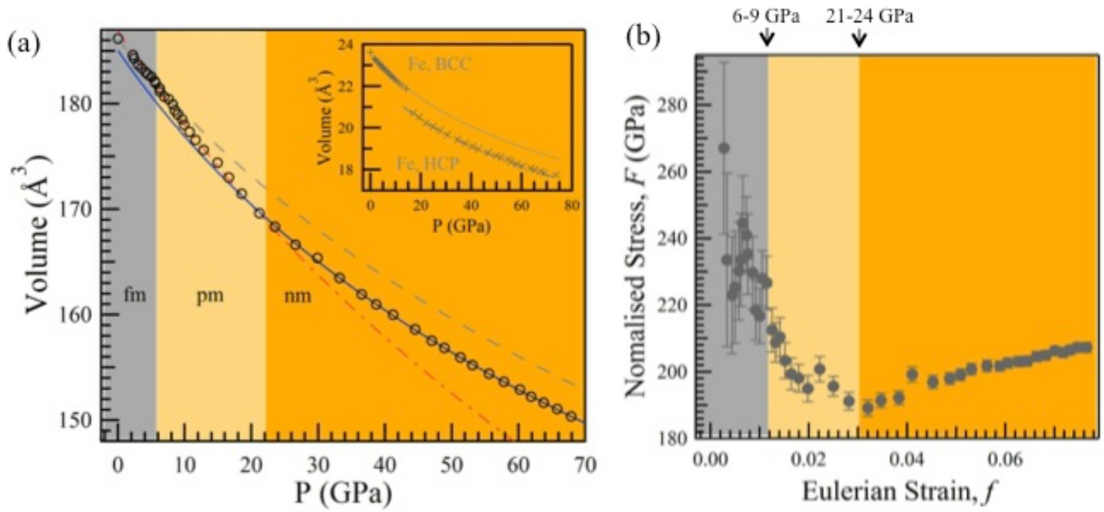

Figure 3.4. a) Unit-cell volume of Fe_7C_3 up to 68 GPa at 300 K is shown as open black circles. The dashed gray, dash-dotted red and solid black curves are Birch-Murnaghan equations of state fits to the data of fm-Fe_7C_3 (1bar ~ 5.6 GPa), pm-Fe_7C_3 (8.9 GPa ~ 21.2 GPa) and fm-Fe_7C_3 (23.5bar ~ 67.9 GPa). The inset shows unit-cell volume of Fe in the same diamond anvil cell for comparison (gray crosses). The gray curves are calculated compression curves using lattice parameters from *Robie et al*., (1987), *Guinan* and *Beshers*, (1968) for BCC phase, and *Dewaele et al*., (2006) for HCP phase. (b) The relation between finite Eulerian strain *F* and normalized stress *f*. The two discontinuities in the slopes of the *F-f* plot are at 6~9 GPa and 21~24 GPa, corresponding to fm-pm and pm-nm transitions.

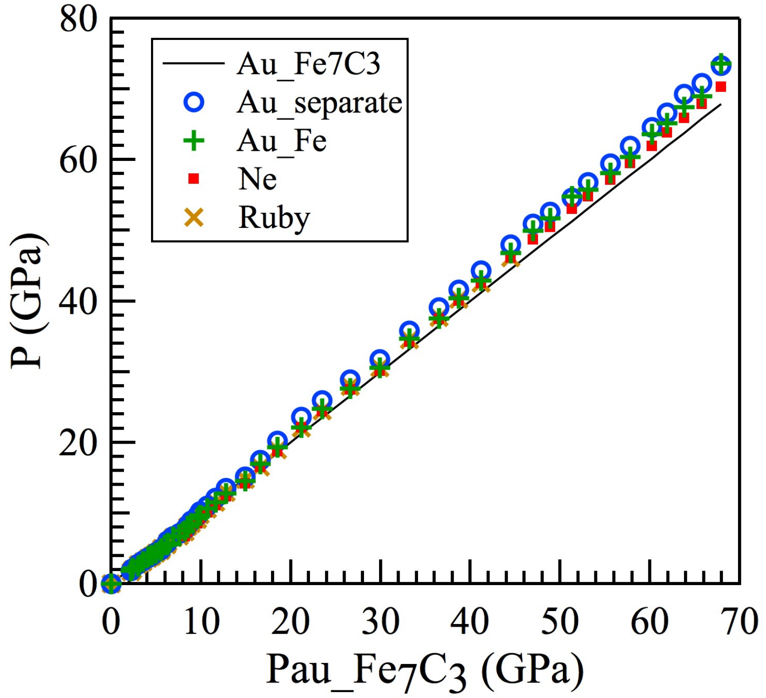

Figure 3.5. Pressures derived from Au at different locations within the DAC sample chamber and those from Ne and ruby.

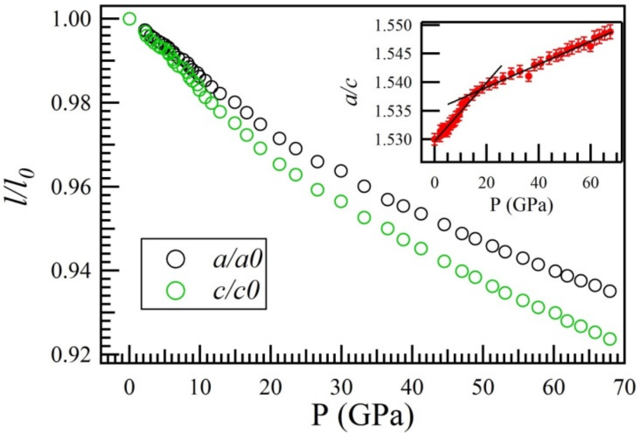

Figure 3.6. Lattice parameters *a* and *c* of Fe_7C_3 up to 68 GPa at 300 K. The inset is the axial ratio *a/c* vs. Pressure. A change of the slope is at 21~24 GPa, corresponding to pm-nm transtion.

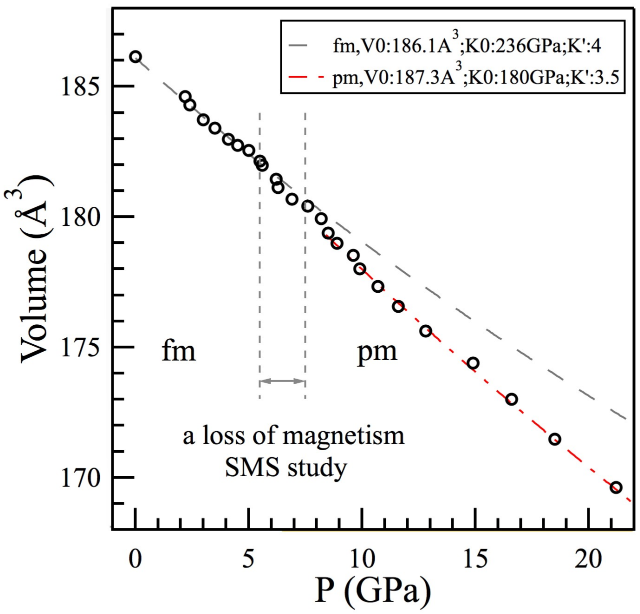

Figure 3.7. Unit-cell volume of Fe_7C_3 up to 21 GPa at 300 K is shown as open black circles. The dashed gray, dash-dotted red are Birch-Murnaghan equations of state fits to the data of fm-Fe_7C_3 (1bar ~ 5.6 GPa), pm-Fe_7C_3 (8.9bar ~ 21.2 GPa). fm-pm transition happens at 5.6 ~ 8.9 GPa, which is consistent with a loss of magnetism observed by synchrontron mössbauer spectrometer (Chen *et al*., (2012)).

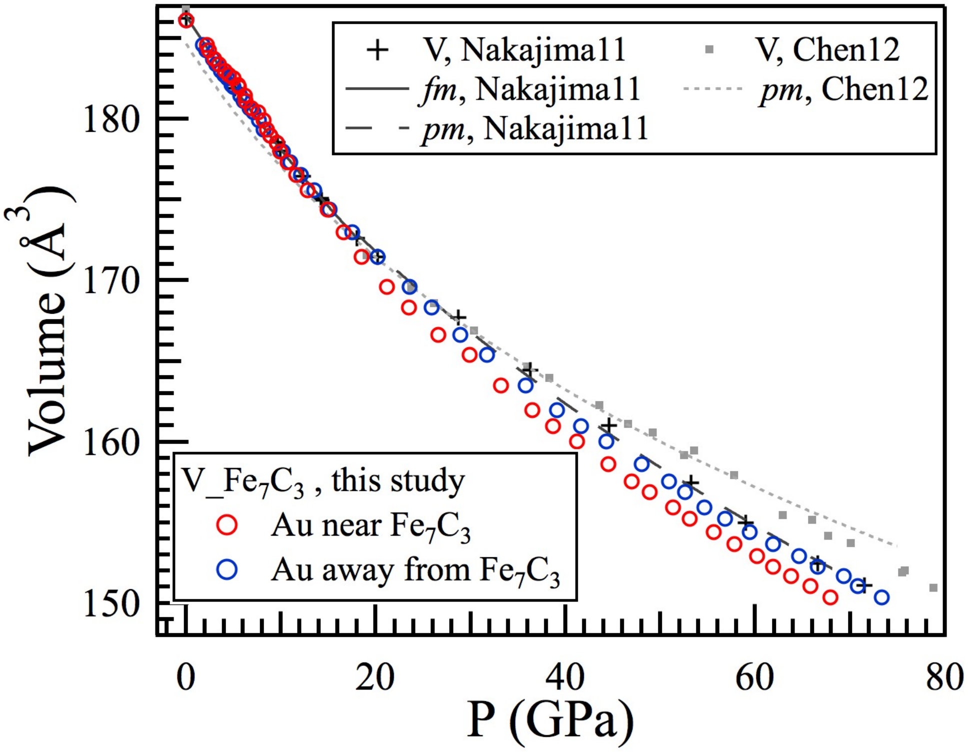

Figure 3.8. The comparison of the compression curve of *h*-Fe_7C_3 from different studies. Data sources: Nakajima11 is Nakajima et al. (2011); Chen12 is Chen et al. (2012).

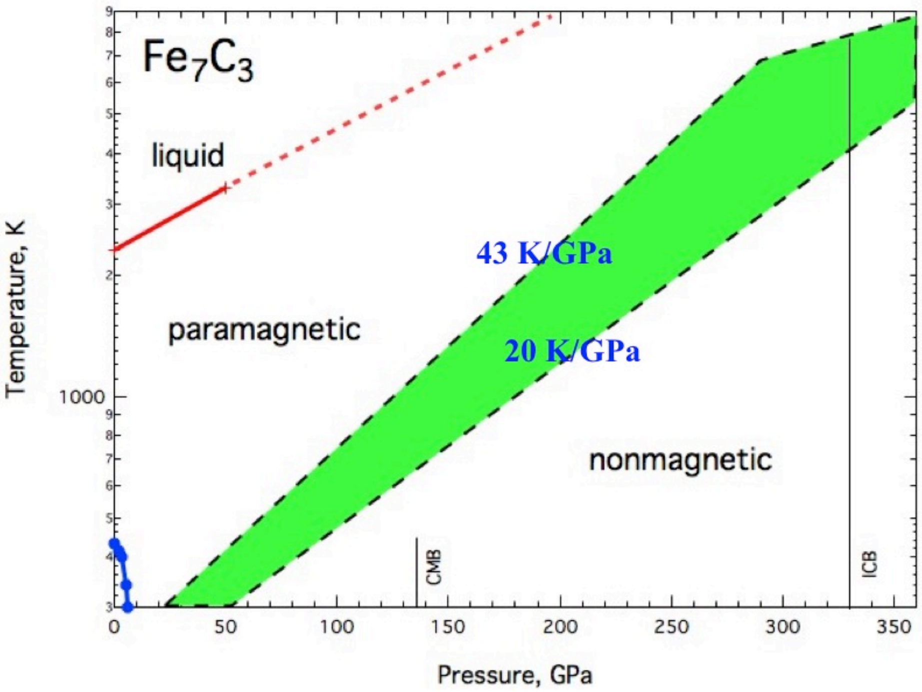

Figure 3.9. The magnetic phase diagram of Fe_7C_3 up to the core's *P-T* conditions. The red curve is a linear extrapolation of melting temperature from Lord et al., (2009); the range of the slope of spin transition boundary is constrained by those of (Mg,Fe)CO3 (Liu et al., 2014) and (Mg,Fe)O (Mao et al., 2011). Different slopes of high-spin to low-spin phase boundaries make either paramagnetic or nonmagnetic phase is stable under the core's *P-T* conditions.

3.7 References

Abrikosov, I.A., Kissavos, A.E., Liot, F., Alling, B., Simak, S.I., Peil, O., Ruban, A.V., 2007. Competition between magnetic structures in the Fe rich fcc FeNi alloys. Phys Rev B 76.

Angel, R. J. (2001), Equation of state, in High-Pressure, High-Temperature Crystal Chemistry, Rev. Mineral. Geochem., vol. 41, edited by R. M. Hazen and R. T. Downs, pp. 41, 35–60, CRC Press, Boca Raton, Fla.

Angel, R.J., Gonzalez-Platas, J., Alvaro, M., 2014. EosFit7c and a Fortran module (library) for equation of state calculations. Z Kristallogr 229, 405-419.

Bancroft, D., Peterson, E.L., Minshall, S., 1956. Polymorphism of Iron at High Pressure. J Appl Phys 27, 291-298.

Chabot, N.L., Campbell, A.J., McDonough, W.F., Draper, D.S., Agee, C.B., Humayun, M., Watson, H.C., Cottrell, E., and Saslow, S.A. (2008) The Fe-C system at 5 GPa and implications for Earth's core. Geochimica Et Cosmochimica Acta, 72(16), 4146-4158.

Chen, B., Gao, L.L., Lavina, B., Dera, P., Alp, E.E., Zhao, J.Y., Li, J., 2012. Magneto-elastic coupling in compressed Fe7C3 supports carbon in Earth's inner core. Geophys Res Lett 39.

Chen, B., Li, Z., Zhang D., Liu, J., Hu, M., Zhao, J., Bi, W., Alp, E.E., Xiao, Y., Chow, P., Li, J., 2014. Hidden carbon in Earth’s inner core revealed by shear softening in dense Fe_7C_3. Proc. Natl. Acad. Sci. USA

Dewaele, A., Loubeyre, P., Occelli, F., Mezouar, M., Dorogokupets, P.I., Torrent, M., 2006. Quasihydrostatic equation of state of iron above 2 Mbar. Phys Rev Lett 97.

Dorfman, S.M., Prakapenka, V.B., Meng, Y., Duffy, T.S., 2012. Intercomparison of pressure standards (Au, Pt, Mo, MgO, NaCl and Ne) to 2.5 Mbar (vol 117, B08210, 2012). J Geophys Res-Sol Ea 117.

Dubrovinsky, L., Dubrovinskaia, N., Abrikosov, I.A., Vennstrom, M., Westman, F., Carlson, S., van Schilfgaarde, M., Johansson, B., 2001. Pressure-induced invar effect in Fe-Ni alloys. Phys Rev Lett 86, 4851-4854.

Duman, E., Acet, M., Wassermann, E.F., Itie, J.P., Baudelet, F., Mathon, O., Pascarelli, S., 2005. Magnetic instabilities in Fe3C cementite particles observed with FeK-edge X-ray circular dichroism under pressure. Phys Rev Lett 94.

Dziewonski, A.M., Anderson, D.L., 1981. Preliminary Reference Earth Model. Phys Earth Planet In 25, 297-356.

Eckstrom, H.C., Adcock, W.A., 1950. A New Iron Carbide in Hydrocarbon Synthesis Catalysts. J Am Chem Soc 72, 1042-1043.

Fang, C.M., van Huis, M.A., Zandbergen, H.W., 2009. Structural, electronic, and magnetic properties of iron carbide Fe7C3 phases from first-principles theory. Phys Rev B 80.

Fruchart, R., and Rouault, A. (1969) Twin Crystals of Orthorhombic Isomorphous Cr7C3, Mn7C3, Fe7C3 Carbides. Annales De Chimie France, 4(3), 143-145.

Fei, Y.W., Brosh, E., 2014. Experimental study and thermodynamic calculations of phase relations in the Fe-C system at high pressures. Earth Planet Sc Lett 408, 155-162.

Fei, Y.W., Ricolleau, A., Frank, M., Mibe, K., Shen, G.Y., Prakapenka, V., 2007. Toward an internally consistent pressure scale. P Natl Acad Sci USA 104, 9182-9186.

Gao, L.L., Chen, B., Wang, J.Y., Alp, E.E., Zhao, J.Y., Lerche, M., Sturhahn, W., Scott, H.P., Huang, F., Ding, Y., Sinogeikin, S.V., Lundstrom, C.C., Bass, J.D., Li, J., 2008. Pressure-induced magnetic transition and sound velocities of Fe(3)C: Implications for carbon in the Earth's inner core. Geophys Res Lett 35.

Gorria, P., Martinez-Blanco, D., Perez, M.J., Blanco, J.A., Hernando, A., Laguna-Marco, M.A., Haskel, D., Souza-Neto, N., Smith, R.I., Marshall, W.G., Garbarino, G., Mezouar, M., Fernandez-Martinez, A., Chaboy, J., Barquin, L.F., Castrillon, J.A.R., Moldovan, M., Alonso, J.I.G., Zhang, J.H., Llobet, A., Jiang, J.S., 2009. Stress-induced large Curie temperature enhancement in Fe64Ni36 Invar alloy. Phys Rev B 80.

Hammersley, A.P., Svensson, S.O., Hanfland, M., Fitch, A.N., Hausermann, D., 1996. Two-dimensional detector software: From real detector to idealised image or two-theta scan. High Pressure Res 14, 235-248.

Herbstein, F.H., Snyman, J.A., 1964. Identification of Eckstrom-Adcock Iron Carbide as Fe7c3. Inorg Chem 3, 894-&.

Ishii, M., Dziewonski, A.M., 2002. The innermost inner core of the earth: Evidence for a change in anisotropic behavior at the radius of about 300 km. P Natl Acad Sci USA 99, 14026-14030.

Kerridge, J.F. (1985) Carbon, Hydrogen and Nitrogen in Carbonaceous Chondrites - Abundances and Isotopic Compositions in Bulk Samples. Geochimica Et Cosmochimica Acta, 49(8), 1707-1714.

Kowalski, M., 1985. Polytypic Structures of (Cr,Fe)7c3 Carbides. J Appl Crystallogr 18, 430-435.

Lin, J.F., Struzhkin, V.V., Mao, H.K., Hemley, R.J., Chow, P., Hu, M.Y., Li, J., 2004. Magnetic transition in compressed Fe3C from x-ray emission spectroscopy. Phys Rev B 70.

Liu, J., Lin, J.F., Mao, Z., Prakapenka, V.B., 2014. Thermal equation of state and spin transition of magnesiosiderite at high pressure and temperature. Am Mineral 99, 84-93.

Lord, O.T., Walter, M.J., Dasgupta, R., Walker, D., Clark, S.M., 2009. Melting in the Fe-C system to 70 GPa. Earth Planet Sc Lett 284, 157-167.

Mao, H.K., Xu, J., Bell, P.M., 1986. Calibration of the Ruby Pressure Gauge to 800-Kbar under Quasi-Hydrostatic Conditions. J Geophys Res-Solid 91, 4673-4676.

Mao, Z., Lin, J.F., Liu, J., Prakapenka, V.B., 2012. Thermal equation of state of lower-mantle ferropericlase across the spin crossover (vol 39, L02399, 2012). Geophys Res Lett 39.

Mason, B., Data of Geochemistry, 6th ed,. Ch. B1, Meteorites, 132 pp., U.S. Geol. Surv. Prof. Pap. 440-B-1, 1979.

Masters, G., Gilbert, F., 1981. Structure of the Inner Core Inferred from Observations of Its Spheroidal Shear Modes. Geophys Res Lett 8, 569-571.

Mathon, O., Baudelet, F., Itie, J.P., Polian, A., d'Astuto, M., Chervin, J.C., Pascarelli, S., 2004. Dynamics of the magnetic and structural alpha-epsilon phase transition in iron. Phys Rev Lett 93.

Mookherjee, M., Nakajima, Y., Steinle-Neumann, G., Glazyrin, K., Wu, X.A., Dubrovinsky, L., McCammon, C., Chumakov, A., 2011. High-pressure behavior of iron carbide (Fe7C3) at inner core conditions. J Geophys Res-Sol Ea 116.

Nakajima, Y., Takahashi, E., Sata, N., Nishihara, Y., Hirose, K., Funakoshi, K., Ohishi, Y., 2011. Thermoelastic property and high-pressure stability of Fe7C3: Implication for iron-carbide in the Earth's core. Am Mineral 96, 1158-1165.

Ono, S., Mibe, K., 2010. Magnetic transition of iron carbide at high pressures. Phys Earth Planet In 180, 1-6.

Poupinet, G., Pillet, R., Souriau, A., 1983. Possible Heterogeneity of the Earths Core Deduced from Pkikp Travel-Times. Nature 305, 204-206.

Prescher, C., Dubrovinsky, L., McCammon, C., Glazyrin, K., Nakajima, Y., Kantor, A., Merlini, M., Hanfland, M., 2012. Structurally hidden magnetic transitions in Fe3C at high pressures. Phys Rev B 85.

Rivers, M., Prakapenka, V.B., Kubo, A., Pullins, C., Holl, C.M., Jacobsen, S.D., 2008. The COMPRES/GSECARS gas-loading system for diamond anvil cells at the Advanced Photon Source. High Pressure Res 28, 273-292.

Senczyk, D., 1993. Some Polytypes of Fe7c3 Carbides. Phase Transit 43, 153-156.

Simon, F., Glatzel, G., 1929. Remarks on fusion pressure curve. Z Anorg Allg Chem 178, 309-316.

Tsuzuki, A., Sago, S., Hirano, S.I., Naka, S., 1984. High-Temperature and Pressure Preparation and Properties of Iron Carbides Fe7c3 and Fe3c. J Mater Sci 19, 2513-2518.

van Schilfgaarde, M., Abrikosov, I.A., Johansson, B., 1999. Origin of the Invar effect in iron-nickel alloys. Nature 400, 46-49.

Vocadlo, L., Brodholt, J., Dobson, D.P., Knight, K.S., Marshall, W.G., Price, G.D., Wood, I.G., 2002. The effect of ferromagnetism on the equation of state of Fe3C studied by first-principles calculations. Earth Planet Sc Lett 203, 567-575.

Walker, D., Dasgupta, R., Li, J., Buono, A., 2013. Nonstoichiometry and growth of some Fe carbides. Contrib Mineral Petr 166, 935-957.

Wang, F.M., Ingalls, R., 1998. Iron bcc-hcp transition: Local structure from x-ray-absorption fine structure. Phys Rev B 57, 5647-5654.

Weiss, R.J., 1963. Origin of Invar Effect. P Phys Soc Lond 82, 281-&.

Wood, B.J., 1993. Carbon in the Core. Earth Planet Sc Lett 117, 593-607.

Xie, J.Y., Chen, N.X., Shen, J., Teng, L.D., Seetharaman, S., 2005. Atomistic study on the structure and thermodynamic properties of Cr7C3, Mn7C3, Fe7C3. Acta Mater 53, 2727-2732.

Chapter IV. Eutectic Melting of Fe-C System at the Core-mantle Boundary

4.1 Abstract

Ultra-low-velocity-zones (ULVZs) are anomalous regions above the core-mantle boundary (CMB) with reduced shear wave velocity (*Vs*) and compressional wave velocity (*Vp*) and they are important for understanding the thermochemical evolution of the deep mantle. Existing hypotheses for the origin of the ULVZ often require very a very hot core, which may not be consistent with independent constraints for sustaining the geodynamo. Recent studies predicted that when the subducted slab entered the lower mantle, a mixture of about 1 wt.% iron and a small amount of carbon existed in the grain boundaries. To evaluate the fate of such mixture, I conducted melting experiments of the Fe-C system up to the lowermost mantle pressures, using the laser-heated diamond anvil cells and synchrotron x-ray diffraction techniques. Our results show that the melting curve of the Fe-C system intersects with mantle geotherm at 3068 kelvin and 128 GPa, implying that the onset of melting of iron-carbon mixture occurs within the D" layer and that about 1 wt.% Fe-C melt associated with subducted slabs would be present at depths of 20 ~ 120 km above CMB. If such mixture melts at the lowermost mantle, it would completely wet grain boundaries and lower *Vs* more than *Vp*. Therefore, such metallic melt from subducted slabs provides a plausible explanation for the non-ubiquitous occurrence of ULVZ.

4.2 Introduction

The D” layer, extending about 250~350 km above the core-mantle boundary (CMB), is characterized by complex patterns of shear wave velocities, such as 1.5 ~ 3% velocity discontinuities as well as lateral shear-wave anisotropy (Garnero and McNamara, 2008). These anomalies are associated with a solid-state phase transition from perovskite to post-perovskite (pPv) (Murakami et al., 2004). Within the D” layer, there are some regions, denominated as Ultra-Low Velocity Zones (ULVZs), with shear wave velocity (Vs) drop by up to ~ 30% and compressional wave velocity (Vp) drop by up to ~10% : The heights of ULVZs are about 5 ~ 40 km and the lateral extent ranges from 100 ~ 900 km (Cottaar and Romanowicz, 2012; Luo et al., 2001; Rondenay and Fischer, 2003; Rost et al., 2010; Rost et al., 2006; Thorne and Garnero, 2004; To et al., 2011). The origin and physical state of ULVZs are important for our understanding of the dynamic Earth and may provide new insight into the thermochemical evolution of the deep mantle. Different hypotheses have been proposed for ULVZs, including partial melting (Lay et al., 2004; Williams and Garnero, 1996); iron-rich materials due to core-mantle interaction (Mao et al., 2006; Wicks et al., 2010); ultra-dense remnants of descending slabs (Dobson and Brodholt, 2005).

The partial melting mechanism for ULVZs has several advantages: If melt exists in the grain boundaries, it can lower Vs more than Vp (Stocker and Gordon, 1975; Takei, 2002), which could be compatible with seismic observations (Cottaar and Romanowicz, 2012; Luo et al., 2001; Rondenay and Fischer, 2003; Rost et al., 2010; Rost et al., 2006; Thorne and Garnero, 2004; To et al., 2011); moreover, ~0.1 wt.% melt is enough to significantly lower seismic velocities, as long as a complete wetting of this melt occurs (Karato, 2014). Recent high pressure melting studies have shown that the solidus temperatures of peridotitic or chondritic mantle are about 4150 K ~ 4180 K at CMB pressure (Andrault et al., 2011; Fiquet et al., 2010). For a core of pure iron, temperature at CMB is about 4050 K (Anzellini et al., 2013). The presence of lighter elements in the core, such as hydrogen, carbon, silicon, sulfur, would lower this temperature by several hundreds (Li and Fei, 2014). As a result, the basal layer of the mantle is hardly molten unless the core is extremely hot or there is some chemical heterogeneity at CMB region.

Subducted oceanic lithosphere can convey localized chemical heterogeneity down to CMB (Ritsema et al., 2004): mid-oceanic ridge basalt (MORB) at the pressure-temperature condition generates excess silica and other minor phases, such as ferrite, hollandaise or an aluminous phase (Andrault et al., 2014). Moreover, the solidus temperature of MORB at CMB is about 350 K lower than those of peridotitic or chondritic mantle (Andrault et al., 2014). When subducted slabs across the 660 km discontinuity, Fe^{2+} in ringwoodite disproportionates to Fe and Fe^{3+} (Frost et al., 2004). Fe^{3+} from this reaction enters bridgmanite while about 1 wt.% Fe distributes in the grain boundaries (Frost et al., 2004). On the other hand, about 20-300 ppm carbon in subducted oceanic lithosphere is likely to be reduced to immobile diamond or iron carbides in the lower mantle (Dasgupta and Hirschmann, 2010; Frost and McCammon, 2008; Rohrbach and Schmidt, 2011). In this case, iron and diamond coexist in the subduction region beneath 660 km discontinuity, which is consistent with the presence of iron and iron carbide inclusions in lower mantle diamonds (Kaminsky and Wirth, 2011). In order to exam whether such Fe-C mixture would melt in the lower mantle, especially if it can explain the features of ULVZ, we conducted high pressure melting experiment on Fe-C system.

4.3 Experimental Methods

The starting material was a mixture of pure iron and Fe_3C with a approximate ratio of 1:1. Fe_3C was synthesized in a piston-cylinder apparatus at Lamont-Doherty Earth Observatory, Columbia University. High pressures were generated using symmetry-type diamond anvil cells (DACs) with pairs of 300 μm culet diamonds or 250/350 μm beveled diamonds. Rhenium gaskets, initially 250 μm thick, were preindented to about 27 GPa and the thickness thinned to about 35 μm. A hole of 150~180 μm was drilled in the center by an electric discharge machine (EDM) at University of Michigan. The mixture of starting materials was pre-pressed in a DAC to form ~7 μm thick flakes with a diameter of 70~130 μm. The sample was loaded into sample chamber, sandwiched by two ~10 μm thick KCl pellets, which served as thermal insulation layers, pressure transmitting media and pressure standard (Dewaele et al., 2012). Ruby balls with ~ 5 diameter were loaded into the sample chambers as secondary pressure standard. To remove any moisture, the samples were first evacuated for 30 minutes, then the sample chambers were close in vacuum by using the COMPRES/GSECARS gas-loading system at the Advanced Photon Source (APS), Argonne National Laboratory (Rivers et al., 2008).

High pressure-temperature angle-dispersive XRD measurements were performed at beamline 16-ID-B of APS. The wavelength of incident monochromatic X-ray was 0.4066 Å, and the incident beam was focused to about 4×7 μm^2. Diffracted X-rays were recorded by a MAR165 CCD detector or a two-dimensional pixel array x-ray detector (Pilatus). The sample-to-detector distance, the tilt angle and rotation angle of the detectors relative to the incident X-ray beam were calibrated by 1 bar diffraction of cerium dioxide (CeO_2).

Double-sided YLF laser-heating system was employed and ~ 30×34 μm^2 temperature 'flat top' was created by pi-shaping optics. Temperatures were measured by an imaging spectrograph from both sides of DACs independently. Temperature reading was from ~ 5×5 μm^2 region, which is compatible with the size of X-ray beam and much smaller than the size of lasers. X-ray beam, laser-heated spots and temperature reading spots were aligned by X-ray induced fluorescence from ruby balls or KCl pressure medium.

For each experiment, the sample was first compressed to the target pressure and each high temperature experiment started with a fresh region of samples. Pressures were determined by the thermal equation of state of KCl (Dewaele et al., 2012). Two different heating paths were adopted: For experiments using the MAR165 CCD detector, the temperatures gradually increased by increasing the laser powers in both sides. After target temperatures were reached, the temperatures were either quenched or gradually decreased to ambient temperature; for experiments using the Pilatus detector, samples were only exposed to lasers for 1 second for each input power of lasers, and then the lasers were blocked by a high-speed shutter and samples were quenched. XRD images and temperature readings were simultaneously collected before, during and after each heating cycle. This heating setup significantly reduced the time for samples and diamonds to expose to high temperatures. It also eliminated potential reactions between diamonds and samples. The eutectic melting temperatures measured by these two setups are consistent with each other.

4.4 Results and Discussions

The sample behavior under high pressure-temperature conditions was monitored by in situ X-ray diffraction (XRD) measurements: With increasing temperature, diffraction rings from hexagonal close packed (HCP) ε-Fe and Fe_3C became shaper; then the diffraction rings lost their continuity and further evolved to single-crystal spots due to grain growth. ε-Fe transformed to face-centered cubic γ-Fe when the temperature-pressure conditions entered its stability field (Komabayashi et al., 2009). Near the eutectic melting temperatures, large single-crystal spots of the same d-spacing could disappear and reappear at different positions in successive XRD images (Fig. 4.1). This phenomenon was also observed in other metals and silicates before melting (Andrault et al., 2014; Anzellini et al., 2013), which is caused by fast grain rotation. The commencement of eutectic melting was detected by the first appearance of a diffuse ring (Fig. 4.1), which originated from the eutectic liquid. At higher temperatures, single-crystal spots from both Fe and Fe_3C became weaker and those from Fe_3C would eventually disappear (Fig. 4.2), indicating that Fe is the liquidus phase in our experiments. If the starting compositions of all the heating spots are comparable, the eutectic composition of Fe-C system does not change significantly over the pressure range investigated here, consistent with thermodynamic calculations (Fei and Brosh, 2014). Moreover, Fe_3C is a stable subsolidus phase up to 120 GPa, therefore eutectic melting curve and Fe_3C melting curve should intersect at higher pressures (Fei and Brosh, 2014; Lord et al., 2009).

Our study extends the pressure range of eutectic melting measurements of Fe-C system to the deepest mantle (Fig. 4.3 and table 4.1) and is consistent with previous study up to 70 GPa (Lord et al., 2009), which detected melting based on temperature plateaus with respect to input laser power. Fitting our eutectic melting temperatures (T_{Eu}) by the Simon-Glatzel equation (Simon and Glatzel, 1929), it yields $T_{Eu}=[(P/13.653+1)^{1/3.0345}]\times 1420$, where P is pressure in GPa, $T_{Eu}^{1bar}=1420$ K is the eutectic melting temperature at ambient pressure (Okamoto, 1992). This eutectic melting curve intersects with geothermal (Hernlund et al., 2005) at 128 GPa, 3069 K (Fig. 4.4), corresponding to 120 km above CMB (Dziewonski and Anderson, 1981).

When the subducted slabs entered the middle part of the D'' layer, the assembly of Fe and diamond/iron carbides in the grain boundaries would start to melt. This melting temperature is 634 ~ 778 K lower than that of MORB (Andrault et al., 2014) and 928 ~ 1082 K lower than that of chondritic or peridotitic mantles (Andrault et al., 2011; Fiquet et al., 2010) (Fig. 4.4). In the regions of subducted slabs, there would always be a small amount of melt (~ 1 wt.%) in the basal part of the lower mantle, no matter the core is hot or cold (Hernlund et al., 2005).

About 1 wt.% Fe and 20 ~ 300 ppm carbon could be generated when subducted slabs penetrated the 660 km discontinuity (Dasgupta and Hirschmann, 2010; Frost et al., 2004) (Fig. 4.5). For this range of compositions, the temperature difference between solidus and liquidus is about 250 ~ 300 K at CMB pressure (Fei and Brosh, 2014). As a result, 1 wt.% Fe-C melt is expected in the grain boundaries at depths of 20 ~ 120 km above CMB, depending on local carbon concentration in Fe-C mixture (Fig. 4.5). This melt is likely to completely wet grain boundaries because the dihedral angle of metallic liquids decreases significantly with pressure in lower mantle minerals (Shi et al., 2013) (Fig. 4.6). This scenario would lead to nonubiquitous low velocity zones with Vs drops more than Vp (Stocker and Gordon, 1975; Takei, 2002), which is a reasonable mechanism for ULVZs. The majority of such Fe-C melt may eventually enter the core by percolation, however 0.1 wt.% residual melt in the lowest mantle is not excluded (Bagdassarov et al., 2009), which is sufficient to significantly lower sound velocities in the present time.

Table 4.1. Upper bound of eutectic melting temperatures of Fe-C system at high pressures. The numbers in parethesis are standard deviations in the last digits.

Pressure (GPa)	Eutectic melting temperature (K)
26.3	2066(35)
29.9	2081(58)
39.3	2257(74)
41.5	2321(60)
53.9	2433(20)
55.8	2334(44)
67.5	2640(18)
83.6	2643(49)
110.9	2949(41)
118	3005(41)

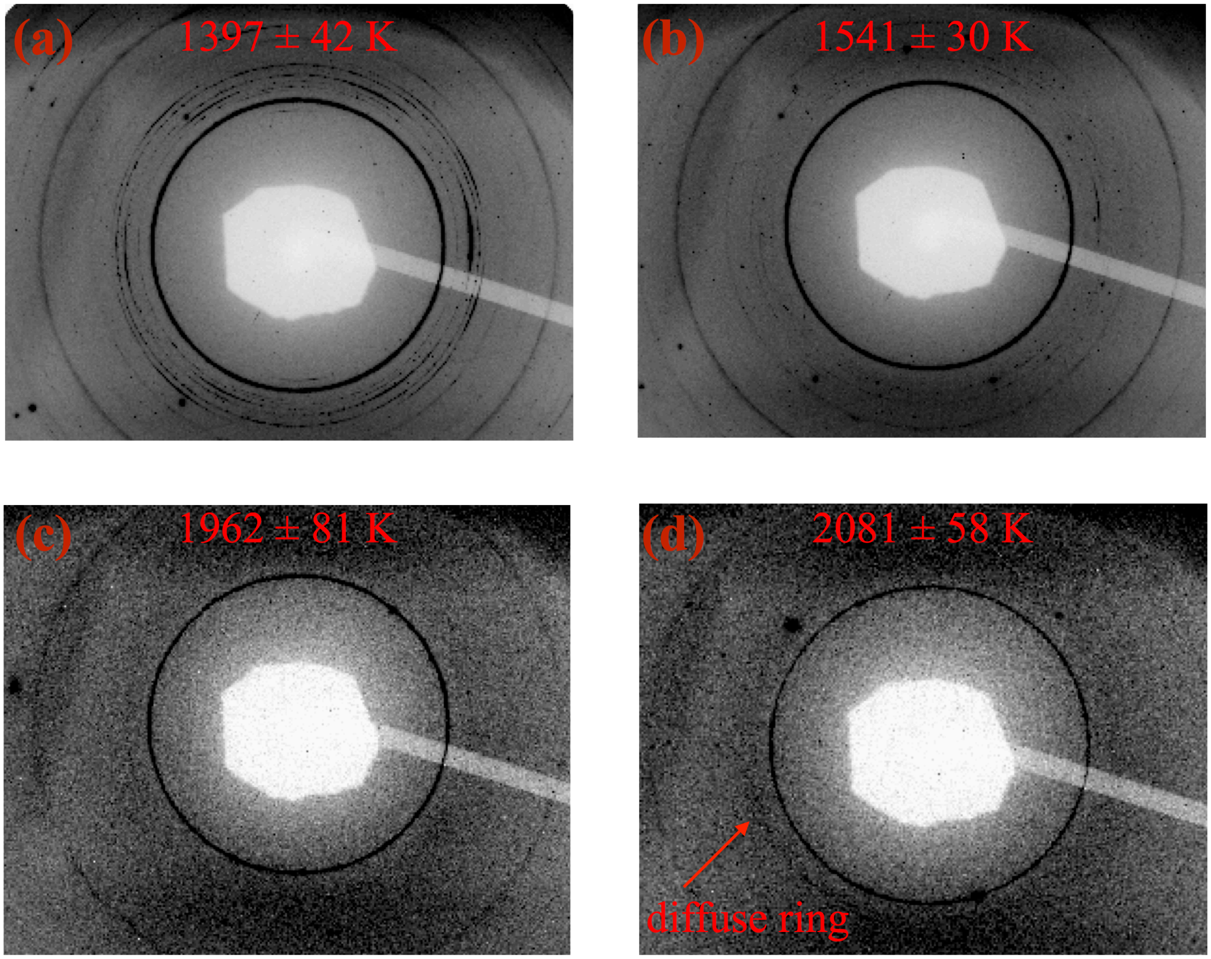

Figure 4.1. The change of X-ray diffraction images with increasing temperatures at 29.9 GPa. At 1397 ± 42 K, diffracted signals from Fe, Fe_3C and KCl were continuous rings; when temperature reached 1541 ± 30 K, diffraction rings from Fe and Fe3C changed to single-crystal spots due to grain growth. With increasing temperature to 1962 ± 81 K, most single crystal spots became very weak. At 2081 ± 58 K, a diffuse ring was first observed, which was an upper bound of eutectic temperature.

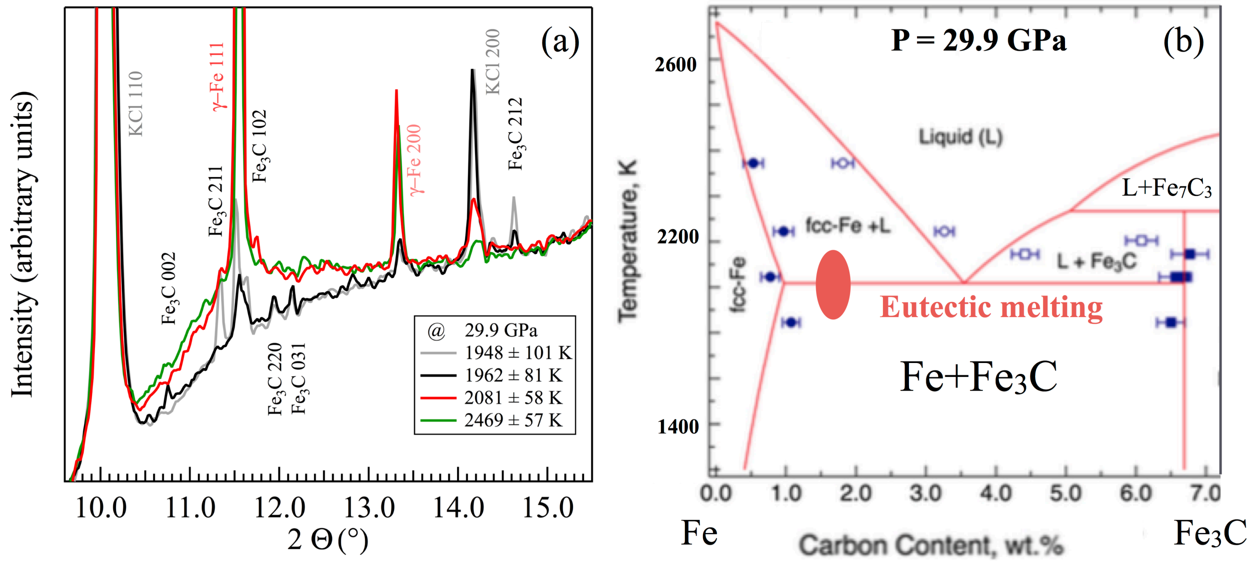

After Fei and Brosh, 2014

Figure 4.2. Integrated x-ray diffraction spectra around the eutectic temperature at 29.9 GPa. At 1962 K, all diffraction peaks are weaker compared with the spectrum at 1948 K; at 2081 K, diffusing scattering signal is first present; the xrd spectra do not change much up to 2469 K; (b) At 29.9 GPa, the eutectic temperature of Fe-C system is bracketed by the temperatures at which the solid diffracted signals are the weakest and a diffuse ring appears for the first time, which is shown as ellipse in the Fe-C phase diagram modified after Fei and Brosh (2014).

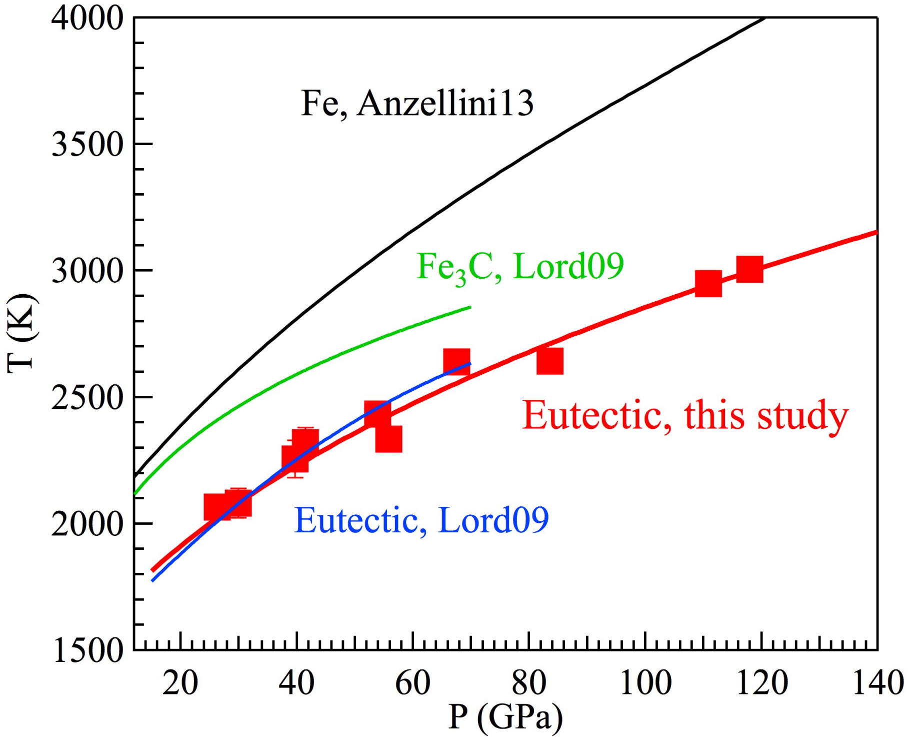

Figure 4.3. Eutectic melting points of Fe-C system (red squares) and curve fit using the Simon-Glatzel equation (red curve, eq. 1), along with melting data from literature. The blue curve is euctectic melting curve of Fe-C system from (Lord et al., 2009). Most of our data below 70 GPa fall into their eutectic melting curve, indicating our results are very consistent with (Lord et al., 2009). The melting curves of Fe_3C (Lord et al., 2009), Fe (Anzellini et al., 2013) are also shown for comparison. The eutectic melting temperatures are about 370 ~ 280 K lower than the melting temperatures of Fe_3C (green curve) between 15 ~ 70 GPa; about 450 ~ 1060 K lower than the melting temperatures of Fe (black curve) between 15 ~ 136 GPa.

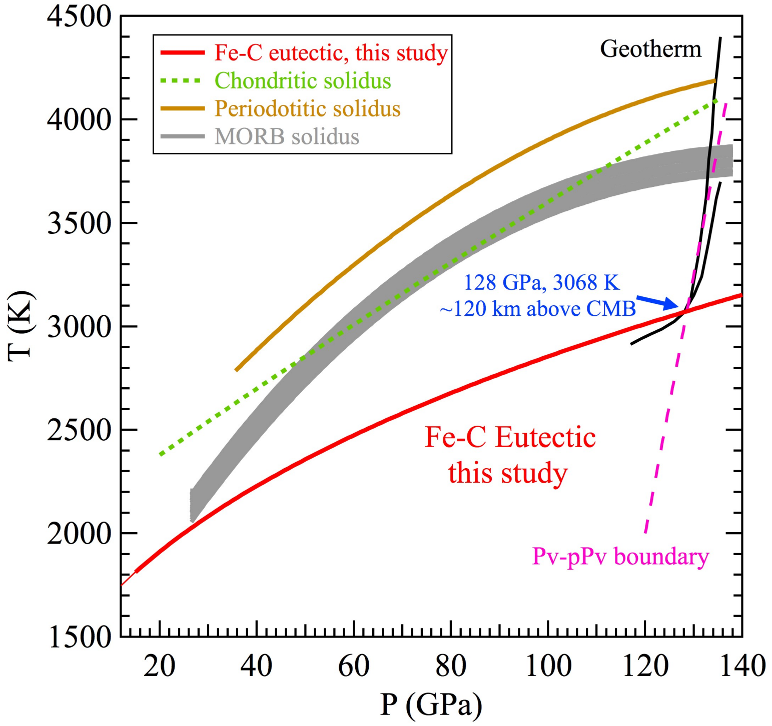

Figure 4.4. The eutectic melting curve of Fe-C system (red curve) plotted together with geotherm and the solidus curves of possible mantle materials. The geotherm (black curves) was calculated based on the double-crossing of the $MgSiO_3$ perovskite (Pv) to post-perovskite (pPv) within the D'' layer (Hernland et al., 2005) and both geotherms for a hot core (4400 K in the core side of the CMB) and a cold core (3700 K in the core side of the CMB) were shown. The Pv-pPv phase boundary for Fe- and Al-bearing magnesium silicate perovskite was also shown as the pink line (Ono and Oganov, 2005). At the CMB, the eutectic melting temperature of Fe-C system is 928 K lower than the solidus of chondritic mantle (Andrault et al., 2011), 1082 K lower than that of periodotitic mantle (Fiquet et al., 2010) and 634 ~ 778 K lower than that of MORB (Andrault et al., 2014).

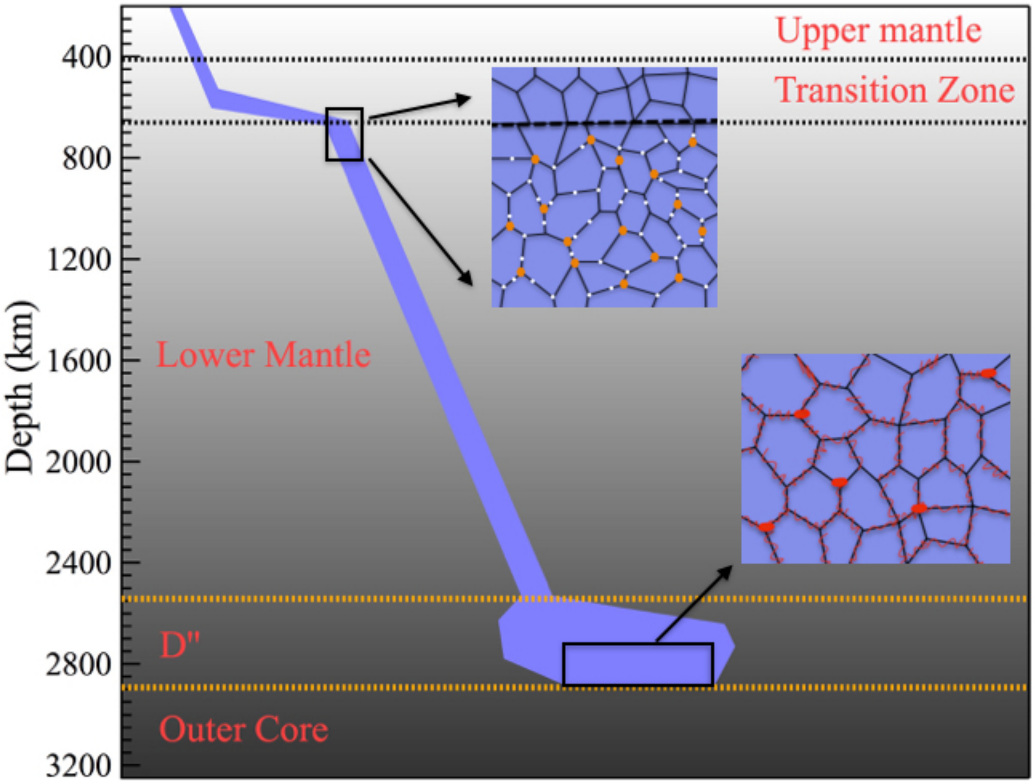

Figure 4.5. Cartoon illustrating a possible sequence of subducted oceanic lithosphere going down the CMB. The blue region stands for a subducted slab, when it penetrated the 660 km discontinuity, about 1 wt.% metallic Fe (bright dots in the upper inset) is generated by the disproportionation reaction of Fe^{2+} (Frost et al., 2004). It should distribute in grain boundaries, along with 20~200 ppm carbon (orange hexagon in the upper inset), which is expected to be diamond or iron carbide due to the reducing condition in the lower mantle (Rohrbach and Schmidt, 2011; Dasgupta and Hirschmann, 2010). This mixture of iron and diamond/iron carbide would start to melt at a depth of 120 km above CMB (red regions in the lower inset). Such melt should be able to completely wet grain boundaries (Shi et al., 2013), resulting in nonubiquitous low sound velocity zones at the basal layer of the mantle.

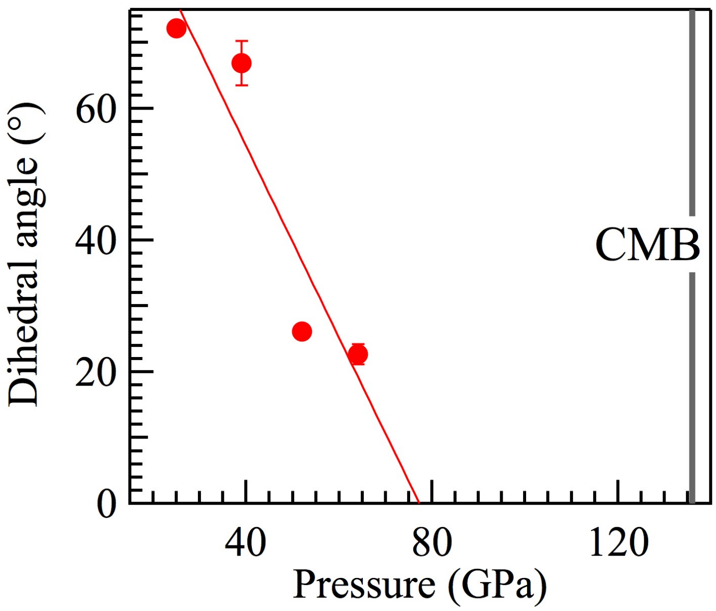

Figure 4.6. The dihedral angles in enstatite - FeNiS melt as a function of pressure from Shi et al., (2013). The dihedral angle decreases significantly at high pressure and is expected to become 0° at pressures above 77 GPa. It implies at the CMB pressure, meltallic liquids should completely wet grain boundaries.

4.4 Reference

Andrault, D., Bolfan-Casanova, N., Lo Nigro, G., Bouhifd, M.A., Garbarino, G., Mezouar, M., 2011. Solidus and liquidus profiles of chondritic mantle: Implication for melting of the Earth across its history. Earth Planet Sc Lett 304, 251-259.

Andrault, D., Pesce, G., Bouhifd, M.A., Bolfan-Casanova, N., Henot, J.M., Mezouar, M., 2014. Melting of subducted basalt at the core-mantle boundary. Science 344, 892-895.

Anzellini, S., Dewaele, A., Mezouar, M., Loubeyre, P., Morard, G., 2013. Melting of Iron at Earth's Inner Core Boundary Based on Fast X-ray Diffraction. Science 340, 464-466.

Bagdassarov, N., Solferino, G., Golabek, G.J., Schmidt, M.W., 2009. Centrifuge assisted percolation of Fe-S melts in partially molten peridotite: Time constraints for planetary core formation. Earth Planet Sc Lett 288, 84-95.

Cottaar, S., Romanowicz, B., 2012. An unsually large ULVZ at the base of the mantle near Hawaii. Earth Planet Sc Lett 355, 213-222.

Dasgupta, R., Hirschmann, M.M., 2010. The deep carbon cycle and melting in Earth's interior. Earth Planet Sc Lett 298, 1-13.

Dewaele, A., Belonoshko, A.B., Garbarino, G., Occelli, F., Bouvier, P., Hanfland, M., Mezouar, M., 2012. High-pressure high-temperature equation of state of KCl and KBr. Phys Rev B 85.

Dobson, D.P., Brodholt, J.P., 2005. Subducted banded iron formations as a source of ultralow-velocity zones at the core-mantle boundary. Nature 434, 371-374.

Dziewonski, A.M., Anderson, D.L., 1981. Preliminary Reference Earth Model. Phys Earth Planet In 25, 297-356.

Fei, Y.W., Brosh, E., 2014. Experimental study and thermodynamic calculations of phase relations in the Fe-C system at high pressure. Earth Planet Sc Lett 408, 155-162.

Fiquet, G., Auzende, A.L., Siebert, J., Corgne, A., Bureau, H., Ozawa, H., Garbarino, G., 2010. Melting of Peridotite to 140 Gigapascals. Science 329, 1516-1518.

Frost, D.J., Liebske, C., Langenhorst, F., McCammon, C.A., Tronnes, R.G., Rubie, D.C., 2004. Experimental evidence for the existence of iron-rich metal in the Earth's lower mantle. Nature 428, 409-412.

Frost, D.J., McCammon, C.A., 2008. The redox state of Earth's mantle. Annu Rev Earth Pl Sc 36, 389-420.

Garnero, E.J., McNamara, A.K., 2008. Structure and dynamics of Earth's lower mantle. Science 320, 626-628.

Hernlund, J.W., Thomas, C., Tackley, P.J., 2005. A doubling of the post-perovskite phase boundary and structure of the Earth's lowermost mantle. Nature 434, 882-886.

Kaminsky, F.V., Wirth, R., 2011. Iron Carbide Inclusions in Lower-Mantle Diamond from Juina, Brazil. Can Mineral 49, 555-572.

Karato, S., 2014. Does partial melting explain geophysical anomalies? Phys Earth Planet In 228, 300-306.

Komabayashi, T., Fei, Y., Meng, Y., Prakapenka, V., 2009. In-situ X-ray diffraction measurements of the gamma-epsilon transition boundary of iron in an internally-heated diamond anvil cell. Earth Planet Sc Lett 282, 252-257.

Lay, T., Garnero, E.J., Williams, Q., 2004. Partial melting in a thermo-chemical boundary layer at the base of the mantle. Phys Earth Planet In 146, 441-467.

Li J, Fei Y (2014) Experimental constraints on core composition. Treatise on Geochemistry, eds Holland HD, Turekian KK (Elsevier, New York), 2nd Ed, pp 527–557.

Lord, O.T., Walter, M.J., Dasgupta, R., Walker, D., Clark, S.M., 2009. Melting in the Fe-C system to 70 GPa. Earth Planet Sc Lett 284, 157-167.

Luo, S.N., Ni, S.D., Helmberger, D.V., 2001. Evidence for a sharp lateral variation of velocity at the core-mantle boundary from multipathed PKPab. Earth Planet Sc Lett 189, 155-164.

Mao, W.L., Mao, H.K., Sturhahn, W., Zhao, J.Y., Prakapenka, V.B., Meng, Y., Shu, J.F., Fei, Y.W., Hemley, R.J., 2006. Iron-rich post-perovskite and the origin of ultralow-velocity zones. Science 312, 564-565.

Murakami, M., Hirose, K., Kawamura, K., Sata, N., Ohishi, Y., 2004. Post-perovskite phase transition in MgSiO3. Science 304, 855-858.

Okamoto, H., 1992. The C–Fe (carbon–iron) system. J. Phase Equilib. 13, 543–565.

Ono, S., and Oganov, A.R. (2005) In situ observations of phase transition between perovskite and CaIrO3-type phase in MgSiO3 and pyrolitic mantle composition. Earth and Planetary Science Letters, 236(3-4), 914-932.

Ritsema, J., van Heijst, H.J., Woodhouse, J.H., 2004. Global transition zone tomography. J Geophys Res-Sol Ea 109.

Rivers, M., Prakapenka, V.B., Kubo, A., Pullins, C., Holl, C.M., Jacobsen, S.D., 2008. The COMPRES/GSECARS gas-loading system for diamond anvil cells at the Advanced Photon Source. High Pressure Res 28, 273-292.

Rohrbach, A., Schmidt, M.W., 2011. Redox freezing and melting in the Earth's deep mantle resulting from carbon-iron redox coupling. Nature 472, 209-212.

Rondenay, S., Fischer, K.M., 2003. Constraints on localized core-mantle boundary structure from multichannel, broadband SKS coda analysis. J Geophys Res-Sol Ea 108.

Rost, S., Garnero, E.J., Stefan, W., 2010. Thin and intermittent ultralow-velocity zones. J Geophys Res-Sol Ea 115.

Rost, S., Garnero, E.J., Williams, Q., 2006. Fine-scale ultralow-velocity zone structure from high-frequency seismic array data. J Geophys Res-Sol Ea 111.

Shi, C.Y., Zhang, L., Yang, W.G., Liu, Y.J., Wang, J.Y., Meng, Y., Andrews, J.C., Mao, W.L., 2013. Formation of an interconnected network of iron melt at Earth's lower mantle conditions. Nat Geosci 6, 971-975.

Simon, F., Glatzel, G., 1929. Bemerkungen zur Schmelzdruckkurve. Z. Anorgan. Allg. Chem. 178, 309–316.

Stocker, R.L., Gordon, R.B., 1975. Velocity and Internal-Friction in Partial Melts. J Geophys Res 80, 4828-4836.

Takei, Y., 2002. Effect of pore geometry on V-P/V-S: From equilibrium geometry to crack. J Geophys Res-Sol Ea 107.

Thorne, M.S., Garnero, E.J., 2004. Inferences on ultralow-velocity zone structure from a global analysis of SPdKS waves. J Geophys Res-Sol Ea 109.

To, A., Fukao, Y., Tsuboi, S., 2011. Evidence for a thick and localized ultra low shear velocity zone at the base of the mantle beneath the central Pacific. Phys Earth Planet In 184, 119-133.

Wicks, J.K., Jackson, J.M., Sturhahn, W., 2010. Very low sound velocities in iron-rich (Mg,Fe)O: Implications for the core-mantle boundary region. Geophys Res Lett 37.

Williams, Q., Garnero, E.J., 1996. Seismic evidence for partial melt at the base of Earth's mantle. Science 273, 1528-1530.

Chapter V. Chemical Convection in Lunar Core from Melting Experiments on Fe-Ni-S System

5.1 Abstract

Paleomagnetic studies on lunar rocks revealed that ancient lunar dynamo probably existed 4.2 billion years ago and lasted for more than 500 million years. Recent dynamic simulations suggested that the lunar dynamo might have stopped when the solidification regime of the lunar core changed from freezing at the bottom of the molten core to crystallizing at the top of the liquid layer. To test this hypothesis, I conducted experiments at relevant pressure conditions using the multi-anvil apparatus to determine the melting behavior of Fe-S binary and Fe-Ni-S ternary systems as simplified model compositions for the lunar core. Our results show that for the Fe-S binary system the solidification regime of the core depends strongly on its sulfur content, and it is expected to switch from the Earth-like "frozen heart" scenario to "snowing" if the initial sulfur content falls between 5 and 11 wt.%. Applying a thermal evolution model, we find that a core with the initial sulfur content of about 7 wt.% can explain the timing and duration of the ancient lunar dynamo.

5.2 Introduction

The physical and chemical properties of the lunar core have drawn broad attention: Recent seismic study reanalyzed Apollo seismic data and suggested the lunar core is partially molten, consisting of a liquid outer shell and a solid inner sphere (Weber et al., 2011); Using high quality lunar gravity data from Gravity Recovery and Interior Laboratory (GRAIL) mission, Williams et al. (2014) proposed several models of the lunar interior structure with the radius of the core ranges from 372 km to 278 km and the corresponding radius of the inner core ranges from 0 km to 277 km; Other models of lunar interior structure suggested similar core size based on different evidences, such as sound velocity measurements of candidates of lunar core (Jing et al., 2014), electromagnetic sounding from satellites (Shimizu et al., 2013). The existence of a fluid outer core is also supported by laser ranging determination of pole orientation (Williams et al., 2001) and depletions of siderophile elements in the lunar mantle (Rai and van Westrenen, 2014; Righter, 2002).

The lunar core should be mainly composed of Fe as the Earth core due to geochemical similarities between Earth and Moon (Dauphas et al., 2014 and references within). Besides Fe, there are at least two other elements are likely present in the lunar core: Recent studies on lunar volcanic glasses (Saal et al., 2008) and melt inclusions (Hauri et al., 2011) showed the lunar mantle has compatible sulfur content as the Earth mantle. Considering the cosmochemical abundance of sulfur and its affinity with iron, sulfur is a likely light element present in the lunar core. Another candidate siderophile element in the lunar core is Ni: the contents of Ni in lunar volcanic glasses are consistently lower than samples from Earth upper mantle (Drake, 1987), which can be explained by the decrease of Ni partitioning coefficient between metallic liquid and silicate liquid with pressure (Li and Agee, 1996). Estimated Ni content in lunar core ranges from 8 wt.% to 55 wt.% of the lunar core (Righter, 2002 and references within). Such a wide range is due to different bulk compositions, sizes of lunar core and Ni partitioning coefficients used in different models (Righter, 2002).

Paleomagnetic studies on lunar rocks have shown that ancient lunar dynamo probably existed 4.2 billion years ago and lasted for more than 500 million years (Garrick-Bethell et al., 2009;

Shea et al., 2012; Suavet et al., 2013; Tikoo et al., 2012). The origin and long duration of ancient lunar dynamo have been studies for decades and remain controversial. Different hypotheses have been proposed but cannot fully explain the paleomagnetic observations: Thermally driven dynamo associated with mantle overtune cannot produce long-lived and continuous paleomagnetic field (Stegman et al., 2003; Zhang et al., 2013); Basin-forming impacts could power a lunar dynamo, but mismatch with paleomagnetic observations in timing (Le Bars et al., 2011); mechanical stirring mechanism mismatches in magnetic intensity (Dwyer et al., 2011). By considering the contribution of the core crystallization from the center, a recent study showed the chemical buoyancy is sufficient to support a long-lived lunar dynamo, even to the present time (Laneuville et al., 2014). The cessation of the lunar dynamo is attributed to a change of core formation scheme from the bottom-up to the top-down, where a compositionally stratified layer is formed at the top of the core and impairs the lunar dynamo rapidly (Laneuville et al., 2014; Ruckriemen et al., 2014; Williams, 2009).

The pressure dependence of liquidi of lunar core compositions is essential for understanding the evolution of the lunar core (Williams, 2009). Interestingly, the pressures of the lunar core are about 5.1 GPa (Weber et al., 2011), which is the pressure of the δ (bcc)-γ (fcc)–liquid triple point of pure iron (Anderson and Isaak, 2000). In addition, another major liquidus phase FeS also has a phase transition from FeS II to FeS III around 6 GPa (Fei et al., 1995). The phase transitions in iron and iron sulfide may significantly influence the behaviors of Fe-S and Fe-Ni-S liquidi. In this study, we measured the liquidi of Fe-S and Fe-Ni-S systems at the pressure of the lunar inner core boundary (ICB) in order to understand the evolution of the lunar core and the ancient lunar dynamo.

5.3 Experimental Methods

Fe-S and Fe-Ni-S phase equilibrium experiments at 5.1 GPa and 1273-1873K, imaging and chemical analysis of the run products were performed at University of Michigan.

Starting materials were mixtures of pure iron, nickel and troilite powders, all of which were commercially available. The compositions of starting materials depended on the target temperatures of experiments: the sulfur content ranged from 9 wt.% to 4 wt.% for Fe-S system and from 9 wt.% to 0.5 wt.% for Fe-Ni-S system. We added about 50 wt.% Ni in Fe-Ni-S starting material, which is approximately the maximum amount of Ni estimated in the lunar core.

The partially melting experiments were performed in a 1000 US ton Walker-type multi-anvil apparatus. The force-pressure relationship was calibrated by bracketing the known bismuth (Bi) I-II, II-III and III-V transition; quartz-coesite transition and $CaGeO_3$ garnet-perovskite transition (Bose and Ganguly, 1995; Decker et al., 1972; Susaki et al., 1985) (Fig. 5.1). 17 mm precast Ceramacast 584 octahedral pressure medium was used and compressed by WC cubes with 12 mm truncated edge length to reach the target pressure. Double-chamber configuration was employed and the two chambers were placed symmetrically with respect to the center of assembly, ensuring the temperature profiles inside the two chambers were identical (Fig. 5.2). Finely grounded starting materials were packed into MgO capsules and heated using a cylindrical rhenium heater. Temperatures were monitored with a W5%Re-W26%Re thermocouple, which traversed the rhenium heater and stayed in the center of the assembly. The temperatures in the center and the sample chambers follow a linear relation (Fig. 5.3), which were measured by putting another thermocouple in sample chamber position in a test experiment. This linear relation was used to correct the difference between thermocouple readings and temperatures in sample chambers. The effect of pressure on the electro-motive force (emf) was ignored. 1 mm thick ZrO_2 thermal insulation sleeve surrounded Re heater was used for experiments with target temperature higher than 1673 K.

For each experiment, the target pressure was first reached, and then temperature was increased with a rate of 60 K /minute to 1073 K and held for 6~24 hours to presinter MgO capsules in order to prevent sample leakage. After presintering, temperature was continuously increased to the target temperature and held for at least 1 hour to reach equilibrium. Then the experiments were quenched by temperature control program and temperature dropped to below 500 K in less than 5 seconds. Recovered run products were mounted into resin and polished along the longitudinal direction of the cylindrical rhenium heater.

All the run products were carbon coated before being imaged and chemical analyzed using the Cameca SX-100 electron microprobe. Beam conditions were 15 kV, 20 nA, counting times of 30 seconds. Pure iron, nickel and pyrite were used as standards for Fe, Ni and S. All the measured areas were away from boundaries between solid and liquid phases, also away from boundaries between samples and MgO capsules. Due to the dendritic quench texture of liquid phase (Fig. 5.2), defocused 20 μm beam were used and multiple measurements covering most areas were averaged to represent the composition of liquid phase. For solid phase, using point beam and defocused 20 μm beam gave consistent compositional results.

5.4 Results

The complete summary of experimental conditions and compositions of run products were listed in Table 5.1. Optical and back-scattered electron (BSE) images of representative run products were shown in Fig. 5.2. For all the experiments, solid phases and liquid phases completely separated; solid phases consistently distributed in the cold ends, regardless of gravitational stability. Such separations were caused by thermal migration (Lesher and Walker, 1988): in the presence of small temperature gradient across sample charges, Fe and Fe-Ni components in liquid phase had higher concentration in hot end than in cold end according to the liquidi (Fig. 5.4), which drove them diffused to the cold end. Therefore in the cold end, Fe and Fe-Ni components were oversaturated and crystallized. In the meanwhile, to sustain equilibrium state, more crystalline Fe and Fe-Ni alloy dissolved in the hot end.

The compositions of liquid phases were used to construct the liquidus curves at 5.1 GPa (Fig. 5.4). In order to test whether our experimental durations were long enough to reach equilibrium, one experiment (#043012) first stayed at 1700 K for 20 minutes, and then temperature was decreased to 1478 K and stayed for 1 hour before quenching. The recovered samples had consistent compositions as those that from experiments directly reached the target temperatures, which implied 1 hour was long enough for both Fe-S and Fe-Ni-S systems to reach equilibrium state at temperatures above eutectic temperatures. The smallest temperature difference between our experiments was 50 K, and those experiments gave consistent but distinguishable results, which implied temperature uncertainty was smaller than 50 K. In experiment #071013, same Fe-Ni-S starting materials were loaded to the two chambers, and the run products gave identical compositions, proving that the two chambers experienced identical temperature profile.

For both Fe-S and Fe-Ni-S systems, solid phase was homogeneous. This implies that at 5.1 GPa, face-centered-cubic (fcc) Fe-Ni alloy form solid solution with Ni content at least up to 56.64 wt.% (Table 5.1). Considering fcc Fe-Ni alloys form complete solid solution at 1 bar (Schwartzendruber et al., 1991), pressure up to 5 GPa has insignificant effect on fcc Fe-Ni alloys in terms of forming solid solution. The dendritic quench texture of liquid phase was composed of Fe-Ni dendrites surrounding by fine-grained sulfide interstitial phases (Fig. 5.2).

5.5 Discussions

5.5.1 The Effects of Ni on the Properties of the Lunar Core

Our experimental data show the presence of Ni lowers the liquidus temperatures by 40~105 K (Fig. 5.4), which are consistent with previous studies at 18~40 GPa (Pike et al., 1999; Stewart et al., 2007; Zhang and Fei, 2008). Our liquidus data of Fe-S system are consistent with the calculated liquidus based on liquidus data at 1 bar, 3 GPa, 6 GPa and 10 GPa (Brett and Bell, 1969; Buono and Walker, 2011; Chen et al., 2008; Hansen and Anderko, 1958) or asymmetric Margules model (Buono and Walker, 2011). If sulfur content in the lunar core is compatible with that in the Earth core (Boyce et al., 2010; Boyce et al., 2010; Boyce et al., 2010), the upper limit is 13 wt.% (Li and Fei, 2014). According to our liquidus curves, the corresponding temperature at ICB is 1637 K in Fe-S system and is lowered to 1593 K by the presence Ni (Fig. 5.4). This range of temperatures at the ICB is high enough to support the existence of a partially molten layer above the core-mantle boundary (CMB) (Weber et al., 2011). On the other hand, the effect of Ni on the densities and sound velocities of both solid and liquid Fe-Ni alloys is minor (Hixson et al., 1990; Mao et al., 1990; Kantor et al., 2007), especially compared with the effect of sulfur (Badro et al., 2007; Balog et al., 2003; Chen et al., 2014; Fei et al., 1995; Jing et al., 2014; Nishida et al., 2013; Sanloup et al., 2000).

The partitioning coefficients for Ni between solid Fe and Fe-S liquid are shown in fig. 5.5 and table 5.2. Our partitioning data are consistent with those at 1 bar (Chabot et al., 2003, 2007), implying pressure has ignorable effect on Ni partitioning behavior in the Fe-S system below 5.1 GPa. On the other hand, the partitioning data at 9 GPa (Chabot et al., 2011) are smaller than those at lower pressures (Fig. 5.5), which may be due to the bcc to fcc structure transition in solid Fe around 5.2 GPa (Anderson and Isaak, 2000) and the structure transition in Fe-S liquid (Morard et al., 2007) around 5 GPa.

5.5.2 Thermodynamic Model

In order to understand the evolution of Fe-S liquidi with pressures, asymmetric Margules solution model has been used to simulate the liquidi of Fe-S system from 1 bar to 10 GPa (Brett and Bell, 1969; Buono and Walker, 2011; Chen et al., 08; Hansen and Anderko, 1958).

In Fe-S system, Fe and FeS are the end members for pressures below 14 GPa (Fei et al., 1997). The total Gibbs energy of Fe-S liquid can be expressed as follows:

$$G^{\mathrm{L}}(x) = \mu^{\mathrm{L,Fe}}(1-x) + \mu^{\mathrm{L,FeS}}x \quad (1)$$

Where G^{L} is the total Gibbs energy of the liquid phase; x is the molar fraction of FeS component; $\mu^{\mathrm{L,Fe}}$ and $\mu^{\mathrm{L,FeS}}$ are chemical potential of Fe and FeS in the liquid phase, respectively. In addition, geometric analysis in $G^{\mathrm{L}} - x$ relation gives the following equation:

$$\frac{\partial G^{\mathrm{L}}(x)}{\partial x} = \frac{G^{\mathrm{L}}(x) - \mu^{\mathrm{L,Fe}}}{x} \quad (2)$$

Asymmetric Margules solution formulation is used to describe the excess Gibbs energy in Fe-S liquid, and Eq. (1) is rewritten as:

$$G^{\mathrm{L}}(x) = \mu_0^{\mathrm{L,Fe}}(1-x) + \mu_0^{\mathrm{L,FeS}}x + x(1-x)[w_G^{\mathrm{Fe}}x + w_G^{\mathrm{FeS}}(1-x)] + RTx\ln(x) + RT(1-x)\ln(1-x) \quad (3)$$

Here $\mu_0^{\mathrm{L,Fe}}$ and $\mu_0^{\mathrm{L,FeS}}$ are the standard chemical potentials of liquid Fe and FeS at reference P-T condition. w_G^{Fe} and w_G^{FeS} are Margules interaction constants. Substituting Eq. (3) into Eq. (2), $\mu_0^{\mathrm{L,FeS}}$ is cancelled out and Eq. (2) becomes

$$\mu^{\mathrm{L,Fe}} - \mu_0^{\mathrm{L,Fe}} = (2w_G^{\mathrm{FeS}} - w_G^{\mathrm{Fe}})x^2 - 2(w_G^{\mathrm{FeS}} - w_G^{\mathrm{Fe}})x^3 + RT\ln(1\text{-}x) \quad (4)$$

For Fe-rich portion of Fe-S liquidi, the liquidus phase is almost pure iron below 25 GPa (Li et al., 2001), therefore $\mu^{\mathrm{L,Fe}}$ in Eq. (4) is equal to $\mu_0^{\mathrm{S,Fe}}$. Substituting $\mu^{\mathrm{L,Fe}}$ by $\mu_0^{\mathrm{S,Fe}}$ and incorporating the *P-T* dependence of $\mu_0^{\mathrm{L,Fe}}$ and $\mu_0^{\mathrm{S,Fe}}$, Eq. (4) becomes:

$$\mu_0^{\mathrm{S,Fe}}(1bar,T)-\mu_0^{\mathrm{L,Fe}}(1bar,T)+\int_{1bar}^{P}(V^{\mathrm{S,Fe}}(T,P)-V^{\mathrm{L,Fe}}(T,P))\mathrm{d}P=(2w_G^{\mathrm{FeS}}-w_G^{\mathrm{Fe}})x^2$$
$$-2(w_G^{\mathrm{FeS}}-w_G^{\mathrm{Fe}})x^3+RT\ln(1\text{-}x) \quad (5)$$

The reference *P-T* condition is 1 bar, 1809 K, which is the melting temperature of iron at 1 bar. $\mu_0^{\mathrm{S,Fe}}(1bar,T)$ and $\mu_0^{\mathrm{L,Fe}}(1bar,T)$ were from Barin. (1995); The pressure dependence was calculated as follows:

$$\int_{1bar}^{P}[V^{\mathrm{S,Fe}}(T,P)-V^{\mathrm{L,Fe}}(T,P)]\mathrm{d}P$$
$$=\int_{1bar}^{P}\left\{V^{\mathrm{S,Fe}}(300K,P)*exp\left[\int_{300K}^{T}\alpha^{\mathrm{S,Fe}}(T,P)dT\right]-V^{\mathrm{L,Fe}}(300K,P)*exp\left[\int_{300K}^{T}\alpha^{\mathrm{L,Fe}}(T,P)dT\right]\right\}\mathrm{d}P \quad (6)$$

$V^{\mathrm{S,Fe}}(300K,P)$ and $V^{\mathrm{L,Fe}}(300K,P)$ were calculated bya third-order Birch Murnaghan equation of state. Thermal expansion $\alpha^{\mathrm{S,Fe}}(T,P)$ and $\alpha^{\mathrm{L,Fe}}(T,P)$ were calculated using the Anderson-Grüneisen parameter: $\delta_T=\frac{\partial\ln\alpha}{\partial\ln V}$. All the thermoelastic parameters of iron used here were from (Komabayashi and Fei, 2010).

Eq. (5) was used to fit all available Fe-S liquidi up to 10 GPa (Fig. 5.6). Instead of incorporating the *P-T* dependence of W_{Fe}, W_{FeS} and using a single set of the expanded Margules parameters to fit all the available Fe-S liquidi up to 10 GPa (Buono and Walker, 2011), we fitted each liquidus individually.

The pressure dependence of W_{FeS} is linear while there is an obvious change in the pressure dependence of W_{Fe} (Fig. 5.6 and table 5.3). Such discontinuity cannot be explained by the differences of thermoelastic parameters between δ and γ phases because using either δ or γ phase as the only liquidus phase in fitting did not mitigate these discontinuities. One possible explanation is that the liquid-liquid transition in metallic liquid near the vicinity of δ (bcc)-γ (fcc)–liquid triple point infects the iron-rich part of Fe-FeS liquidi: structure transition of liquid Fe from bcc-like local order to a mixture of bcc and fcc-like local order has been observed near the triple point (Sanloup et al., 2000), accompanying with abrupt increase in electrical resistivity (Secco and Schloessin, 1989) and drop of viscosity coefficient (Terasaki et al., 2002). Another study on the structure of the Fe-S eutectic liquid has shown that the pressure dependence of eutectic temperature and the volume occupancy of the eutectic liquid described by a hard sphere model changed around 5 GPa (Morard et al., 2007), which may be also related to the liquid-liquid transition.

5.5.3 Core Evolution

The lunar core has been proposed to solidify from the CMB to the center, based on that the adiabatic slopes of liquid iron and Fe-S alloy are steeper than their liquidus slopes over the pressure range of the lunar core (Jing et al., 2014; Williams, 2009). In this case, the lunar core starts to solidify at its top and the follow-up process is that crystallized iron descent down to the center of the core (Chen et al., 2008; Hauck et al., 2006; Jing et al., 2014; Stewart et al., 2007).

Assuming sulfur is a major light element in the lunar core, using interpolated Fe-S liquidi to calculate liquidus gradients around lunar core pressures is not appropriate because Fe-S liquidi change nonlinear with respect to pressure (section "*5.5.2. Thermodynamic Model*"). Here the liquidus gradient of Fe-S system around lunar core pressures is recalculated using the Fe-S liquidus data at the pressure range of the lunar core (4.9~5.6 GPa), and is compared with the correspoding adiabatic gradient. Because the pressures of lunar core span less than 1 GPa, the liquidus and adiabatic gradients at ICB are representative.

In Fig. 5.7 (a), the pressure dependence of liquidus temperatures are shown. To calculate the liquidus slopes, three sets of pressures are chosen: the first set contains liquidus data at 5.1 and 6 GPa, which is the pressure range from luner center to ICB (Fig. 5.8). The second set consists of data at 3, 5.1 and 6 GPa, which covers the whole pressure range of the luanr core. The third set is data at 1 bar, 3 GPa and 10 GPa, which is used to calculate liquidus slopes in previous studies (Weber et al., 2011; Williams, 2009). The first set of data is fitted by linear equation while the others are fitted by quadratic equations (Fig. 5.7 (a)), and the corresponding liquidus slopes at lunar ICB are shown in fig. 5.7 (b).

The adiabatic gradients are calculated following the method described in Stacey (2005): $(\frac{dT}{dP})_{ad} = \frac{\alpha T}{\rho C_P} = \left(\frac{\alpha_0 T_0}{\rho_0 C_{P0}}\right)\left(\frac{\rho_0}{\rho}\right)^{\delta_S+1}$, where α, ρ and C_P are thermal expansion, density and heat capacity of the bulk liquid core composition at lunar core pressures while α_0, ρ_0 and α, ρ and C_P are the corresponding parameters at 1 bar; δ_S is the adiabatic Anderson-Grüneisen parameter. Using the above equation, the calculated adiabatic slope of Fe-S liquid given in Jing et al. (2014) is 38 ~ 43 K/GPa at the lunar core pressures (Fig. 5.7 (b)).

Comparing the three sets of liquidus gradients with the two sets of adiabatic gradients calculated above (Fig. 5.7 (b)), different core solidification senarios can be expected: 1) Using the larger value of thermal expansion and the adiabatic gradient derived from liquidus data at 1 bar, 3 GPa and 10 GPa, the adiabatic gradient is always higher than the liquidus gradient (Fig. 5.7 (b)). Consequently, the core would start to crystallize from the top, which is consistent with previous studies (Jing et al., 2014; Williams, 2009). On the other hand, if only the liquidi around the pressures of the lunar core are used for calculating liquidus gradents, they are larger than corresponding adiabatic gradients for sulfur content lower than 9.5 ~ 11.3 wt.%, depending on which set of pressure combinations and thermal expansion are used in the calculations (Fig. 5.7 (b)). As a result, the scheme of the lunar core crystallization can change from the bottom-up to the top-down if the sulfur content of the lunar ourter core pass the transition point due to the core crystallization.

5.5.4 Ancient Lunar Dynamo

In order to illustrate how the transition of the lunar core crystallization from the bottom-up to the top-down affects the evolution of the ancient lunar dynamo, we calculated the compositional heat flow (Q_c) in lunar liquid outer following Davies and Gubbins, (2011) and compared it with the minimal CMB heat flow (Q_{min}) required for sustaining a convective core dynamo (Stevenson et al., 1983):

$$Q_c = -\rho_{oc} C_P \frac{\alpha_c}{\alpha_T} \frac{4\pi r_0^2 \rho_{ic} c_0}{\tau_r M_{oc}} \frac{T_{ic}}{T_{oc}} \frac{dT_{oc}}{dt} V_{oc} \qquad (7)$$

$$Q_{\min} = \alpha_T T_{CMB} g_{CMB} k_c / C_P \qquad (8)$$

Where ρ_{oc} and ρ_{ic} are the mean densities of the outer and inner core; C_P is the specific heat of the core; a_c is compositional expansion coefficient, a_T is thermal expansion of the core; c_0 is outer core concentration; τ_r is difference between melting and adiabatic gradients, T_{ic}, T_{oc}, T_{CMB} are temperatures in the inner core, outer core and CMB; M_{oc} and V_{oc} are mass and volume of the outer core; k_c is thermal conductivity of the outer core.

The lunar pressure and gravity profiles (Fig. 5.8) are calculated using the following equations:

$$g(R) = \frac{4\pi G}{R^2} \int_0^R r^2 \rho(r) dr \qquad (9)$$

$$P(R) = \int_{R}^{R_{\mathrm{Moon}}} g(r)\rho(r)dr \qquad (10)$$

Where g(R), ρ(R) and P(R) are gravity, density and pressure at distance R of lunar interior from the center; G is gravitational constant and R_{Moon} is the radius of the Moon.

The temperature gradient difference τ_r should be positive so the core crystallizes from the center and exclusion of light alloying elements from ICB provides chemical buoyance force to power a dynamo. As discussed above, such process is possible for sulfur content in the liquid outer core lower than 9.5 ~ 11.3 wt.% (Fig. 5.7 (b)).

Using the core model given in Weber et al., (2011), the relation between the bulk sulfur content in the core and the sulfur content in the outer core is calculated based on mass conservation (Fig. 5.9). Along with the growth of the inner core, Q_c and Q_{min} are calculated with different bulk sulfur contents and are shown in Fig. 5.9. The cooling rate follows the computational result from Zhang et al, (2013). The temperature profile in lunar core is constructed based on the Fe-S liquidus from this study; the mass and volume of the outer core are calculated based on the core model from Weber et al, (2010). The sulfur content of the liquid outer core increases with the growth of the inner core, which is composed of pure iron.

Using different values of thermal expansion, liquidus and adiabatic gradients, the change of the scheme of the lunar core crystallization happens when the sulfur content of the lunar outer core is about 9.5 ~ 11.3 wt.% (Fig. 5.7 (b)). It means that when the bulk sulfur content equals to 5.4 ~ 11.3 wt.%, the core starts to crystallize in the center and change to the top-down scheme when the sulfur content in the liquid outer core is more than 9.5 ~ 11.3 wt.% (Fig. 5.9). The calculated Q_c and Q_{min} show that for sulfur contents lower than 5.4 wt.%, Q_c is higher than Q_{min} except at the very beginning of inner core solidification (Fig. 5.10 (a)) and the chemical buoyance force could support a lunar dynamo. Such a lunar dynamo is not expected to shut down, which is consistent with recent geodynamic calculations (Laneuville et al., 2014). For bulk sulfur contents between 9.5 ~ 11.3 wt.%, the compositional heat flux changes from position to negative when sulfur content of the outer core passes the transition point (Fig. 3.10 (b)). Across this transition, the crystallization scheme of the lunar core changes from the bottom-up to the top-down. Consequently, a sulfur-rich layer stably stays in the top part of the lunar core, reducing the thickness of convection layer. Furthermore, there is no chemical buoyance force associated with exclusion of light-alloying elements at the ICB to fuel a magnetic dynamo. As a result, the top-down crystallization of the inner core can only sustain a short-lived dynamo, probably for less than 100 Ma (Laneuville et al., 2014; Ruckriemen et al., 2014), which can explain the cessation of ancient lunar dynamo. If the initial sulfur content is more than 11.3 wt.%, the compositional heat flux is always insufficient to support a lunar dynamo.

5.6 Conclusions

We determined the liquidus curves of Fe-S system and Fe-Ni-S system at the pressure of the lunar ICB (5.1 GPa). Our results show the melting temperatures and partitioning coefficients of Ni are significantly affected by liquid and solid structure transitions in Fe-S system around 5 GPa. Compared with the adiabatic gradients, the liquidus gradients are higher for sulfur content smaller than 9.5 ~ 11.3 wt.%. Such lunar core crystallizes from the center and could power a long-lived dynamo. With the growth of the inner core, the sulfur content in the lunar outer core increases and the adiabatic gradients become smaller than the adiabatic gradients. Consequently, the lunar dynamo may shut down within 100 Ma. The time duration for such transition is determined by the cooling rate of the core, the thermal evolution of the mantle. By incorporating our liquidus data, geodynamic calculations are needed to determine the duration of such a lunar dynamo.

Table 5.1. Conditions and results of melting experiments in the systems of Fe-S and Fe-Ni-S at 5.1 GPa.

Exp. #	*T* (K)	Time (h)	Phases	Fe wt.%	Ni wt. %	S wt. %	Total wt. %
042412-1	1237	2	Fe	99.89(6)	-	0.06(2)	99.95(6)
			FeS	63.4(1)	-	36.1(1)	99.5(1)
042412-2	1237	2	Fe-Ni alloy	43.8(1)	55.7(1)	0.14(5)	99.6(1)
			Fe-Ni-S melt	32.0(3)	45.8(4)	21.9(4)	99.7(1)
082212-1	1286	3	Fe	99.70(7)	-	0.03(1)	99.73(7)
			FeS	63.19(9)	-	36.03(4)	99.2(1)
			Fe-S melt	76.1(2)	-	22.8(2)	98.9(2)
082212-2	1286	3	Fe-Ni alloy	44.0(2)	54.7(3)	0.04(1)	98.7(1)
			Fe-Ni-S melt	32.3(4)	45.0(5)	22.2(5)	99.5(1)
042912-1	1334	2	Fe	99.5(1)	-	0.05(1)	99.6(1)
			Fe-S melt	76.66(8)	-	22.43(5)	99.09(6)
042912-2	1334	2	Fe-Ni alloy	43.5(1)	56.6(2)	0.08(1)	100.18(8)
			Fe-Ni-S melt	33.0(4)	46.9(5)	20.6(7)	100.5(1)
032912-1	1430	1	Fe	100.05(6)	-	0.07(1)	100.12(6)
			Fe-S melt	78.1(3)	-	21.0(3)	99.1(1)
032912-2	1430	1	Fe-Ni alloy	43.74(9)	56.25(6)	0.09(1)	100.1(1)
			Fe-Ni-S melt	33.3(3)	48.2(5)	18.8(4)	100.3(1)
021013-1[a]	1430	1	Fe	-	-	-	-
			Fe-S melt	78.6(4)	-	20.6(3)	99.2(1)
021013-2	1430	1	Fe-Ni alloy	43.15(8)	55.25(6)	0.08(1)	98.5(1)
			Fe-Ni-S melt	33.4(3)	47.0(5)	18.8(5)	99.1(1)
043012-1	1478	1	Fe	99.90(7)	-	0.08(1)	99.98(7)
			Fe-S melt	80.3(6)	-	18.8(6)	99.1(1)
043012-2	1478	1	Fe-Ni alloy	46.2(5)	53.7(5)	0.09(1)	99.99(6)
			Fe-Ni-S melt	35.7(6)	46.8(5)	18.0(9)	100.5(1)
040412-1	1526	1	Fe	99.90(7)	-	0.13(3)	100.03(5)
			Fe-S melt	83.2(4)	-	16.1(4)	99.3(1)
040412-2	1526	1	Fe-Ni alloy	44.48(4)	55.25(4)	0.10(1)	99.83(6)
			Fe-Ni-S melt	35.8(3)	48.8(5)	15.8(6)	100.4(1)
081912-1	1580	1	Fe	99.76(6)	-	0.08(1)	99.84(6)
			Fe-S melt	84.3(5)	-	15.2(4)	99.5(1)
081912-2	1580	1	Fe-Ni alloy	45.46(6)	53.20(1)	0.10(1)	98.76(6)
			Fe-Ni-S melt	38.3(3)	48.4(3)	12.8(3)	99.5(1)
041012-1	1623	1	Fe	99.79(9)	-	0.11(1)	99.9(1)
			Fe-S melt	85.5(3)	-	13.7(3)	99.2(1)

Table 5.1. continue

Exp. #	*T* (K)	Time (h)	Phases	Fe wt.%	Ni wt. %	S wt. %	Total wt. %
041012-2	1623	1	Fe-Ni alloy	45.84(9)	54.03(8)	0.11(1)	99.98(9)
			Fe-Ni-S melt	39.2(2)	49.3(3)	11.7(4)	100.2(1)
041413-1	1719	1	Fe	99.8(1)	-	0.09(1)	99.9(1)
			Fe-S melt	89.5(3)	-	10.1(3)	99.6(1)
041413-2	1719	1	Fe-Ni alloy	51.55(9)	48.37(6)	0.06(1)	99.98(7)
			Fe-Ni-S melt	48.0(1)	46.4(2)	5.7(3)	100.1(1)
021613-1	1815	1	Fe	99.76(3)	-	0.08(1)	99.92(1)
			Fe-S melt	94.6(3)	-	5.1(3)	99.71(4)
021613-2	1815	1	Fe-Ni-S melt	53.4(2)	38.4(2)	8.2(3)	99.51(4)
071013-1	1815	1	Fe-Ni alloy	46.1(1)	53.4(1)	0.02(1)	99.52(6)
			Fe-Ni-S melt	45.08(7)	53.0(1)	0.9(1)	98.98(8)
071013-2	1815	1	Fe-Ni alloy	45.2(1)	54.03(4)	0.02(1)	99.25(9)
			Fe-Ni-S melt	44.53(6)	53.88(7)	0.58(6)	98.99(8)

The numbers in parenthesis were standard errors in the last digits.

[a] The solid phase was lost when we opened the assembly.

Table 5.2. The partition coefficient of Ni ($D_{Ni}^{solid/liquid}$) between solid and liquid iron-alloys at different temperatures and 5.1 GPa.

Temperature (K)	D_{Ni}
1237	1.22(1)
1286	1.22(2)
1334	1.21(1)
1430	1.17(1)
1430	1.18(1)
1478	1.15(2)
1526	1.13(1)
1580	1.099(7)
1623	1.096(7)
1719	1.042(5)
1815	1.008(3)
1815	1.003(1)

Table 5.3. Margules interaction constants at different pressures.

Pressure (GPa)	W_{FeS}(kJ/mol)	W_{Fe}(kJ/mol)
0	26.5(1)	9.1(2)
3	15.5(1)	-8.1(7)
5.1	6.9(7)	-17.9(5.0)
6	1.5(1.2)	-26.7(7.0)
10	-17.9(1.8)	-76.2(8.8)

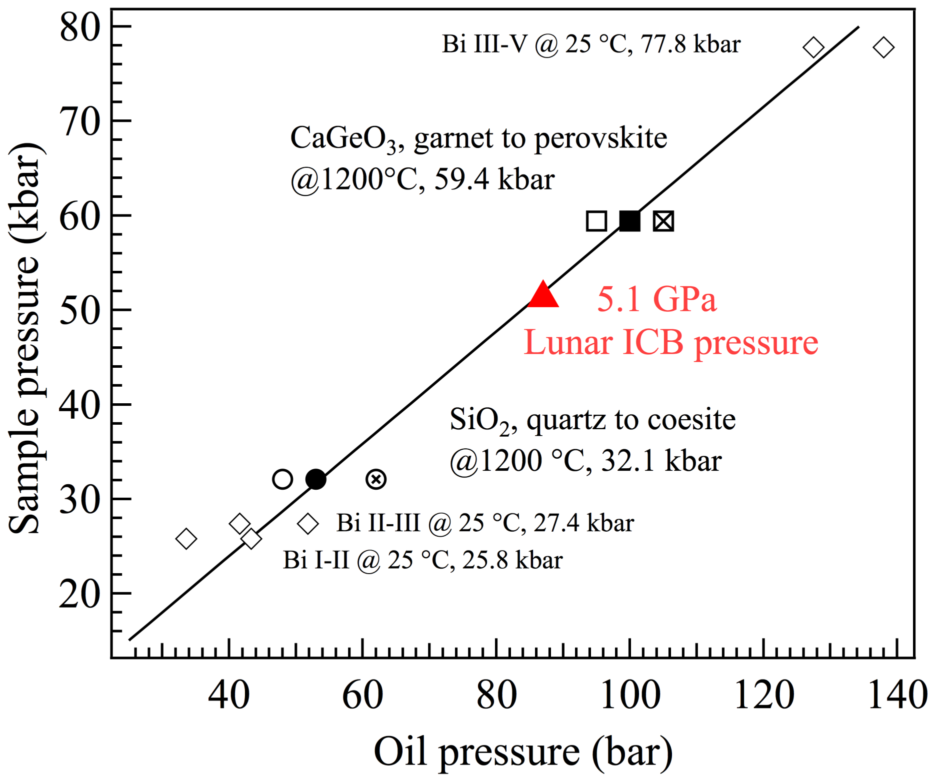

Figure 5.1. Multi-anvil calibration curve for Umich 17/12 assembily estimated by bismuth (Bi) I-II, II-III and III-V transition at ambient temperature (run 072315 and 081213); quartz to coesite transition at 32.1 kbar and 1200 °C (run 092211, 092511 and 021812); CaGeO3 garnet to perovskite transition at 59.4 kbar and 1200 °C (run 101511, 110311 and 012212). The solid circle and square are conditions where high-pressure and low-pressure phases coexist; the open symbols are conditions where only low-pressure phases are found while the open symbols with crosses inside are conditions where only high-pressure phases are found. To reach the pressure of the lunar inner-core boundary, the corresponding oil pressure is 87 bar (red triangle).

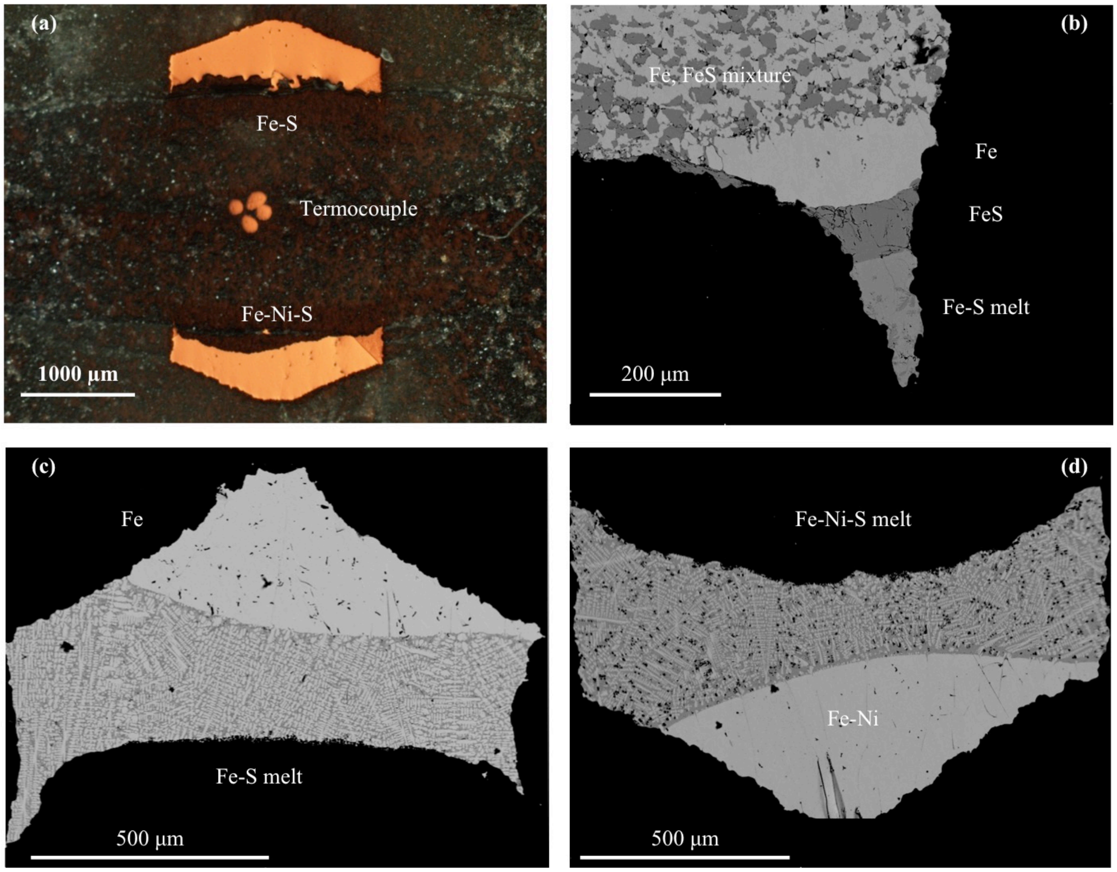

Figure 5.2. (a) Reflective light image of the experiment at 5.1 GPa, 1478 K (Run ID 043012). The two sample chambers are at equal distance from the thermocouple, which is placed at the geometric center of the heater; (b) Back-scattered-electron (BSE) image showing part of the Fe-S sample in the experiment at 5.1 GPa, 1286 K (Run ID 082212). Most of the sample consists of a mixture of solid Fe and solid FeS. At the lower corner of the sample, solid Fe (bright) and solid FeS (dark) coexist with a small patch of Fe-S eutectic melt (with dendritic texture); (c) and (d) are BSE images of Fe-S and Fe-Ni-S samples respectively, in the experiment at 5.1 GPa and 1580 K (Run ID 081912) These typical run products contain solid Fe (bright) and Fe-S or Fe-Ni-S melt with dendritic texture.

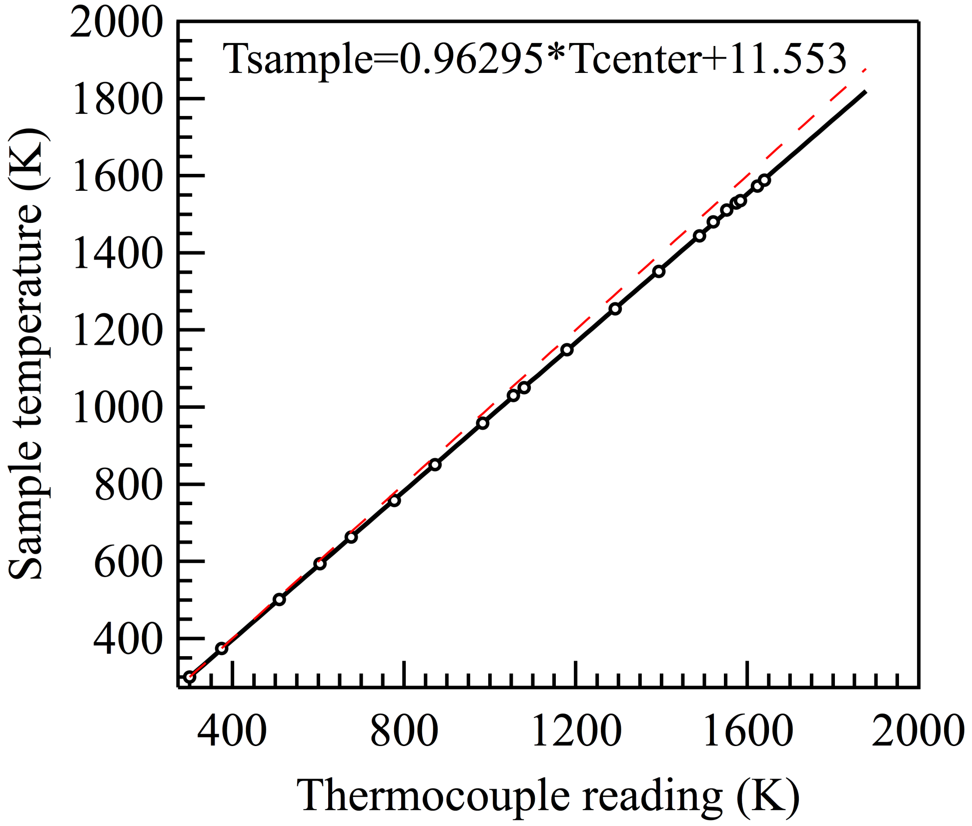

Figure 5.3. The relation between thermocouple reading and temperature in sample chambers. This relation was obtained by placing one set of thermocouple in the center of assembly and another set of thermocouple in sample chamber position in a test experiment. The red dashed line with a slope of 1 as comparison.

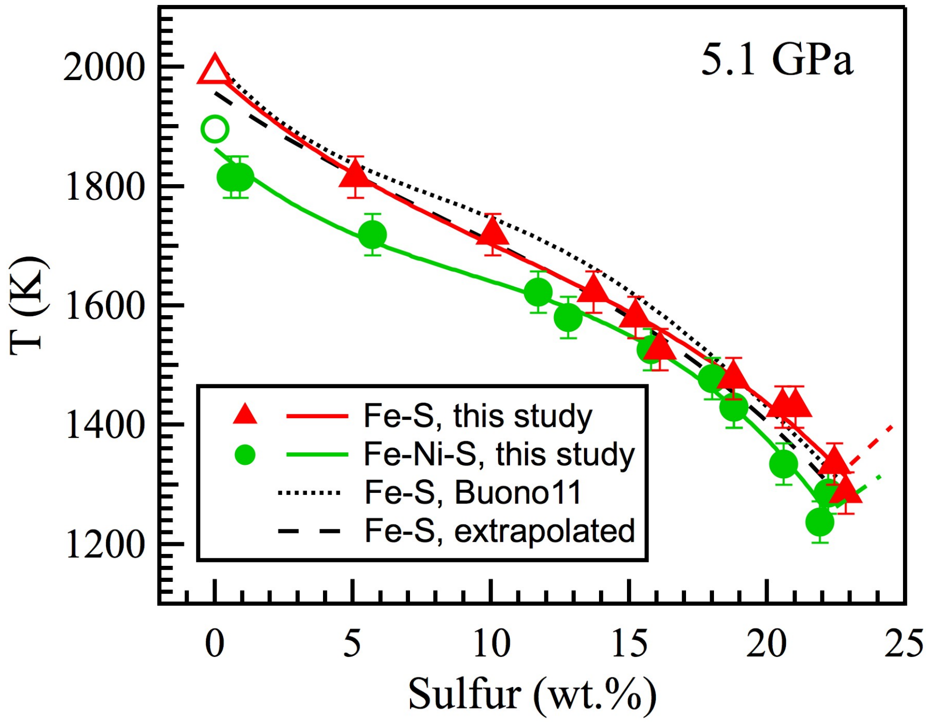

Figure 5.4. The liquidi of Fe-S and Fe-Ni-S systems at 5.1 GPa. The red and green solid curves are 3rd order polynomial fittings to the data from this study (red solid triangles for Fe-S and green solid circles for Fe-Ni-S), with an estimated uncertainty of ± 35 K in temperature (see text for details). The red open triangle and green open circle mark the melting temperature of pure iron and Fe-50wt.%Ni, respectively (Anderson and Isaak, 2000; Tomiska and Neckel, 1985). The dotted curve is the calculated Fe-S liquidus from Buono and Walker (2011). The dashed curve is constructed from linear interpolations (see text for details) of liquidi data at 1 bar (Hansen and Anderko, 1958), 3 GPa (Brett and Bell, 1969), and 10 GPa (Chen et al., 2008).

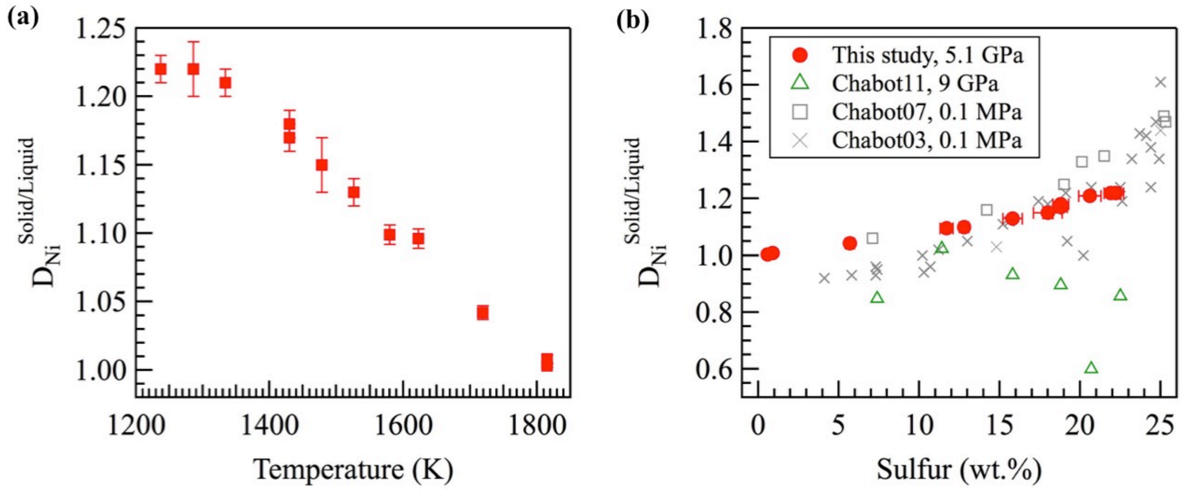

Figure 5.5. Solid metal/liquid metal partitioning of Ni in Fe-Ni-S system at 5.1 GPa. The partitioning data for Ni are from this study, Chabot et al. (2003, 2007, 2011).

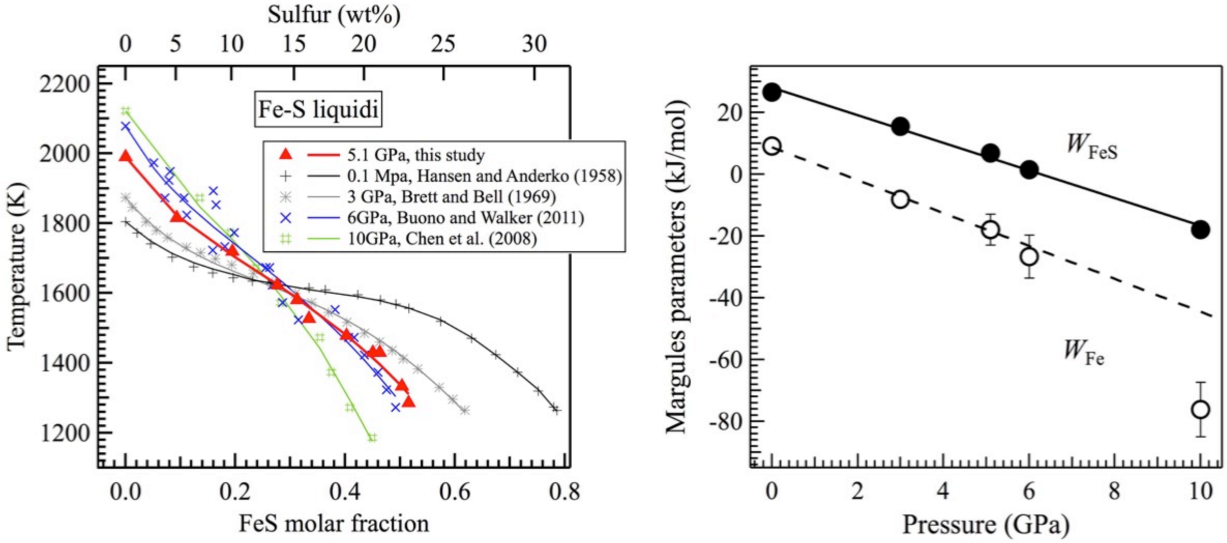

Figure 5.6. (a) Fe-S liquidi between 1 bar and 10 GPa. Solid curves are fittings to experimental data using the asymmetric Margules solution formulation. (b) Fitted Margules parameters W_{Fe} (open circles) and W_{FeS} (solid circles) as a function of pressure. The parameters at 5.1, 6, and 10 GPa form linear trends (dashed lines), which do not pass through the points at 1 bar. Error bars represent fitting errors.

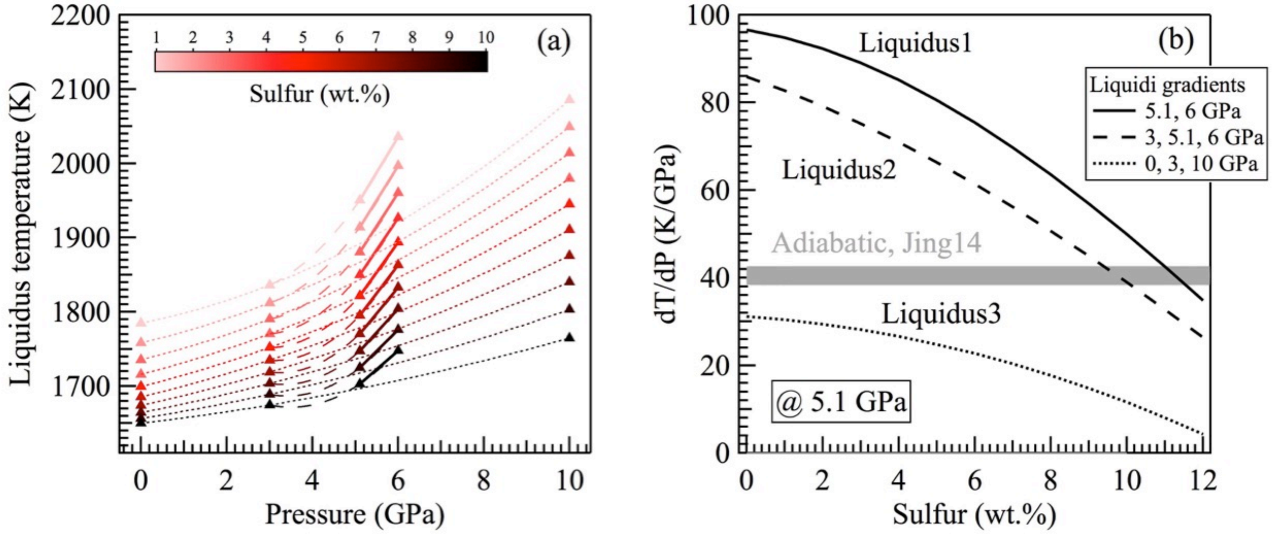

Figure 5.7. (a) Pressure dependence of liquidus temperature for Fe-S mixtures containing 1 wt.% to 10 wt.% sulfur, on the basis of the liquidus curves in Fig. 4(a). The solid lines connects the points at 5.1 GPa and 6 GPa; the dotted curves are quadratic fittings for points at 1 bar, 3 GPa and 10 GPa; the dashed curves are quadratic fittings for points at 3, 5.1 and 10 GPa. (b) The comparison between liquidus gradients and adiabatic gradients at lunar ICB pressure (5.1 GPa) for sulfur content up to 12 wt.%. The black curve is liquidus gradient derived from linear regression of Fe-S liquidi at 5.1 GPa and 6 GPa; the dotted curve is that from quadratic regression of Fe-S liquidi at 1 bar, 3 GPa and 10 GPa; the dashed curve is that from quadratic regression of Fe-S liquidi at 3 GPa, 5.1 GPa and 6 GPa. The gray area displays the range of calculated adiabatic gradients given in Jing et al. (2014).

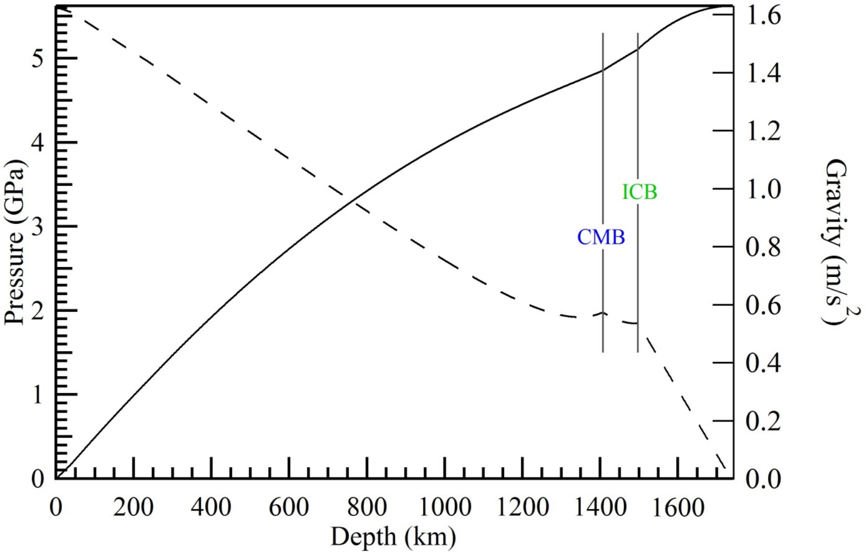

Figure 5.8. Pressure (solid) and and gravitational acceleration (dashed) in lunar interior, calculated from the density profile given in Weber et al. (2011).

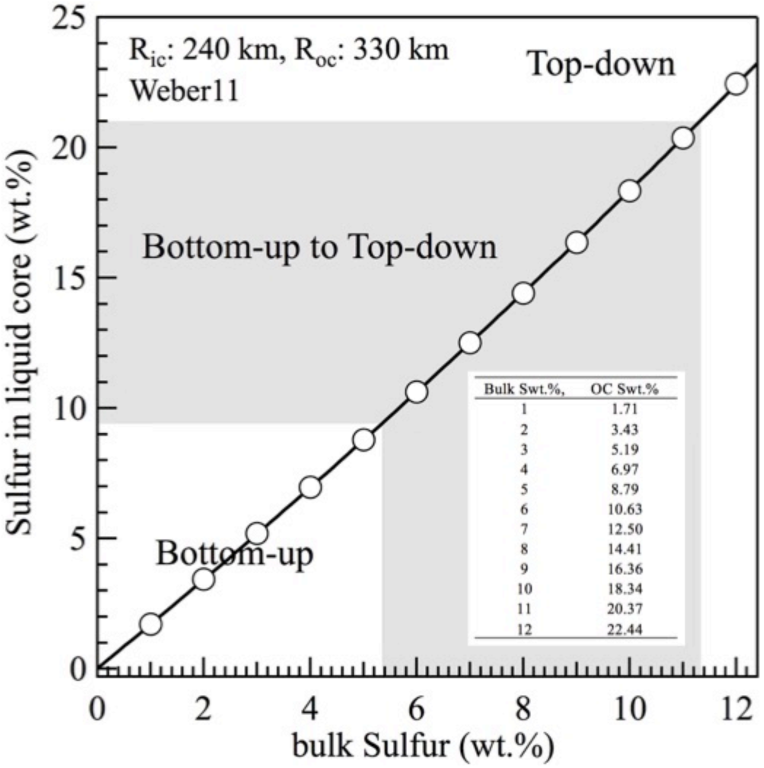

Bulk Swt.%,	OC Swt.%
1	1.71
2	3.43
3	5.19
4	6.97
5	8.79
6	10.63
7	12.50
8	14.41
9	16.36
10	18.34
11	20.37
12	22.44

Figure 5.9. The relation between the bulk sulfur content of the lunar core and sulfur content of the outer core. The blue symbols and curve are for a core with 330 km radius and an inner core with 240 km radius (Weber et al., 2011); the corresponding sulfur contents are listed in the inset table. If the adiabatic gradient and the liquidi gradient are equal when sulfur content is 9.5~11.3 wt.% in the Fe-S system, the gray region marks the sulfur contents for a transition of core crystallization scheme from the bottom-up to the top-down.

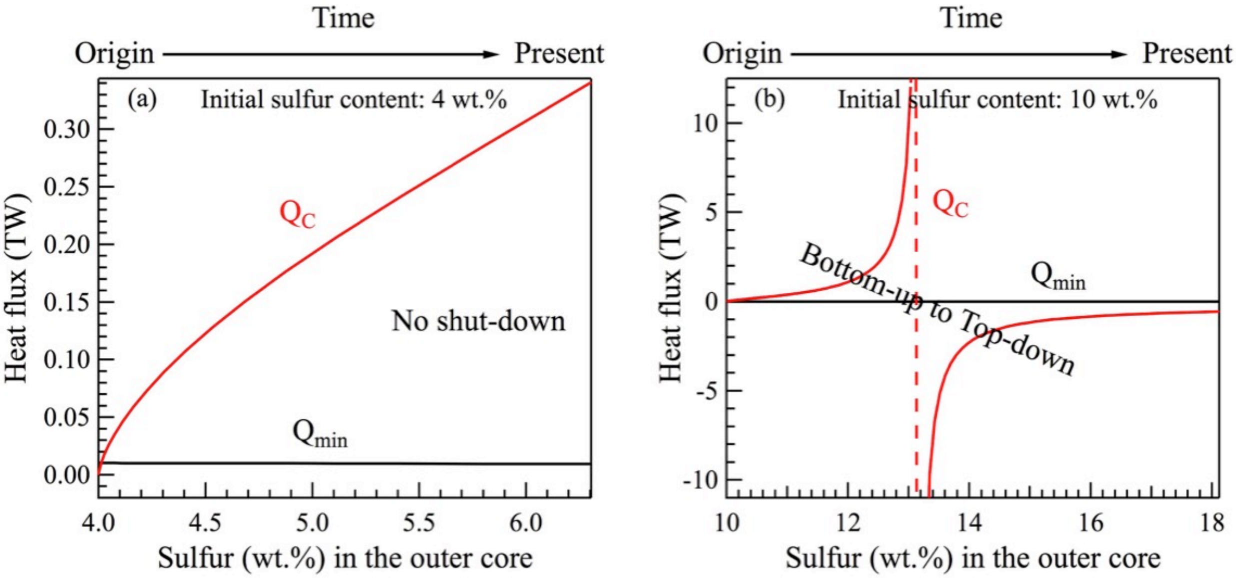

Figure 5.10. To prevent the core dynamo from shutting down, the compositional heat flux Q_c (red curve) must exceed the minimum heat flux Q_{min} across the lunar core-mantle boundary (CMB). (a) The initial sulfur content of the lunar core is assumed to be 4 wt.%. No shut-down is expected. (b) The initial sulfur content of the lunar core is assumed to be 10 wt.%. The dashed lines mark the transition of the scheme of core solidification from bottom-up to "snowing". During the transition, the core is expected to freeze simultaneously at all depths.

5.7 References

Anderson, O.L., Isaak, D.G., 2000. Calculated melting curves for phases of iron. Am Mineral 85, 376-385.

Badro, J., Fiquet, G., Guyot, F., Gregoryanz, E., Occelli, F., Antonangeli, D., d'Astuto, M., 2007. Effect of light elements on the sound velocities in solid iron: Implications for the composition of Earth's core. Earth Planet Sc Lett 254, 233-238.

Balog, P.S., Secco, R.A., Rubie, D.C., Frost, D.J., 2003. Equation of state of liquid Fe-10 wt % S: Implications for the metallic cores of planetary bodies. J Geophys Res-Sol Ea 108.

Bose, K., Ganguly, J., 1995. Quartz-Coesite Transition Revisited - Reversed Experimental-Determination at 500-1200-Degrees-C and Retrieved Thermochemical Properties. Am Mineral 80, 231-238.

Brett, R., Bell, P.M., 1969. Melting relations in the Fe-rich portion of the system Fe–FeS at 30 kb pressure. Earth Planet. Sci. Lett. 6, 479–482.

Buono, A.S., Walker, D., 2011. The Fe-rich liquidus in the Fe-FeS system from 1 bar to 10 GPa. Geochim Cosmochim Ac 75, 2072-2087.

Chabot, N.L., Campbell, A.J., Jones, J.H., Humayun, M., and Agee, C.B. (2003) An experimental test of Henry's Law in solid metal-liquid metal systems with implications for iron meteorites. Meteoritics & Planetary Science, 38(2), 181-196.

Chabot, N.L., McDonough, W.F., Jones, J.H., Saslow, S.A., Ash, R.D., Draper, D.S., Agee, C.B., 2011. Partitioning behavior at 9 GPa in the Fe-S system and implications for planetary evolution. Earth Planet Sc Lett 305, 425-434.

Chabot, N.L., Saslow, S.A., McDonough, W.F., McCoy, T.J., 2007. The effect of Ni on element partitioning during iron meteorite crystallization. Meteorit Planet Sci 42, 1735-1750.

Chen, B., Li, J., Hauck, S.A., 2008. Non-ideal liquidus curve in the Fe-S system and Mercury's snowing core. Geophys Res Lett 35.

Chen, J.H., Yu, T., Huang, S., Girard, J., Liu, X.Y., 2014. Compressibility of liquid FeS measured using X-ray radiograph imaging. Phys Earth Planet In 228, 294-299.

Dauphas, N., Burkhardt, C., Warren, P.H., Teng, F.Z., 2014. Geochemical arguments for an Earth-like Moon-forming impactor. Philos T R Soc A 372.

Davies, C.J., Gubbins, D., 2011. A buoyancy profile for the Earth's core. Geophys J Int 187, 549-563.

Decker, D.L., Bassett, W.A., Merrill, L., Hall, H.T., and Barnett, J.D., 1972. High-pressure calibration: A critical review. Journal of Physical and Chemical Reference Data, 1, 773– 835.

Drake, M.J., 1987. Siderophile Elements in Planetary Mantles and the Origin of the Moon. J Geophys Res-Solid 92, E377-E386.

Dwyer, C.A., Stevenson, D.J., Nimmo, F., 2011. A long-lived lunar dynamo driven by continuous mechanical stirring. Nature 479, 212-U284.

Fei, Y.W., Bertka, C.M., Finger, L.W., 1997. High-pressure iron sulfur compound, Fe_3S_2, and melting relations in the Fe-FeS system. Science 275, 1621-1623.

Fei, Y.W., Prewitt, C.T., Mao, H.K., Bertka, C.M., 1995. Structure and Density of FeS at High-Pressure and High-Temperature and the Internal Structure of Mars. Science 268, 1892-1894.

Garrick-Bethell, I., Weiss, B.P., Shuster, D.L., Buz, J., 2009. Early Lunar Magnetism. Science 323, 356-359.

Hansen, M., Anderko, K., 1958. Constitution of the Binary Alloys, 2nd ed. McGraw- Hill Book Co., New York.

Hauck, S.A., Aurnou, J.M., Dombard, A.J., 2006. Sulfur's impact on core evolution and magnetic field generation on Ganymede. J Geophys Res-Planet 111.

Hauri, E.H., Weinreich, T., Saal, A.E., Rutherford, M.C., Van Orman, J.A., 2011. High Pre-Eruptive Water Contents Preserved in Lunar Melt Inclusions. Science 333, 213-215.

Hixson, R.S., Winkler, M.A., Hodgdon, M.L., 1990. Sound speed and thermophysical properties of liquid iron and nickel. Phys. Rev. B 42, 6485–6491.

Jing, Z.C., Wang, Y.B., Kono, Y., Yu, T., Sakamaki, T., Park, C., Rivers, M.L., Sutton, S.R., Shen, G.Y., 2014. Sound velocity of Fe-S liquids at high pressure: Implications for the Moon's molten outer core. Earth Planet Sc Lett 396, 78-87.

Kantor, A.P., Kantor, I.Y., Kurnosov, A.V., Kuznetsov, A.Y., Dubrovinskaia, N.A., Krisch, M., Bossak, A.A., Dmitriev, V.P., Urusov, V.S., Dubrovinsky, L.S., 2007. Sound wave velocities of fcc Fe-Ni alloy at high pressure and temperature by mean of inelastic X-ray scattering. Phys Earth Planet In 164, 83-89.

Khan, A., Mosegaard, K., Williams, J.G., Lognonne, P., 2004. Does the Moon possess a molten core? Probing the deep lunar interior using results from LLR and Lunar Prospector. J Geophys Res-Planet 109.

Komabayashi, T., Fei, Y.W., 2010. Internally consistent thermodynamic database for iron to the Earth's core conditions. J Geophys Res-Sol Ea 115.

Laneuville, M., Wieczorek, M.A., Breuer, D., Aubert, J., Morard, G., Ruckriemen, T., 2014. A long-lived lunar dynamo powered by core crystallization. Earth Planet Sc Lett 401, 251-260.

Le Bars, M., Wieczorek, M.A., Karatekin, O., Cebron, D., Laneuville, M., 2011. An impact-driven dynamo for the early Moon. Nature 479, 215-U290.

Lesher, C.E., Walker, D., 1988. Cumulate Maturation and Melt Migration in a Temperature-Gradient. J Geophys Res-Solid 93, 10295-10311.

Li, J., Agee, C.B., 1996. Geochemistry of mantle-core differentiation at high pressure. Nature 381, 686-689.

Li, J., and Fei, Y., 2013. Experimental constraints on core composition. In: Holland, H. D. and Turekian, K. K. (Eds.), Treatise on Geochemistry 2nd edition, Vol. 2.14 Elsevier Ltd.

Li, J., Fei, Y., Mao, H.K., Hirose, K., Shieh, S.R., 2001. Sulfur in the Earth's inner core. Earth Planet Sc Lett 193, 509-514.

Mao, H.K., Wu, Y., Chen, L.C., Shu, J.F., Jephcoat, A.P., 1990. Static Compression of Iron to 300 Gpa and Fe0.8ni0.2 Alloy to 260 Gpa - Implications for Composition of the Core. J Geophys Res-Solid 95, 21737-21742.

Morard, G., Sanloup, C., Fiquet, G., Mezouar, M., Rey, N., Poloni, R., Beck, P., 2007. Structure of eutectic Fe-FeS melts to pressures up to 17 GPa: Implications for planetary cores. Earth Planet Sc Lett 263, 128-139.

Nishida, K., Kono, Y., Terasaki, H., Takahashi, S., Ishii, M., Shimoyama, Y., Higo, Y., Funakoshi, K., Irifune, T., Ohtani, E., 2013. Sound velocity measurements in liquid Fe-S at high pressure: Implications for Earth's and lunar cores. Earth Planet Sc Lett 362, 182-186.

Rai, N., van Westrenen, W., 2014. Lunar core formation: New constraints from metal-silicate partitioning of siderophile elements. Earth Planet Sc Lett 388, 343-352.

Righter, K., 2002. Does the Moon have a metallic core? Constraints from giant impact modeling and siderophile elements. Icarus 158, 1-13.

Rückriemen, T., Breuer, D., Laneuville, M., Spohn, T., 2014. Evolution of the Moon's Core in the Fe–snow Regime. In: 45th Lunar and Planetary Science Conference, p. 2546.

Saal, A.E., Hauri, E.H., Lo Cascio, M., Van Orman, J.A., Rutherford, M.C., Cooper, R.F., 2008. Volatile content of lunar volcanic glasses and the presence of water in the Moon's interior. Nature 454, 192-U138.

Sanloup, C., Guyot, F., Gillet, P., Fiquet, G., Hemley, R.J., Mezouar, M., Martinez, I., 2000. Structural changes in liquid Fe at high pressures and high temperatures from synchrotron X-ray diffraction. Europhys Lett 52, 151-157.

Sanloup, C., Guyot, F., Gillet, P., Fiquet, G., Mezouar, M., Martinez, I., 2000. Density measurements of liquid Fe-S alloys at high-pressure. Geophys Res Lett 27, 811-814.

Schwartzendruber L. J., Itkin V. P., and Alcock C. B. 1991 The Fe-Ni (iron-nickel) system. Journal of Phase Equilibria 12:288–312.

Secco, R.A., Schloessin, H.H., 1989. The Electrical-Resistivity of Solid and Liquid Fe at Pressures up to 7-Gpa. J Geophys Res-Solid 94, 5887-5894.

Shea, E.K., Weiss, B.P., Cassata, W.S., Shuster, D.L., Tikoo, S.M., Gattacceca, J., Grove, T.L., Fuller, M.D., 2012. A Long-Lived Lunar Core Dynamo. Science 335, 453-456.

Shimizu, H., Matsushima, M., Takahashi, F., Shibuya, H., Tsunakawa, H., 2013. Constraint on the lunar core size from electromagnetic sounding based on magnetic field observations by an orbiting satellite. Icarus 222, 32-43.

Stegman, D.R., Jellinek, A.M., Zatman, S.A., Baumgardner, J.R., Richards, M.A., 2003. An early lunar core dynamo driven by thermochemical mantle convection. Nature 421, 143-146.

Stevenson, D.J., Spohn, T., Schubert, G., 1983. Magnetism And Thermal Evolution Of the Terrestrial Planets. Icarus 54, 466-489.

Stewart, A.J., Schmidt, M.W., van Westrenen, W., Liebske, C., 2007. Mars: A new core-crystallization regime. Science 316, 1323-1325.

Suavet, C., Weiss, B.P., Cassata, W.S., Shuster, D.L., Gattacceca, J., Chan, L., Garrick-Bethell, I., Head, J.W., Grove, T.L., Fuller, M.D., 2013. Persistence and origin of the lunar core dynamo. P Natl Acad Sci USA 110, 8453-8458.

Susaki, J., Akaogi, M., Akimoto, S., Shimomura, O., 1985. Garnet-Perovskite Transformation in Cageo3 - Insitu X-Ray Measurements Using Synchrotron Radiation. Geophys Res Lett 12, 729-732.

Terasaki, H., Kato, T., Urakawa, S., Funakoshi, K., Sato, K., Suzuki, A., Okada, T., 2002. Viscosity change and structural transition of Molten Fe at 5 GPa. Geophys Res Lett 29.

Tikoo, S.M., Weiss, B.P., Buz, J., Lima, E.A., Shea, E.K., Melo, G., Grove, T.L., 2012. Magnetic fidelity of lunar samples and implications for an ancient core dynamo. Earth Planet Sc Lett 337, 93-103.

Weber, R.C., Lin, P.Y., Garnero, E.J., Williams, Q., Lognonne, P., 2011. Seismic Detection of the Lunar Core. Science 331, 309-312.

Wieczorek, M.A., Jolliff, B.L., Khan, A., Pritchard, M.E., Weiss, B.P., Williams, J.G., Hood, L.L., Righter, K., Neal, C.R., Shearer, C.K., McCallum, I.S., Tompkins, S., Hawke, B.R., Peterson, C., Gillis, J.J., Bussey, B., 2006. The constitution and struc- ture of the lunar interior. In: Jolliff, B.L., Wieczorek, M.A., Shearer, C.K., Neal, C.R. (Eds.), New Views of the Moon. Mineralogical Society of America, pp. 221–364.

Williams, J.G., Boggs, D.H., Yoder, C.F., Ratcliff, J.T., Dickey, J.O., 2001. Lunar rotational dissipation in solid body and molten core. J Geophys Res-Planet 106, 27933-27968.

Williams, Q., 2009. Bottom-up versus top-down solidification of the cores of small solar system bodies: Constraints on paradoxical cores. Earth Planet Sc Lett 284, 564-569.

Zhang, L., Fei, Y.W., 2008. Effect of Ni on Fe-FeS phase relations at high pressure and high temperature. Earth Planet Sc Lett 268, 212-218.

Zhang, N., Parmentier, E.M., Liang, Y., 2013. A 3-D numerical study of the thermal evolution of the Moon after cumulate mantle overturn: The importance of rheology and core solidification. J Geophys Res-Planet 118, 1789-1804.

Zhang, Y.G., Guo, G.J., 2000. Molecular dynamics calculation of the bulk viscosity of liquid iron-nickel alloy and the mechanisms for the bulk attenuation of seismic waves in the Earth's outer core. Phys Earth Planet In 122, 289-298.

Chapter VI. Conclusions

This dissertation focuses on the nature and dynamics of the Earth's lower mantle, the Earth's and lunar cores. Using high pressure devices, micro-analytical instruments and synchrotron radiation facilities, I studied the crystal chemistry of bridgmanite (Chapter II), the melting curves of Fe-S and Fe-Ni-S at the lunar core pressure (Chapter III); the magneto-elastic interaction in Fe_7C_3 (Chapter IV) and the eutectic melting of Fe-C system up to 120 GPa (Chapter V). Below I summarize the main conclusions in each chapter and their broad geochemical and geophysical implications.

In chapter II, I reported the Debye temperatures of Fe^{2+} and Fe^{3+} in Al-bearing bridgmanite, the dominant phase in the Earth's lower mantle. These data are necessary for calculating the Fe^{3+} content of bridgmanite samples from its area fraction obtained by Mössbauer spectroscopy, and to my knowledge they do not exist in the literature. Furthermore, I inferred the site occupancy of Fe^{3+} in a large number of bridgmanite samples reported in the literature and offered new insights into the crystal chemistry and electric conduction mechanisms in bridgmanite. In addition, an Fe^{2+} component with a large quadrupole splitting (QS) near 4.0mm/s was observed at 1 bar and below 250 K. The occurrence of this component suggests that large QS value may result from distortion and should not be used as a diagnostic signature of intermediate spin state as proposed recently.

In Chapter III, two discontinuities were found in the compression curve of Fe_7C_3 up to 70 Gpa and 300 K: the first one is attributed to a ferromagnetic to paramagnetic transition at 5.6 ~

8.9 GPa; the second one is assigned to a paramagnetic to nonmagnetic transition between 21.2 ~ 23.5 GPa. The elastic parameters of these three magnetic phases were derived by fitting the compression curves by Birch-Murnaghan equations of state. Across the first magnetic transition, the bulk modulus and its pressure dependence decrease, making Fe_7C_3 as an Invar alloy. My results support magnetoelastic interaction is the origin of the Invar behaviors. On the contrary, the second magnetic transition stiffens Fe_7C_3, making the density of the nonmagnetic phase matches that of the inner core. Either paramagnetic or nonmagnetic Fe_7C_3 could be the stable phase under the pressure-temperature conditions of the inner core, depending on the clapeyron slope of its spin transition. Further high pressure, high temperature works are needed to constrain this slope and test the model of an Fe7C3-dominant inner core.

In Chapter IV, based on the eutectic melting curve of Fe-C system, I proposed a new mechanism to explain the nonubiquitous occurrence of ultra-low velocity zones (ULVZs) near the core-mantle boundary: about 1 wt.% mixture of iron and diamond/iron carbide could be generated in subducted oceanic lithosphere when penetrating the 660 km discontinuity. The eutectic melting curve of Fe-C system intersects with mantle geothermal at 3068 kelvin and 128 GPa, implying that in the regions of subducted slabs, there would always be a small amount of melt (~ 1 wt.%) in the basal part of the lower mantle. Such metallic melt could completely wet grain boundaries and significantly lower seismic velocities. This scenario would lead to nonubiquitous low velocity zones with Vp drops more than Vs, which is a reasonable mechanism for ULVZs.

In Chapter V, I investigated the melting behaviors of both iron-sulfur system and iron-nickel-sulfur system at the pressure of the lunar inner-core boundary (5.1 GPa). Combined my data and other Fe-S melting data in literature, the liquidus slope with respect to pressure (dTm/dP) were calculated for different Fe-S compositions. The liquidus slope intersects with the adiabatic slope at 9.5 ~ 11.3 wt.% sulfur. In order to explain the long duration (> 500 million years) of lunar paleomagnetic field, the bulk sulfur content in the lunar core should range from 2.1 ~ 6.6 wt.%. In this case, the lunar core started to crystallize in the center and supported a long-lived lunar dynamo. However, due to the growth of the inner core, the lunar core would transits to crystallize from the top, resulting in that the lunar dynamo shut off shortly. My melting curves of possible lunar core materials at the pressure of the lunar inner-core boundary (5.1 GPa) can be directly employed to calculate the lunar temperature profile; model the lunar core and mantle convections; the lunar chemical evolution due to core formation and inner core crystallization.

In order to further investigate the hypothesis of a carbon-rich inner core, future work will focus on thermal equations of state (TEoS) for major iron carbides Fe_7C_3 and Fe_3C: such data can be directly compared with the density profile of the Earth's inner core and exam whether the presence of iron carbides in the inner core can explain its density deficit relative to solid iron at relevant temperature and pressure conditions. Moreover, such TEoS can constrain the Clapeyron slopes of paramagnetic to nonmagnetic transition in Fe_7C_3 and Fe_3C, which determine the stable magnetic phases at the inner core's temperature and pressure conditions.